EPFL

Bacterial colonization in realistic environments: how mechanics impact biofilm formation in the wild and during infection

Tamara ROSSY

■ École
polytechnique
fédérale
de Lausanne

2023

Acknowledgements

As I look back on these years of PhD, I realize how much I've learnt and grown since I joined the lab. This would not have been possible without all the amazing people who supported me at different stages of my project and personal life.

First, I would like to thank Alex Persat for having been a wonderful mentor. He gave me the greatest gift one can wish for from a supervisor: trust. He allowed me to work on a project that was far from my comfort zone, he encouraged me not to give up when obstacles came in the way, and always believed in me – even when I didn't. Alex, you made me a scientist and I will always be grateful for everything you taught me.

In addition, I thank Katharina Ribbeck, Sara Mitri, John McKinney and Selman Sakar for agreeing to be part of my thesis committee. I enjoyed interacting with them and benefiting from their expertise. Similarly, a few years ago, I received valuable input from Andy Oates, Tom Battin and Matthias Lutolf during my candidacy exam, for which I'm grateful.

I would also like to acknowledge all the people I had the chance to collaborate with: Carey Nadell, Joern Pezoldt, Bart Deplancke, Jaemin Kim, Nikolaos Bouklas, and Alexandra Iouranova, along with the EPFL core facilities who made our lives easier with their advice and experience.

On that note, I would like to extend a special thank you to Tania Distler, who has lifted a great weight off my shoulders since she joined the lab a bit more than a year ago. In addition to being a fast learner, Tania turned out to be a dedicated and supportive coworker, always offering to help with experiments, writing, proofreading… Tania, you have my full trust – I know AirGels are in great hands with you, and I'm convinced that you will keep producing high quality work, in the Persat lab and in your next workplaces.

Speaking of work environment, I feel extremely privileged to have been part of the EPFL SV community, both scientifically and socially. All the seminars, symposia, happy hours, Christmas parties and GHI retreats that took place during my PhD contributed to making it an unforgettable experience. I realized how much I missed those interactions during the COVID-19 pandemic and I'm glad the campus finally regained its vibrant atmosphere in the past few months. A big thank you to everyone who made these events possible! Owing to them, I have met great people from neighboring labs, with whom it's always fun to have a drink, go bouldering, or play table soccer.

During my PhD, I was also fortunate enough to meet scientists outside of EPFL, either during conferences or as part of our lab's involvement with the NCCR AntiResist consortium. I thank everyone I met on those occasions, in particular Benoît Laventie, with whom I regularly kept exchanging tips and tricks about HBE cells and *P. aeruginosa*.

A new interest I discovered during my PhD is science communication. I'm grateful to the people who gave me the chance to share my research in different ways, especially Eva Schier from the SV communications team, who has always shown great enthusiasm and support when we discussed my participation to outreach events. And of course, I would also like to mention the sci-comm highlight of my PhD: "Ma thèse en 180s". This contest gave me the opportunity to meet fantastic people, in particular the participants to the Swiss finals, with whom it's always nice to go out for a beer and chat! I would never have expected to enter a competition in such a friendly atmosphere, thank you so much! And kudos to the organizers, both at EPFL and at the CUSO.

Obviously, I cannot write the acknowledgements section of my thesis without mentioning the great companions who shared this journey with me: the members of the Persat group (who are probably laughing behind my back as I get emotional while typing those lines…). We started as a small family, when I joined Zainebe, Lorenzo, Xavier in the newly opened lab. Their warm welcome immediately made me feel at home. It was super exciting to set up the lab together, to run our first experiments, to figure things out along the way… We were then joined by many nice people who all brought something special to our team: Alice, Jeremy, Sophia, Marco, Alessandra, Sourabh, Pascal, Sofya,

understand each other. Thank you for always supporting me with your advice and offering me a place to stay when I needed it. I also thank Chloé, Prisca and Léa for all the nice and extremely ~~noisy~~ lively moments we spent together; Elodie for the endless audio messages and phone calls; Sara and Stéphane for always being up to party and chat until dawn; Olivier and Quentin for encouraging and accompanying me during important moments of my life; Loïc and Laureline for reminding me all the fun times we spent together in high school; Marie-Pierre and Emile for supporting me in my creative writing projects; and Camille for being a great singing teacher.

A very special thanks goes to Martin, for being one of the most inspiring people I've ever met. You are a unique blend of kindness, independence and reliability. Thank you for bringing me closer to the person I want to be. I can't wait to see what the future holds for us!

I also want to thank my family (and our big puppy Masha!), on the Rossy, Chamero, Richard and Trujillo sides, for all the good times we've spent together. A special thought goes to my grandpas, who sadly passed away many years ago, but greatly contributed to my upbringing – they are missed dearly. To conclude, I cannot even express how grateful I am to my parents, Gloria and Jean-Marc, and to my sister (and best friend!) Alexandra. The three of you have always been there for me, with your unconditional support, your great advice, your hugs, your warmth, your love, … I owe you everything. Thank you, a thousand times, and even more!

Abstract

A variety of mechanical inputs acts onto bacteria in nature. However, these are most often ignored in the studies of their physiology, despite increasing evidence for bacterial mechanosensing. Quantitative links between environmental mechanics, bacterial colonization and physiology remain to be established. For that purpose, we must study bacteria in environments integrating relevant mechanical features. The constant improvement of microfabrication technologies and tissue engineering provides valuable tools to mimic such environments in the laboratory. During my PhD, I investigated biofilm formation in engineered microenvironments reproducing realistic conditions. First, I used a microfluidics approach to understand how flow intensity modulates biofilm architecture of the freshwater bacterium *Caulobacter crescentus.* I observed that surface colonization rate and lineage mixing decreased with increasing flow velocity. By modulating strain segregation, flow might thus influence the social interactions between biofilm-dwelling bacteria. These findings indicate that social interactions are not only dictated by biological factors, but also by mechanical conditions imposed onto the community. Second, I developed a tissue-engineered human airway model allowing to monitor respiratory infections at high spatiotemporal resolution. I demonstrated that it recapitulates key features of the human airway epithelium, such as mucus secretion and beating cilia. I then studied biofilm formation by the opportunistic pathogen *Pseudomonas aeruginosa* in this model airway. Surprisingly, *P. aeruginosa* was found to form mucus-associated biofilms within hours, much faster than previously observed in *in vitro* experiments. Bacterial aggregation was accelerated through active contraction of mucus by the pathogen's retractile type IV pili. These results suggest that, while protecting epithelia, mucus constitutes a breeding ground for biofilms. Overall, my PhD thesis provides the community with new tools to study microbes in a more realistic physical context. In addition, it sheds light on the complex interplay between mechanics and bacterial colonization, determining the fate of bacteria in natural environments.

Keywords

Résumé

Dans la nature, les bactéries sont exposées à toutes sortes de signaux mécaniques. Cependant, ceux-ci sont souvent ignorés dans les études microbiologiques, malgré les preuves de plus en plus nombreuses de mécanosensation bactérienne. Des liens quantitatifs entre mécanique environnementale, colonisation bactérienne et physiologie restent à établir. Pour cela, il est nécessaire d'étudier les bactéries dans des environnements intégrant des signaux mécaniques pertinents. L'amélioration constante des technologies de microfabrication et d'ingénierie tissulaire fournit des outils précieux pour imiter de tels environnements *in vitro*. Au cours de mon doctorat, j'ai étudié la formation de biofilms dans des microenvironnements artificiels reproduisant des conditions réalistes. Tout d'abord, j'ai utilisé une approche microfluidique pour comprendre comment l'intensité du flux module l'architecture des biofilms formés par la bactérie d'eau douce *Caulobacter crescentus*. J'ai observé que le taux de colonisation de surface et le mélange des lignées diminuaient avec l'augmentation de la vitesse d'écoulement. En modulant la ségrégation des souches, le flux pourrait ainsi influencer les interactions sociales entre les bactéries peuplant le biofilm. Ceci indique que les interactions sociales ne sont pas seulement dictées par des facteurs biologiques, mais également par les conditions mécaniques imposées à la communauté. Deuxièmement, j'ai développé un modèle de voies respiratoires humaines en utilisant des techniques d'ingénierie tissulaire. Ce nouveau modèle permet une étude des infections respiratoires à haute résolution spatiotemporelle. J'ai démontré qu'il récapitulait les principales caractéristiques de l'épithélium des voies respiratoires humaines, telles que la sécrétion de mucus et le battement des cils. J'ai ensuite étudié la formation de biofilms par le pathogène opportuniste *Pseudomonas aeruginosa* dans ce modèle de voie respiratoire. Étonnamment, *P. aeruginosa* s'est avérée former des biofilms sur le mucus en quelques heures seulement, beaucoup plus rapidement que ce qui avait été observé dans des expériences *in vitro* par le passé. L'agrégation bactérienne semble accélérée par une contraction active du mucus ; cette dernière est générée par les pili rétractiles de type IV que possède *P. aeruginosa*. Ces résultats suggèrent que, tout en protégeant l'épithélium, le mucus constitue un terreau fertile pour les biofilms. Dans l'ensemble, ma thèse de doctorat fournit de nouveaux outils pour étudier les microbes dans un contexte physique réaliste. De plus, elle met en lumière l'interaction complexe entre la mécanique et la colonisation bactérienne, déterminant le sort des bactéries dans les environnements naturels.

Mots-clés

Biofilms ; Microfluidique ; Hydrodynamique ; Ingénierie tissulaire ; Modèles pulmonaires ; Infections respiratoires ; Mucus.

Contents

List of Figures

List of Supplementary Figures

List of Tables

List of Abbreviations

T4P	type IV pili
EPS	exopolysaccharides
MCC	mucociliary clearance
CF	cystic fibrosis
COPD	chronic obstructive pulmonary disease
Pe	Péclet number
ALI	air-liquid interface
iPSCs	induced pluripotent stem cells
HBE cells	human bronchial epithelial cells
PDMS	polydimethylsiloxane
PEG	polyethylene glycol
ECM	extracellular matrix
SPIM	selective plane illumination microscope
scRNA-seq	single-cell RNA sequencing
CBF	cilia beating frequency
ASL	airway surface liquid

A mi abuelito, que hubiera sido muy orgulloso

Chapter 1. Introduction

I will start with a general introduction bridging the different subjects of this thesis. I also provide more specific background information at the beginning of each chapter.

Bacteria have colonized almost every possible niche on Earth. Consequently, they are exposed to a wide range of forces from their environment (Figure 1.1), such as shear stress from fluid flow or compressive forces from interactions with surfaces[1,2]. Even though bacteria are constantly subjected to mechanical inputs, we still do not fully understand how they sense and respond to these signals.
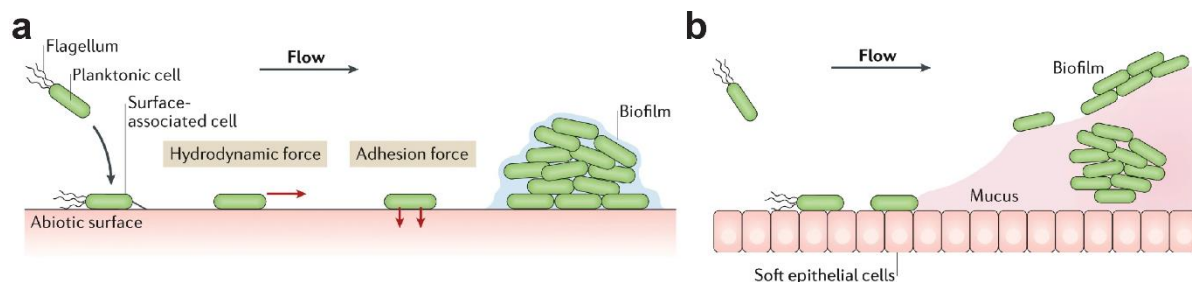
Figure 1.1: Forces acting on bacteria.

(a) During colonization of abiotic surfaces in flow conditions, bacteria may experience hydrodynamic and adhesion forces. (b) The mechanical properties of host tissues often differ from abiotic surfaces, since bacteria might come in contact with soft epithelial cells or mucus. Adapted from [2].

Nevertheless, we know that bacteria physically interact with their surroundings through surface appendages, such as type IV pili (T4P). These retractile filaments are involved in a mode of surface motility called twitching[3] and also serve to probe the mechanical properties of the substrate[4,5]. Mechanical cues can trigger physiological responses in bacteria. For example, T4P-mediated surface sensing increases the pathogenicity of *Pseudomonas aeruginosa* by promoting the transcription of virulence genes, such as quorum sensing or secretion systems[5,6]. Over longer timescales, bacteria such as *P. aeruginosa, Caulobacter crescentus* and *Bacillus subtilis* produce sticky substances

called exopolysaccharides (EPS) in response to surface sensing[2]. EPS play an important role for the formation of multicellular communities termed biofilms[7,8]. Environmental cues also influence the architecture and mechanical properties of these communities[9], as will be discussed in the next section.

1.1 Biofilm mechanics

In the wild, microbes predominantly live in biofilms[10]. In this section, I will give examples illustrating how mechanics impact biofilms at liquid-solid interfaces. Indeed, the typical view of biofilms depicts those communities as surface-associated, although recent literature makes a case for revising this definition in order to encompass broader aggregation phenomena[11].
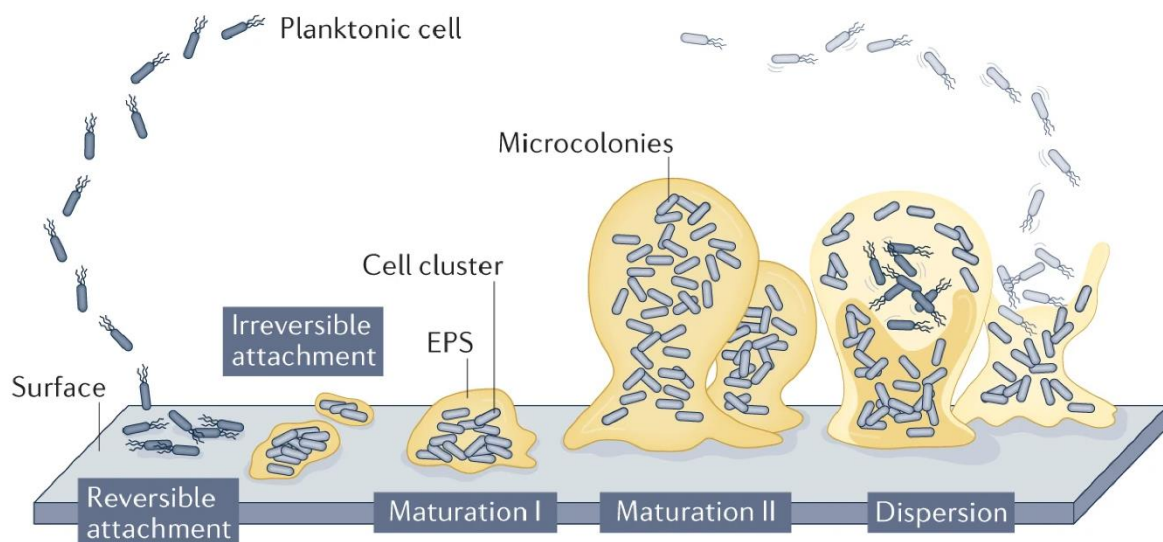
Figure 1.2: Five-step biofilm life cycle model.

Classical view of the biofilm life cycle, involving attachment of planktonic cells to a surface, maturation and dispersion of single cells back into the planktonic phase. From [11].

The classical biofilm life cycle model (Figure 1.2) starts with the attachment of individual planktonic cells to a solid substrate, first reversibly and then irreversibly[12]. This step is followed by the secretion of EPS matrix surrounding biofilm-dwelling cells[12]. These small, matrix-embedded clusters then mature into larger microcolonies, before dispersing back to planktonic cells. By attaching to the surface, single cells can nucleate new biofilms, thereby restarting the cycle[12].

1.1.1 Biofilm morphogenesis

Several factors influence the initial stage of surface attachment; for example, appendages, like T4P and flagella, can interact with the surface either in a specific (e.g. receptor-ligand binding) or unspecific way (e.g. friction)[13]. Beyond those direct interactions, the flagellum can play an important role in increasing the rate of encounter of swimming bacteria with surfaces[13].

The material properties of the substrate are also critical to determine whether bacteria will be able to attach and develop into biofilms. For instance, micropatterned surfaces covered in a fully wetted film hinder biofilm formation[14]. The properties of the substrate may influence colony morphology, motility of single cells and mixing of different strains[15], along with the stiffness of the biofilm itself[16].

Finally, cell shape also determines whether a bacterium will be able to attach to a substrate under specific conditions. *C. crescentus*, with its characteristic crescent shape, is well-adapted for surface colonization under moderate flows. Flow orients the curved cell body so that the pole of dividing cells is in close proximity to the surface, facilitating adhesion compared to straight mutants[17] (Figure 1.3a). Also, bacteria with a high aspect ratio are more easily trapped than round cells in porous environments (like soil) and as a result are advantaged to colonize such habitats[13].

1.1.2 Impact of transport phenomena on biofilm architecture

The density and architecture of the EPS matrix dramatically influences the local environment to which biofilm-dwelling cells are exposed: deep in the biofilm, the concentration of oxygen and nutrients is lower than at the surface, which may result in species stratification[9]. The different growth rates of bacteria residing at different locations influence the topology of the biofilm[9], in which voids and channels may arise, locally enhancing nutrient transport[13] (Figure 1.3b).

The quantity of small molecules that reach cells within a biofilm does not only depend on the EPS architecture, but also on hydrodynamic conditions[13]. In addition to nutrients, flow carries signaling molecules away from the growing colony. This may lead to gradients of quorum sensing signals between the core and the surface of the biofilms, as observed for *Staphylococcus aureus*, or between different portions of pipes in industrial settings[13].

Flow can also transport single cells, leading to their accumulation in regions of given shear stress. For example, as the affinity of the FimH adhesin to mannose increases with shear, *Escherichia coli* frequently accumulates in regions subjected to strong flows[18]. Fluid shear also causes the erosion of biofilms; as a consequence, bacteria have evolved strategies to consolidate the biofilm in response to flow, such as increased EPS secretion[13,16] (Figure 1.3c). Owing to its viscoelastic properties, the EPS matrix thus helps the biofilm withstand shear forces[16].
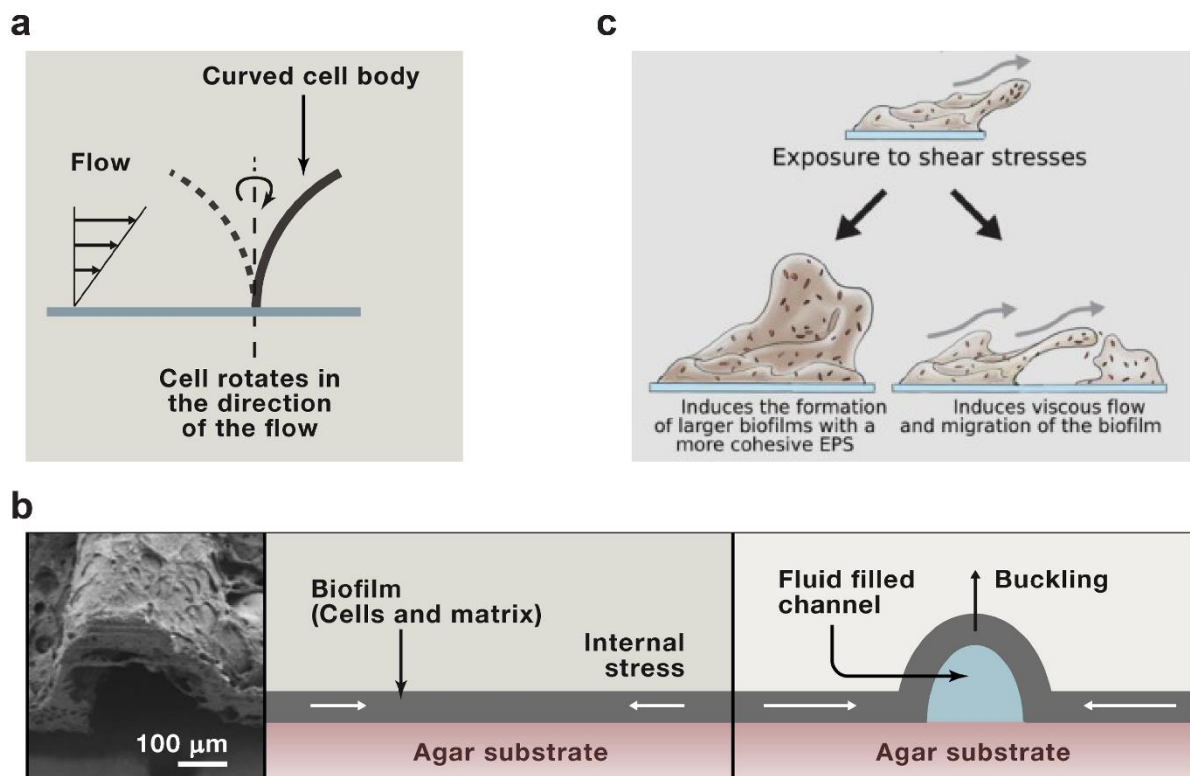
Figure 1.3: Bacterial colonies and flow.

(a) Cell shape sometimes provide a colonization advantage under specific conditions, as for *C. crescentus*, whose curved body enhances attachment in flow environments. From [1]. (b) To release stresses in the growing colony, biofilms frequently buckle, leading to the appearance of voids and channels through which advective transport can happen. From [1]. (c) Biofilms can respond to shear stress in several manners, e.g. through increased secretion of EPS, which strengthens the whole colony, or by viscous flow, which constitutes a passive mode of migration. From [16].

1.1.3 Mechanics of the biofilm matrix

Owing to its viscoelastic nature, the EPS matrix deforms in response to mechanical perturbations[16]. Simulations showed that, in strong flow, the surface of biofilms is exposed to tensile forces and the upstream regions to compressive forces. Overall, this results in porosity gradients inside the biofilm:

the base is strengthened owing to a reduced porosity, while the upper parts remain soft and deform more[19]. Similarly, because of their viscoelasticity, shear-exposed biofilms sometimes passively flow on surfaces (Figure 1.3c). This has been proposed as a mechanism for migration of *P. aeruginosa* colonies along endotracheal tubes, ultimately resulting in ventilator-associated pneumonia[16]. The EPS matrix, and the stresses that build up as cells grow within, are also responsible for a self-healing property of biofilms: upon mechanical damage, *B. subtilis* biofilms rapidly expand, thereby repairing the compromised region[20]. In addition, internal stresses in the EPS matrix may play a role during infections. For example, *in vitro*, *Vibrio cholerae* biofilms growing on epithelial cell monolayers buckle to release those stresses, which deforms and disrupts the underlying tissue[21].

Finally, because of their ability to deform, biofilms exhibit different architectures in different flow regimes. Depending on the magnitude of shear stress, aquatic biofilms either form isotropic clusters, like stromatolites (low shear), or filamentous structures called streamers (high shear)[22]. Streamers arise in curved geometries under both turbulent and laminar conditions, and they often lead to the clogging of pipes[13] (Figure 1.4a). This highlights the dynamic interplay between biofilm architecture and environmental mechanics: as the spatial organization of a biofilm changes, it feeds back onto the flow profile, which modifies the local conditions and creates new niches[13]. This process was illustrated in a study where WT and matrix-deficient *P. aeruginosa* co-existed in porous microenvironments[23]. As WT biofilms grew and clogged the pores, they generated low-shear zones that could be colonized without relying on EPS. Therefore, matrix-deficient mutants thrived in those regions (Figure 1.4b).

1.1.4 Social interactions in biofilms

The architecture and matrix properties of biofilms modulate the social interactions that occur between different strains or species. For example, a dense matrix is more difficult for new cells to invade[2]. In addition, in well-mixed biofilms, bacteria often develop competitive behaviors in order to surpass individuals with different genetic backgrounds. On the other hand, segregated environments tend to promote cooperative behaviors[24].
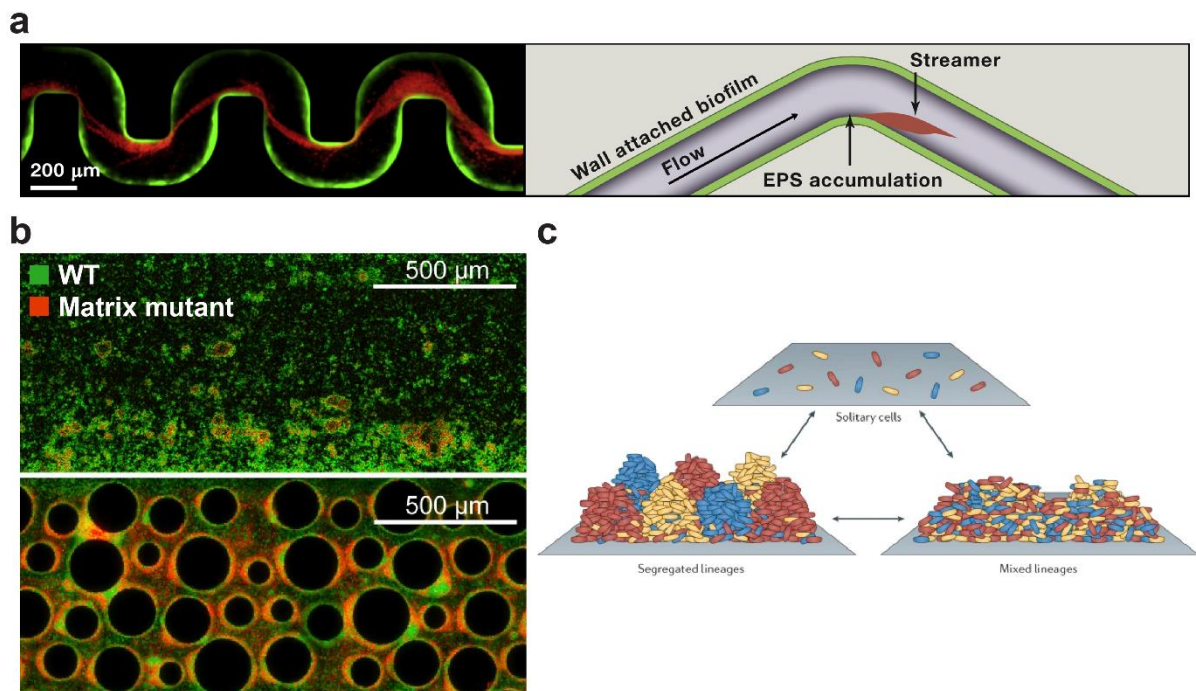
Figure 1.4: Spatial structure of biofilms – impact of environment and social interactions.

(a) Filamentous structures called streamers can form in curved channels under flow conditions. From [1]. (b) Colonization by specific mutant strains, such as a matrix-deficient *P. aeruginosa* (red), depends on the environmental conditions. Here, the mutant benefits from flow obstruction in a microchannel harboring a complex pattern. From [23]. (c) Different social phenotypes may arise depending on the spatial organization of strains and species within biofilms. These social phenotypes can alter the growth or viability of a subpopulation, which in turn generates new spatial patterns. From [24].

By remodeling the distribution of single cells within communities, social phenotypes then feed back on the spatial architecture of biofilms (Figure 1.4c). For example, cheating mutants that do no secrete matrix can arise in *Pseudomonas fluorescens* pellicle biofilms growing at the air-liquid interface. Since cheaters do not pay the cost of EPS secretion, their growth is facilitated. However, this has detrimental consequences for the community, since biofilms containing a large proportion of cheaters are mechanically weaker. Thus, the whole population eventually collapses into the liquid phase[9].

Overall, the fate of biofilm-dwelling cells depends on a complex combination of biological and mechanical cues. In the next section, I will motivate why it is crucial to study biofilms in realistic contexts with relevant environmental signals.

1.2 The threats of bacterial biofilms

As mentioned above, the biofilm lifestyle provides colonization advantages in various contexts. Surface association helps microorganisms access nutrients or remain stable in the face of changing environments, like in fluid flow[22]. In addition, synergies can emerge between different microbial species, ultimately accomplishing functions that benefit the whole ecosystem. This is the case for stream biofilms: these diverse communities, comprising countless microorganisms, are involved in the cycling of organic matter, ecosystem respiration or capture of contaminants[25].

Unfortunately, the resilience of biofilms also makes them a major concern for human society. Owing to their encapsulation in EPS matrix, biofilms are shielded from a variety of external threats such as UV exposure, phagocytosis or antimicrobials[22]. Reduced metabolic activity within the core of biofilms also decreases the efficacy of treatment with bactericidal compounds that require active growth of the cells[26]. As a result, biofilms can pose problems in industrial settings, for example by disturbing flow in pipes or by forming on the hull of ships, accelerating corrosion and creating drag that will dramatically increase fuel consumption[11,25,27]. In fact, a recent publication reports a global economic impact of biofilms reaching almost \$4000 billion in 2019[28].

Biofilms can also form on the surface of medical devices or on human tissues (Figure 1.5), thereby causing infections that are difficult to treat[22]. As many as 65-80% of infections in humans are thought to be associated with biofilms[29]. One typical example is infective endocarditis. Often caused by streptococci, these biofilms manifest as layers of bacteria that accumulate in blood clots when the cardiac valve endothelium is damaged[22]. As described above, this high shear environment is an especially fertile ground for the formation of thick and strong biofilms[16]. *Ex vivo* antibiotic treatments of these aggregates require doses that are 150 times higher than the minimal bactericidal concentration for planktonic cultures[30]. Even more worrisome, antibiotic therapies that fail to eradicate the whole population foster the development of antibiotic resistance[31]. The latter is considered as one of the biggest threats to global health by the World Health Organization[32].

In the next section, I will discuss biofilms that form inside human hosts, with a particular focus on the context of mucus, which is the first barrier encountered by many microbes entering our bodies.
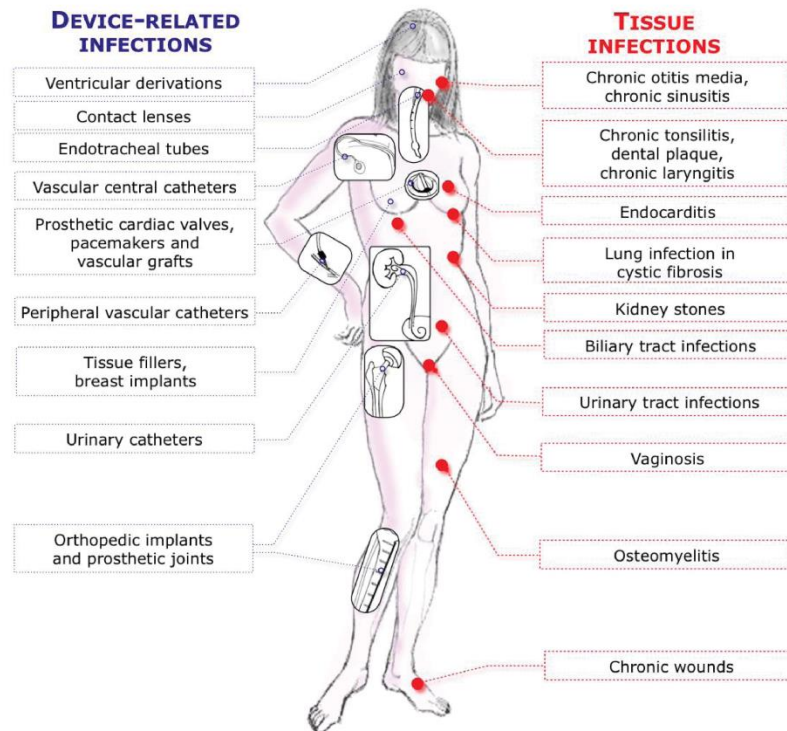
Figure 1.5: Biofilms infections in the human body.
In infectious settings, biofilms either form on medical devices or directly on host tissue. From [29].

1.3 Human mucosal biofilms

The human body possesses various mucosal tissues, which are coated with a secreted viscoelastic substance called mucus. While the exact properties of mucus differ across mucosal sites, some important features are conserved. In terms of composition, for example, the main solid constituents of mucus are large, polymeric glycoproteins called mucins[33]. Their protein backbone displays repeats of proline, threonine and serine, which become heavily glycosylated when mucins are processed through the Golgi apparatus[34]. Upon secretion by mucosal epithelial cells, glycosylated mucins form a crosslinked network retaining up to 1000 times their mass in water[35], which gives rise to the gel-like properties of mucus. Both the mucins and their glycosylation patterns are diverse, and as a consequence each mucosal site in the body has a specific signature, which is often altered in disease[33]. In addition to mucins and water, mucus can also contain DNA, lipids, antimicrobial

peptides…[36,37]. Because of its variable chemical composition, but also because of the diverse environmental conditions (pH, ion concentration…), mucus exhibits different mechanical properties across locations of the body[33]. For example, its viscosity increases as pH decreases; consequently, stomach mucus is particularly stiff, which likely helps protecting the underlying cells against gastric acid[33] (Figure 1.6a).
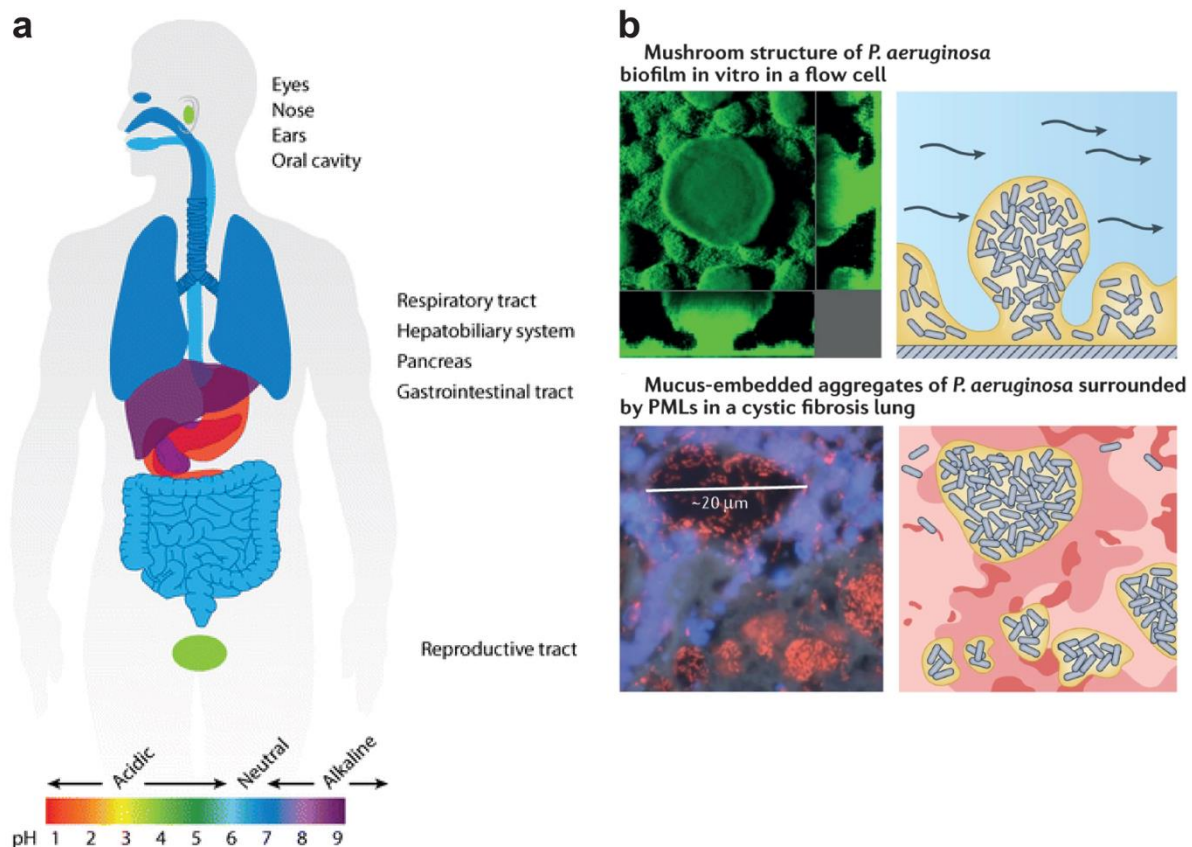
Figure 1.6: Mucus and mucus-associated biofilms.

(a) Mucus properties vary across different parts of the body, for instance in terms of pH. From [33]. (b) The architecture of bacterial biofilms (here *P. aeruginosa*), can differ dramatically between *in vitro* and *in vivo* settings. It is thus crucial to study them in an appropriate model system. From [11].

As they colonize the human body, bacteria have to contend with the complex properties of mucus and associated clearance mechanisms. This may translate into using mucus as a substrate for biofilm formation. For example, commensal streptococci form microcolonies at the middle ear mucosa, which protects them against flow and immune cells[38]. Similarly, commensals like *Bacteroides* form biofilms at the gut mucosa[39]. However, pathogens can also take advantage of the

protection conferred by biofilms to persist at the mucosal surface during infection, for example in inflammatory bowel disease[40], bacterial vaginosis[41] and cystic fibrosis (CF)[42]. In CF, mucus mechanics are significantly altered: at low shear rates, CF mucus reaches bulk viscosities 5 to 50 times larger than healthy mucus[36]. How bacteria interact with airway mucus in health and disease is still not fully understood. Tackling this issue was part of my PhD work, as will be described in upcoming chapters.

Given the importance of mechanical inputs on bacterial physiology and behavior, both at the single cell and community levels, we anticipate that mucosal mechanics impact biofilm formation and bacterial virulence. The architecture of biofilms forming on human mucosal surfaces also differs from those colonizing abiotic materials[43]. Consequently, it is crucial to use the appropriate experimental model for biofilm studies. In the next section, I will review the most commonly used setups for biofilm research.

1.4 Experimental systems for biofilm studies

Both *in vivo* and *in vitro* experimental systems are routinely used to study biofilms. While *in vivo* models are valuable to investigate the response of a whole organism to infections with biofilm-forming bacteria, they also prevent the use of high spatiotemporal-resolution monitoring techniques. Since understanding biofilm formation dynamics in realistic contexts was the main goal of my PhD, animal models were not an option. I will therefore focus on *in vitro* systems.

The simplest *in vitro* biofilm models are static systems, like microtiter plate assays and the related Calgary biofilm device[29,43]. Such methods typically rely on measurements of total biomass with crystal violet or live/dead stains. As a result, they allow for high-throughput experiments. More complex information can be obtained from flow cell setups, which are better-suited for microscopy, at the expense of throughput. While original flow cells were large and therefore required substantial volumes of liquid, microfluidic chips and precision pumping systems are nowadays available. These reduce the necessary amount of medium, facilitate microscopy and enable some degree of parallelization. In addition, the design of microfluidic chips can be customized, so that biofilm

formation can be studied in environments with various geometries[23,44–46]. Even more complex *in vitro* biofilm models are available: termed "microcosms", those setups may include several bacterial species, or specific materials, such as hydrogels and cells to emulate host tissues[29].

Each of these systems has its advantages and limitations. The choice of model thus obviously depends on the scientific question one wishes to address. Microfluidic chips are well-suited to study the effect of a given set of parameters – e.g. fluid flow velocity – on the architecture of biofilms growing on abiotic surfaces. However, since biofilm shape and size differ substantially between *in vitro* and clinical settings[43,47], microcosms are more appropriate than abiotic substrates to investigate the biofilms found in infections (Figure 1.6b).

During my PhD, I used both microfluidic and microcosm-like setups in order to investigate biofilm formation in realistic contexts. In the next section, I will describe the aims of my PhD in more details, as well as how I chose or developed experimental systems to meet these goals.

1.5 Motivation and aims of the thesis

Physical interactions between bacteria and their environment remain understudied, mainly due to technical obstacles. Inaccessibility and complexity of the environment limit our ability to monitor biofilm formation in space and time at high resolution. As a result, new model systems reproducing natural environments and their mechanical properties are necessary for microbiological studies in realistic contexts.

During my PhD, I first focused on biofilm formation in aquatic environments. For this, I studied how the freshwater bacterium *Caulobacter crescentus* associates with surfaces in different flow conditions. Surface colonization patterns are tightly intertwined with social interactions occurring between different microbial strains or species. For instance, contact-based competition can prevail when non-kin cells are in close proximity. By applying selective pressure, social interactions constitute a driving force behind evolution. It is thus important to understand the role that environmental factors play in shaping bacterial communities. To this end, I fabricated microfluidic channels and applied fluid flow to mimic a range of aquatic environments, as described in Chapter

2. I used fluorescence microscopy and image analysis to study the effect of flow velocity on surface colonization patterns such as cluster growth rate and mixing. This allowed to demonstrate that a cellular advection-diffusion mechanism governs the organization of *C. crescentus* communities. Consequently, environmental mechanics may have a strong influence on microbial evolution.

Flow is also ubiquitous within human tissues, such as in the lungs, where beating cilia transport mucus along the airway epithelium. As a result, in healthy individuals, mucociliary flow propels pathogens out of the airway. However, illnesses like CF and chronic obstructive pulmonary disease (COPD) reduce the efficacy of this defense system, thereby increasing sensitivity to respiratory infections. Abnormal biophysical properties of mucus are a hallmark of these diseases. Sick individuals harbor thickened and dehydrated mucus that is harder to clear. Nevertheless, the mechanisms by which mucosal mechanics impacts bacterial colonization and pathogenicity remain to be established. Current airway infection models limit our ability to dynamically probe infections. When I started my PhD, model systems that combined relevant airway cell types – including mucus-secreting cells – with high-resolution imaging capability and presence of an air-liquid interface did not exist. Therefore, I set off to develop such a model in order to explore the dynamics of host-pathogen interactions in the respiratory tract. In Chapter 3, I detail how I used a combination of microfabrication and tissue-engineering techniques in order to build what we called AirGel – an optically transparent, cylindrical chip lined with human airway epithelial cells. I demonstrated that, when grown in AirGel chips, these cells formed a tight epithelium and recapitulated the histological signature of the human airway, as well as its mucociliary clearance function.

As shown in Chapter 4, I finally used AirGels to study the interactions between the opportunistic pathogen *Pseudomonas aeruginosa* and airway mucus. This bacterium is a common source of chronic infections in CF patients. Its tendency to form biofilms in the airway makes it especially difficult to eradicate with antibiotic treatments. Understanding the onset of biofilm formation in the respiratory mucosa is crucial for the development of new therapeutic strategies. Being optimized for microscopy, AirGels allow to investigate these mechanisms at high spatiotemporal resolution. Using

fluorescent labels and confocal microscopy, I found out that *P. aeruginosa* was able to contract mucus with its T4P, thereby accelerating the formation of biofilms in the airway.

Overall, my PhD work highlights the importance of faithfully reproducing the biophysical features of the environment in order to understand biofilm formation. Combining engineering methods with high-resolution microscopy and microbiology tools was critical to reach this goal. In my thesis, I will detail these interdisciplinary approaches and demonstrate how they allowed us to answer long-standing questions related to ecology and infection biology.

Chapter 2.   Cellular advective-diffusion drives the emergence of bacterial surface colonization patterns and heterogeneity

This chapter focuses on the effect of fluid flow on bacterial colonization patterns in aquatic environments. It has been published in Nature Communications (10), Article number: 2471 in June 2019, as:

Affiliations:

Tamara Rossy & Alexandre Persat: Institute of Bioengineering and Global Health Institute, School of Life Sciences, École Polytechnique Fédérale de Lausanne, Lausanne, 1015, Switzerland.

Carey D. Nadell: Department of Biological Sciences, Dartmouth, Hanover, NH, 03755, USA.

Author contributions:

T.R., C.N., and A.P. conceptualized the study, T.R. performed the experiments and data analysis. T.R., C.N., and A.P. wrote the paper.

2.1 Abstract

Microorganisms navigate and divide on surfaces to form multicellular structures called biofilms, the most widespread survival strategy found in the bacterial world. One common assumption is that cellular components guide the spatial architecture and arrangement of multiple species in a biofilm. However, bacteria must contend with mechanical forces generated through contact with surfaces and under fluid flow, whose contributions to colonization patterns are poorly understood. Here, we show how the balance between motility and flow promotes the emergence of morphological patterns in *Caulobacter crescentus* biofilms. By modeling transport of single cells by flow and Brownian-like swimming, we show that the emergence of these patterns is guided by an effective Péclet number. By analogy with transport phenomena we show that, counter-intuitively, fluid flow represses mixing of distinct clonal lineages, thereby affecting the interaction landscapes between biofilm-dwelling bacteria. This demonstrates that hydrodynamics influence species interaction and evolution within surface-associated communities.

2.2 Additional background

Biofilm formation is among the most important and widespread survival strategies found in the bacterial world[10]. This process occurs when microorganisms navigate and attach to surfaces, embedding themselves and their progeny in a matrix of EPS that confer multiple competitive advantages. Owing to the adhesive properties of the EPS matrix, biofilms help bacteria stably reside at surfaces with access to metabolic resources. This multicellular lifestyle also provides cells with a physical shelter, reducing population erosion in flow environments[25], increasing resistance to chemical stressors such as antibiotics[48], and limiting the invasion of bacterial and viral competitors within the community[49,50].

The spatial structure of biofilms is heterogeneous and dynamic[24]. Natural biofilms are thought to commonly include multiple strains and species that can be organized in a variety of three-dimensional patterns. For instance, dental plaque biofilms comprise multiple genera enclosed in a single structure with varying shape and clonal density at different spatial scales[51]. The spatial

arrangements of such multi-species consortia can dramatically impact evolution of cell-cell interactions, and vice versa[24]. The expression of social phenotypes leads to the constant remodeling of biofilms: some strains are killed or constrained to regions with poor nutrient availability, while others may gain access to nutrient-rich space[52].

During surface colonization, bacteria must contend with a wide range of mechanical forces generated in contact with interfaces under fluid flow[1]. Despite their importance in the establishment of biofilms in the natural environment, their contributions to colonization patterns and biofilm architecture are not well understood. As one might suspect, hydrodynamic forces can disrupt biofilms, promoting removal of biomass from surfaces[27]. Less intuitively, fluid flow can promote unusual biofilm structures such as streamers, leading to sudden clogging of fluidic systems[45], affect the cellular organization of single cells within the biofilm[53] or alter the evolutionary dynamics of matrix secretion[23].

Bacterial motility plays a key role during early biofilm growth, for example as single cells increase their rate of encounter with surfaces by swimming[54–57]. However, the joint roles of fluid flow, motility and bacterial surface interactions have only just begun to receive attention[58]. Given the importance of fluid flow in remodeling biofilms and in transporting planktonic cells or aggregates, we anticipate that such forces also modulate spatial organization of surface associated bacterial collectives on many scales.

Most microbes have evolved cellular components optimizing their interactions with surfaces[1,3,48]. *C. crescentus* is particularly well-adapted to life on surfaces under flow: a polar stalk and adhesive holdfast confer strong attachment, and its curved morphology promotes biofilm formation in flow[17,59]. During the process of growth on surfaces, *C. crescentus* mother cells asymmetrically divide into a non-motile stalked cell that stays put on the surface and a daughter swarmer cell that may either attach to the surface of be carried by the flow[60]. The characteristic curved shape of *C. crescentus* promotes local surface colonization by reorienting the body of sessile mother cells in the direction of the flow, so that the piliated pole of the daughter cell is close to the surface. Relative to mutants with

straight cell shape, this process accelerates accumulation of biomass near the founder cell, leading to the formation of clonal microcolonies[17,54,61,62]. During sessile division in flow, daughter swarmer cells may either attach immediately downstream of their mother cell or explore the surrounding fluid to later reattach. The former depends on cell shape while the latter must depend on fluid transport mechanisms and cell motility. The relative importance of these surface colonization modes will, we predict, dramatically influence the basal architecture and cell lineage structure of nascent biofilm populations.

Here, we sought to answer how hydrodynamic forces affect *C. crescentus* biofilm architecture and spatial lineage structure. Using microfluidics and fluorescence microscopy, we explored how the intensity of transport by flow could modulate patterns of surface occupation. Our results indicate that increasingly fast fluid flow shifts surface occupation away from flagellum-driven exploration, and contributes to the formation of larger, more segregated colonies. Using insights from mass transport phenomena, we propose a model based on diffusion and advection describing how hydrodynamics influence initial surface colonization. Finally, we demonstrate that the balance of between flow transport and swimming of planktonic cells strongly modulates the spatial organization of distinct bacterial clones, thereby driving biofilm heterogeneity, which in turn may impact the evolution of social phenotypes.

2.3 Results

2.3.1 Flow modulates bacterial surface colonization patterns

We initially sought to investigate the contributions of fluid flow to surface colonization patterns. We first grew *C. crescentus* biofilms in different hydrodynamic conditions by exposing surface-associated cells to controlled flow in microfluidic channels. We observed striking differences in morphologies in the emerging sessile populations as a function of flow speed. In relatively weak flow (2 mm.s^{-1}), *C. crescentus* rapidly colonized the surface of the channel without forming well-defined colonies (Figure 2.1a). In contrast, spatial patterns of colonization emerged in strong flow (27 mm.s^{-1}), where biofilms grew into sparse, dense microcolonies (Figure 2.1b). Surface occupation

dramatically dropped for growth at mean fluid velocity higher than 4 mm.s^{-1} (Figure 2.1c versus Figure 2.1d-e, and Figure 2.1f).
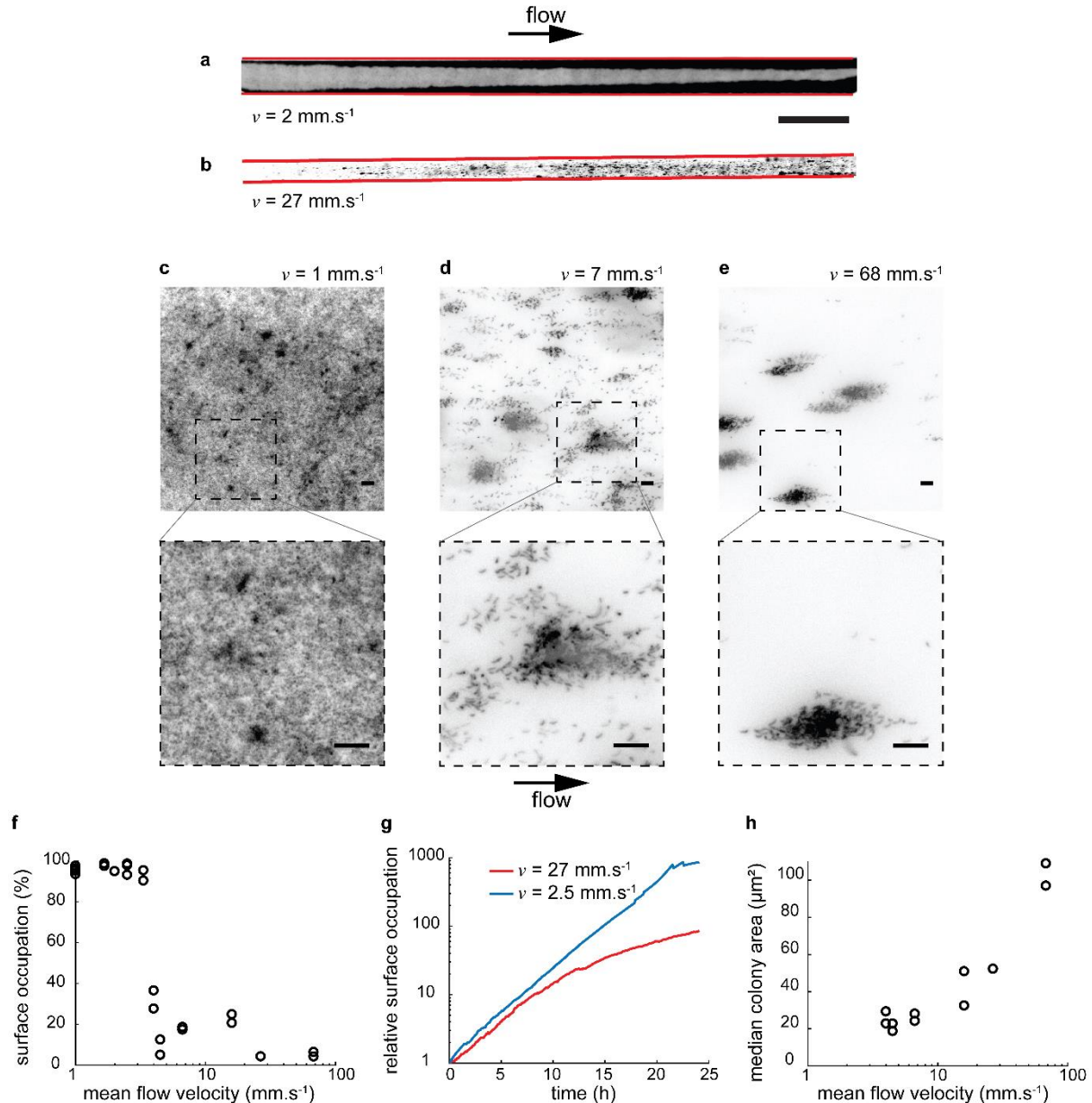
Figure 2.1: Flow modulates *C. crescentus* colonization patterns.

(a-b) Top view, grayscale display of fluorescence microscopy images of *C. crescentus* after 48h exposure to fluid flow in microchannels (cells are shown in black over a white background). In strong flow (b), biofilms grow into patterns of discrete cell clusters, unlike in weak flow (a). The edges of the microchannel are highlighted in red. Scale bar: 1 mm. (c-e) Colonization patterns at the channel centerline at three representative flow velocities, after 24h of colonization under flow. In weaker flow (c), the channel surface is nearly saturated. At intermediate flow (d), multicellular clusters are surrounded by smaller groups or single isolated cells. In strong flow (e), biofilms grow mainly as multicellular clusters. Scale bars: 10 μm. (f-h) Fluid flow modulates kinetics and pattern geometry during surface colonization. (f) Surface occupation after 24h of growth as a function of mean flow velocity. Each data point corresponds to an individual experiment. (g) Surface occupation over time for two representative flow velocities. (h) Median microcolony area after 24h of growth as a function of mean flow velocity.

Surface colonization was also found to be faster in weak flow than in strong flow (Figure 2.1g). Visualization at higher spatial resolution highlights the presence of many isolated single cells in intermediate flow (Figure 2.1d), which are absent in stronger flows (Figure 2.1e). As a result, clusters are generally small in weak to intermediate flow (median cluster area < 40 µm^2), in comparison to strong flows (median cluster area > 100 µm^2) (Figure 2.1h). Thus, flow promotes the emergence of multicellular patch-like patterns at the channel surface but slows down surface occupation.

2.3.2 Swimming motility promotes surface colonization

During asymmetric division, *C. crescentus* releases unattached progeny into the fluid bulk (Figure 2.2a). By visualizing surface colonization dynamically, we observed that, in strong flow, biofilms develop from single founder cells (Supplementary Movie 2.1). Conversely, in weak flow, new founder cells frequently attach to the surface, speeding up the overall rate of colonization and homogenizing surface coverage (Supplementary Movie 2.2 and Figure 2.1g). We thus suspected that the relative contribution of random spatial exploration by swimming motility, and flow transport may enable reattachment. To demonstrate this, we abolished swimming motility by deleting the flagellar gene *flgE*. For this mutant, flow is the dominant transport mechanism of swarmer cells. Figure 2.2b shows a comparison between biofilms formed by wild-type (WT) and *flgE*⁻ in weak flow. In contrast to WT, flagellum-less cells colonize the surface into patch-like patterns and single isolated cells are rare, reminiscent of the patterns observed with WT in intermediate flow (Figure 2.1d). While the obvious effect of a *flgE*⁻ mutation is loss of motility, recent work indicates that these can affect the regulation of holdfast synthesis[62,63]. We thus tested whether the distinct biofilm patterns observed between WT and *flgE*⁻ cells could indeed be attributed to differences in motility rather than in adhesive properties. We already know that the proportion of swarmer cells attaching to the surface immediately after division is similar between WT and *flgE*⁻, suggesting that these distinct patterns are not a result of differences in adhesion between the two strains[17]. To further confirm that this difference in pattern formation between WT and *flgE*⁻ is in fact due to motility, we compared the ability of WT and *flgE*⁻ to attach to the surface in flow. We performed these attachment experiments using synchronized populations of WT and *flgE*⁻ swarmer cells by connecting the outlet of a microchannel colonized with

a 40-hours-old biofilm to the inlet of a new microchannel. These measurements show that while WT cells are able to reach and attach to the surface at low flow, *flgE⁻* cells only rarely attach to the surface of the channel independently of flow velocity (Supplementary Figure 2.1). Altogether, these observations demonstrate that the colonization patterns generated by *flgE⁻* are caused by a loss of swimming motility through a decrease in effective diffusion across the flow direction. Thus, motility plays a critical role in controlling surface occupation density and distribution.
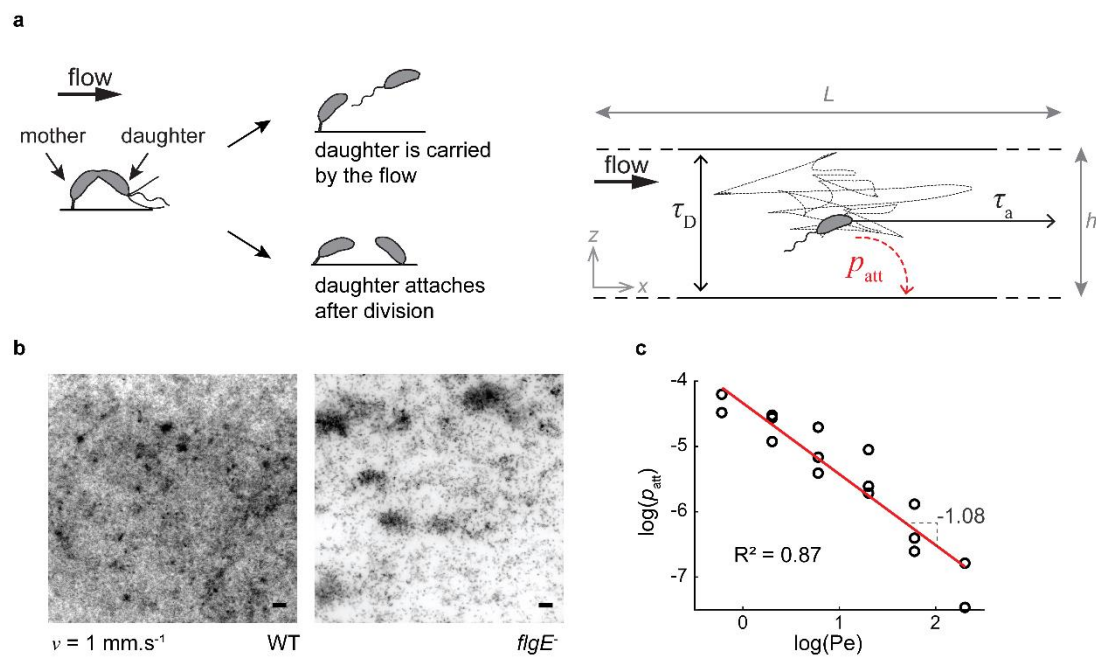
Figure 2.2: Physical mechanism for modulation of *C. crescentus* biofilm architecture.
(a) *C. crescentus* divides asymmetrically: the mother cell is anchored to the surface and undergoing division. At the time of division, a daughter cell can either attach to the surface or be carried by the flow. If attachment occurs, the daughter immediately synthesizes a holdfast contributing to clonal expansion on the surface. If the daughter cell does not attach to the surface, it is subject to: (i) advective transport by fluid flow and (ii) diffusion-like transport generated by unbiased swimming. (b) Contribution of bacterial motility to surface colonization patterns. Fluorescence microscopy images of wild-type (WT) or flagellum-less (*flgE⁻*) *C. crescentus* after 24h exposure to fluid flow (1 mm.s⁻¹). Surface colonization by the *flgE⁻* mutant is slower and less saturated than WT. This qualitatively recapitulates the results observed in stronger flow for WT. Scale bars: 10 µm. (c) Attachment probability (attachment rate normalized by total bacterial flux) as a function of the Péclet number (Pe) on a logarithmic scale. A linear fit of the data indicates swarmer adhesion probability scales with Pe⁻¹, as suggested by our advective-diffusion model.

2.3.3 An advective-diffusion model for surface colonization

Fluid flow transports bacteria directionally along streamlines, whereas cells swim in diffusive, Brownian-like trajectories in the absence of chemical gradients[64]. We therefore drew an analogy with advective-diffusion transport problems: the balance between flow-driven advective transport of

single cells and their diffusive flagellar motility must contribute to the distinct colonization patterns observed in our experiments. We thus developed a scaling for the probability of attachment of a free-swimming bacterium as a function of fluid velocity by reasoning in terms of timescales. Fluid flow transports swarmer bacteria from their division site towards the channel outlet in a characteristic time $\tau_\mathrm{a} = L/v$, where L is the microchannel length and v the mean flow velocity. During this time, a cell explores the depth of the channel by swimming, effectively diffusing in the direction perpendicular to the surface with characteristic timescale $\tau_\mathrm{D} = h^2/D$, where h is the channel height and D the effective diffusion coefficient of a bacterium attributed to unbiased swimming[64]. The probability that a free-swimming bacterium reattaches to the surface depends on the ratio of these two timescales: $\tau_\mathrm{D}/\tau_\mathrm{a} = (h^2 v)/(DL)$, a non-dimensional quantity resembling a Péclet number (Pe), which measures the relative contributions of advective to diffusive transport[65,66]. At large Pe ($\tau_\mathrm{a} \ll \tau_\mathrm{D}$) cells are rapidly washed out of the channel before encountering the surface so that the probability of attachment is low. In contrast, at very low Pe, diffusion dominates over flow; a planktonic cell has sufficient time to reach the surface before being flushed out of the channel, and may eventually reattach to the surface away from its stalked parent (high attachment probability). To validate this scaling, we flowed planktonic cells in microchannels and measured the attachment rate of WT cells as a function of applied flow velocity, effectively tuning Pe. We counted the number of cells attaching onto the surface per unit time, and estimated the corresponding p_att by normalizing the rate of attachment with the incoming flux of cells. We found that attachment probability scales with Pe[-1] (Figure 2.2c), which is consistent with the advection-diffusion model, validating our physical explanation of surface colonization patterns and rates.

2.3.4 Flow modulates clonal lineage structure

While patterns of surface colonization are crucial for initiating biofilm growth, they can also set the foundation for clonal lineage structure, a key factor influencing the evolution of microbial interaction traits[24]. The mechanisms by which environmental conditions, such as fluid flow, and microbial response to these factors influence the spatial architecture of polymicrobial communities, however, are still unclear.
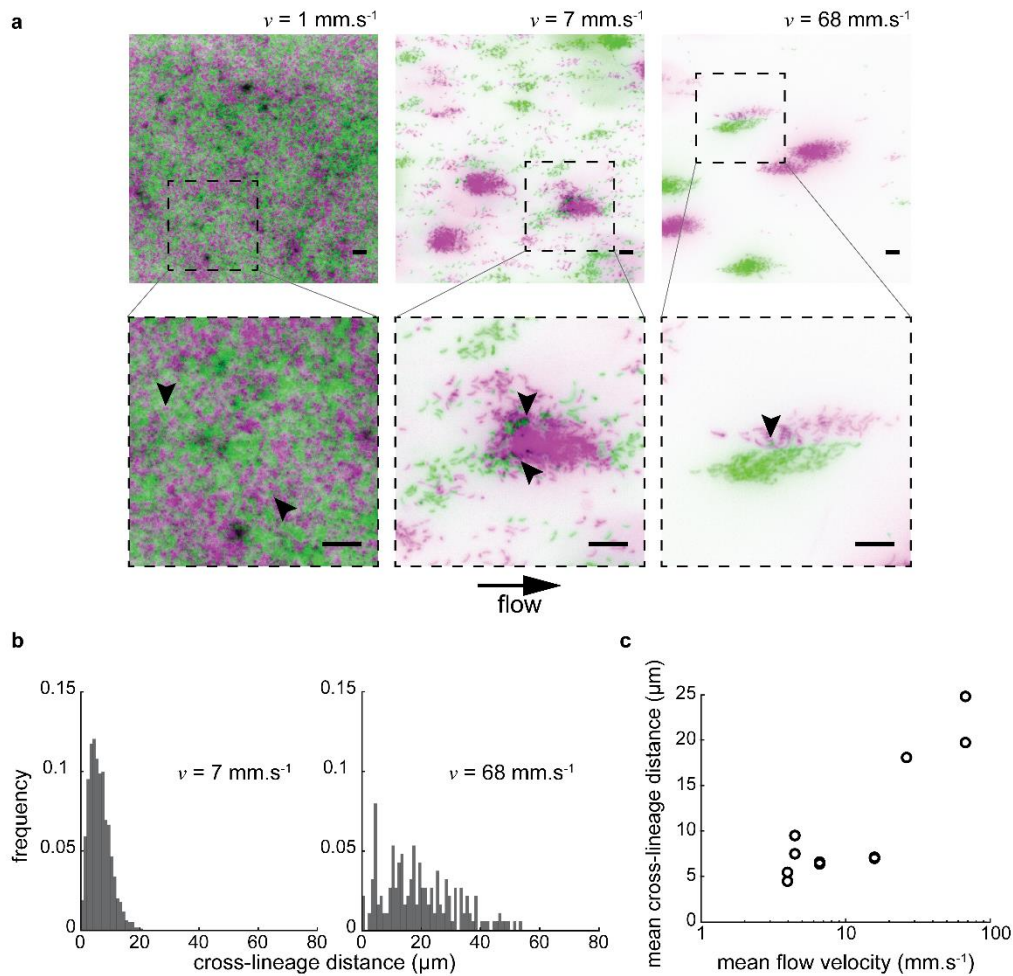
Figure 2.3: Flow modulates clonal structuring of *C. crescentus* biofilms.

(a) Fluorescence microscopy images of *C. crescentus* biofilms (24h). Two populations at equal density, expressing either mKate or Venus fluorescent proteins, were initially loaded in microchannels. The bottom row of images highlights the presence of invading cells (indicated by black arrowheads) within otherwise clonal clusters. Green: *C. crescentus* mKate. Magenta: *C. crescentus* Venus. Scale bars: 10 µm. (b) Distribution of cross-lineage colony distances (i.e. distance between green colonies and their nearest magenta neighbor, and vice-versa) for two representative mean flow velocities (7 mm.s⁻¹ and 68 mm.s⁻¹). The distribution broadens as flow velocity increases. (c) Cross-lineage colony distance, which can be used as a measure of clonal segregation, as a function of mean flow velocity. As flow velocity increases, the mean cross-lineage distance increases, indicating that biofilm mixing decreases.

In mass transport phenomena, the balance between advective and diffusive transport strongly influences mixing of fluids and solutes[66]. By analogy, we reasoned that since surface occupation by *C. crescentus* is governed by advective diffusion, flow may also impact the mixing of distinct cell lineages and their social interactions. We grew *C. crescentus* biofilms in various flow conditions, starting from a one-to-one mixture of strains constitutively expressing mKate or Venus fluorescent proteins whose doubling times are identical[17] (Figure 2.3a). Consistent with advective-diffusion

transport, surface populations of mKate- and Venus-expressing cells were well mixed in weak flow. There was no clear region where clonal lineages were segregated at scales larger than 10 µm. Within seemingly homogeneous clonal groups of cells, we could generally find invaders expressing the other fluorescent protein. At higher flow velocity, clonal groups were larger and segregated from each other, suggesting that they originated from a single parent cell.

The distribution of cross-lineage colony distances effectively measures segregation and thus strongly depends on flow intensity: in intermediate flow, all colonies expressing a given fluorescent protein are at most ~20 µm away from their nearest counterpart (Figure 2.3b). The distribution is heavily weighted at low values of nearest neighbor distance (standard deviation = 3.5 µm). In contrast, at high flow intensity, the distribution of cross-lineage colony distances broadens dramatically (standard deviation = 12.8 µm). Colonies from each color variant can be separated by as much as 50 µm, and there is a substantial decrease in the frequency of small intercolony distances. This shift in distribution occurs progressively as flow intensity increases: the mean cross-lineage distance indeed increases as a function of mean flow velocity, demonstrating that segregation strengthens with flow (Figure 2.3c). We hypothesized that, at low Pe, motility drives diffusive swimming trajectories to promote clonal mixing. We confirmed this by observing a reduction of clonal mixing of flagellum-less mutant at low flow intensity compared to WT (Figure 2.4a). Consistent with this, in competition experiments between WT and $flgE^-$, WT cells commonly invaded the biofilms of the non-motile mutant, but the opposite was very rare (Supplementary Figure 2.2). At high Pe, flow represses mixing of clones by carrying planktonic cells far from their parent, so that the spatial arrangement of WT and $flgE^-$ are similar (Figure 2.4b). Together, these observations are consistent with a model where the balance between advection and diffusion of planktonic cells and deposition of daughter cells adjacent to their points of origin dictates the level of clonal structure within nascent *C. crescentus* biofilms (Figure 2.4c).
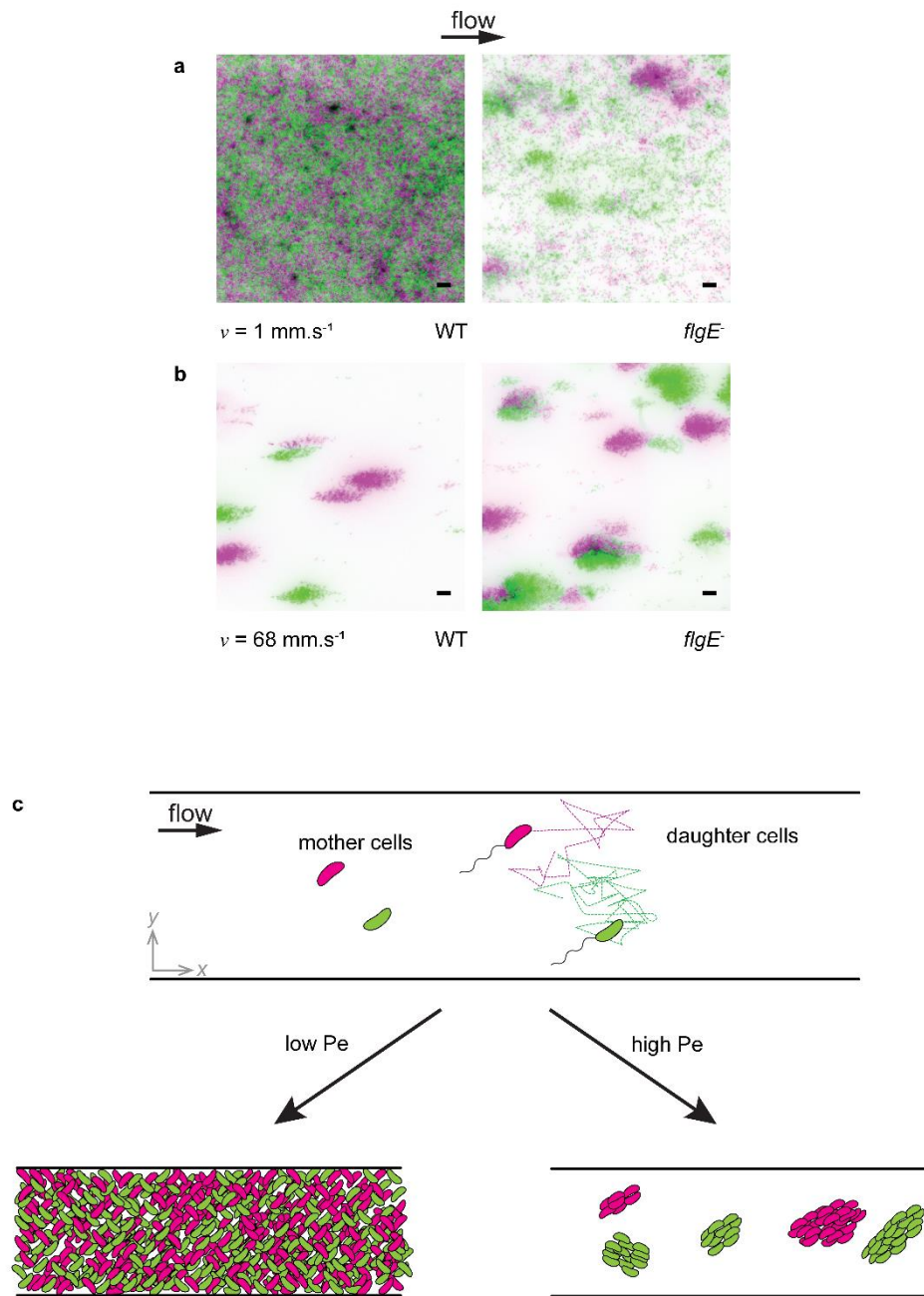
Figure 2.4: Impact of motility on the spatial structure of cell lineages.

Fluorescence microscopy images of wild-type (WT) or flagellum-less (*flgE*) *C. crescentus* after 24h of growth in a microchannel under low (1 mm.s⁻¹) or high (68 mm.s⁻¹) flow. Two populations at equal density, expressing either mKate or Venus fluorescent proteins, were initially loaded in microchannels. (a) At low flow, the colonization pattern of *flgE* shows lower surface coverage and larger cluster size than WT. This qualitatively recapitulates the results observed in stronger flow for WT, indicating that flagellum-powered swimming motility contributes to clonal dispersion. (b) Under strong flows, when advective transport dominates over bacterial swimming, WT and *flgE* cells form similar biofilm patterns. Green: *C. crescentus* mKate. Magenta: *C. crescentus* Venus. Scale bars: 10 μm. (c) Within the framework of our model, the ratio of diffusive to advective transport timescales influences heterogeneity of clonal distributions in space. Indeed, Brownian-like single cell trajectories generate dispersion of bacterial clones across the channel surface at low Pe. Strong flows (large Pe) mitigate this effect by increasing clonality.
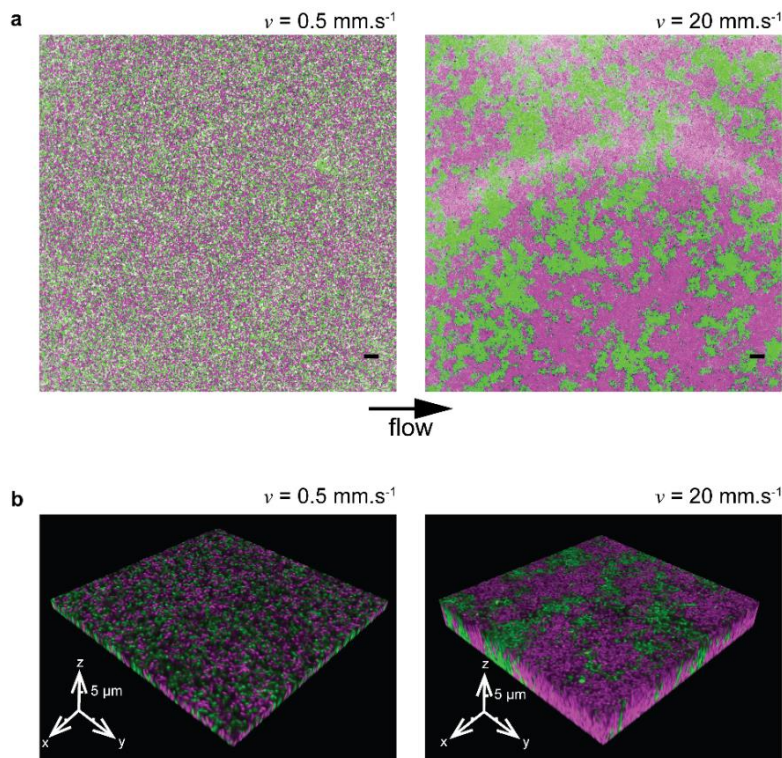
Figure 2.5: Flow-dependent colonization patterns persist on longer time scales and in three dimensions.

Biofilms of *C. crescentus* expressing either mKate or Venus fluorescent proteins, grown under low (0.5 mm.s^{-1}) or high (20 mm.s^{-1}) flow during 6 days. (a) At the channel surface, biofilm mixing patterns after 6 days recapitulate those obtained after 24h (Figure 2.3a). Scale bar: 10 μm. (b) 3D rendering of a z-stack acquisition of biofilms grown for 6 days under flow. Characteristic mixing patterns previously observed on the surface of channel also extend in the third dimension. Green: *C. crescentus* mKate. Magenta: *C. crescentus* Venus.

Finally, we verified that clonal patterns are conserved later in the colonization process, demonstrating that the dependence of biofilm spatial structure on flow is not a sole consequence of differences in colonization kinetics. After 6 days of growth, biofilms in both weak and strong flow regimes covered the surface entirely and extended into the channel depth. These mature biofilms retained the clonal structure set by the initial patterns of surface occupation we observed after 24 h of growth: the spatial distribution of clones remained highly mixed at low flow and relatively segregated at high flow (Figure 2.5a). These differences in cellular arrangement are retained in the third dimension, as clonal clusters observed in strong flow essentially propagate as they grow normally to the channel surface (Figure 2.5b).

2.4 Discussion

Biofilms are permanently subject to the physical forces generated in their microenvironments. In their aquatic lifestyle, they must in particular cope with viscous forces induced by fluid flow. These forces strongly impact many elements of biofilm structure, including their overall morphology[67,68], solute flux into and out of the population[69] and detachment of cell clusters from surfaces[27]. Given the importance of hydrodynamic effects in remodeling biofilms and in transporting planktonic cells or aggregates[53], we anticipated that these forces also modulate spatial organization of surface associated bacterial collectives on many scales.

We demonstrated that the multi-scale feedbacks between surface attachment, daughter cell deposition, fluid transport, and dispersion by diffusion exert a strong influence on the morphological, spatial and genetic structure of biofilm populations. The early stages of surface colonization can set the foundations of subsequent biofilm architecture, influencing the spatial distributions of different strains and species, and the community's interaction networks. One critical ingredient to this process is probabilistic local attachment versus planktonic release of daughter cells. Any species in which extracellular matrix secretion has some likelihood of locally trapping recently divided daughter cells should display similar dynamics. Consistent with this, Martinez-Garcia et al. recently showed using theory and experiments with *Vibrio cholerae* that flow, initial population density, and matrix secretion interact strongly to influence clonal colony size in early biofilm growth[58].

Even in the absence of matrix-mediated daughter cell surface attachment, asymmetries in adhesive properties may very likely appear between two daughter cells that are dividing symmetrically[70]. For example, a memory effect in *Pseudomonas aeruginosa* yields strong differences in the adhesive behavior of two sessile daughter cells, nearly recapitulating the pattern of *C. crescentus*, despite the absence of obvious cellular asymmetry[55,71,72]. Furthermore, the distribution of messenger molecules that regulate the production of matrix components is asymmetric in daughter *P. aeruginosa* cells, potentially differentially affecting adhesive properties[55,71,72]. The same effect may also arise in *Escherichia coli*[70]. The balance between directional advective and random diffusive trajectories of detached planktonic cells constitutes a second ingredient setting the spatial structure of biofilm

communities. In the same manner as transport of particulate matter, a Péclet number can be used to predict the emergence of motility- and flow-induced morphological transitions. Advective-diffusion has been employed to model the dispersion of planktonic bacteria in laminar flow[73], and even the dispersion of airborne plant seeds[74]. Likewise, phase-like transitions between multicellular phases in *Myxococcus xanthus* can be described using a Péclet number quantifying the relative contribution of directional cell displacement to rotational diffusion[75].

The distinction between spatial segregation versus mixture of distinct clonal lineages is of key importance to the expected evolutionary trajectories of numerous traits, and in particular, traits that exert a fitness impact on nearby cells. These include all contact-mediated interactions as well as helpful or harmful interactions mediated by compounds secreted into the extracellular space. The spatial orientation of genetic lineages and the movement of these compounds, which is also controlled by local fluid transport regime, interact to determine whether these interactive behaviors are evolutionarily stable[24]. Tight clustering of clonemates as occurs under strong flow, for instance, increases the evolutionary stability of locally cooperative phenotypes. On the other hand, antagonistic traits operate most effectively under mixed lineage conditions, when the targets of the harmful phenotype are easily within reach. Our study highlights the importance of the mechanical environment in shaping the foundation of biofilm community architecture at single cell and cell collective length scales. Our model system consisting of *C. crescentus* colonizing flat surfaces in unidirectional flow is minimalistic, but generates insights for the understanding of organization of more complex communities in more intricate mechanical environments. An important future direction will be to recapitulate more ecologically realistic conditions, to understand how flow structure shapes spatial organization of biofilms in environments such as the widely varying host mucosa and rhizosphere[76,77].

2.5 Methods

2.5.1 Design and fabrication of the microfluidic chips

We fabricated the microfluidic chips following standard soft lithography techniques. More specifically, for the 24h- and 48h-long biofilm experiments, we designed 1 cm-long, 500 or 250 μm-wide channels in Autodesk AutoCAD 2018 and printed them on a soft plastic photomask. We then coated silicon wafers with photoresist (SU8 2025, Microchem), with varying thicknesses (25 μm, 50 μm and 90 μm) to allow a wider range of mean flow velocities for identical flow rate settings. The wafer was exposed to UV light through the mask and developed in PGMEA (Sigma-Aldrich) in order to produce a mold. PDMS (Sylgard 184, Dow Corning) was subsequently casted on the mold and cured at 80°C for about 1h30. After cutting out the chips, we punched 1 mm inlet and outlet ports. We finally bonded the PDMS chips to glass coverslips (Marienfeld 1.5) in a ZEPTO plasma cleaner (Diener electronic). To fabricate channels for the 6 day-long biofilm experiments, we followed a similar procedure, but adjusted the dimensions of the channel to leave more space for large 3D structures to form. More precisely, the channel was 2 mm wide, 110 μm high.

2.5.2 Bacterial strains

We used *C. crescentus* strains CB15 constitutively expressing chromosomally-integrated fluorescent protein genes *Venus* or *mKate* off a modified *lac* promoter[17]. These strains were grown in peptone yeast extract (PYE) medium supplemented with 5 μg/ml of kanamycin (PYE-Kan) in a shaking incubator set to 30°C. For the experiments involving non-motile CB15, we inserted either mKate or Venus in the chromosome of the flagellum-less mutant CB15 *flgE*⁻ using plasmids pXGFPC-2 Plac::mKate2 and pXGFPC-2 Plac::Venus respectively[17]. We prepared electrocompetent CB15 *flgE*⁻ by centrifuging 3 ml of stationary phase culture and rinsing it two times with cold Milli-Q water (Merck Millipore). About 600 ng of plasmid were added for transformation and the bacteria were then plated on PYE-Kan plates.

2.5.3 Biofilm growth in microfluidic chambers

At the start of every experiment, the bacterial cultures had an optical density of approximately 0.15 ($\sim$ 4.5$\cdot$10^8 CFU.ml^{-1}). Equal volumes of CB15 mKate and CB15 Venus were diluted in PYE-Kan to a final 1:10 concentration. We then loaded the bacterial mixture in a microchannel using a micropipette, and let them adhere for 3 minutes (WT) or 15 minutes (*flgE*$^-$) before washing the channel with PYE-Kan. For all conditions but the highest flow velocity (v = 68 mm.s^{-1} for 24h biofilms, and v = 20 mm.s^{-1} for 6-day biofilms), we connected the inlet port to a disposable PYE-Kan-filled syringe (BD Plastipak) using a 1.09 mm outer diameter polyethylene tube (Instech) and a 27G needle (Instech). The syringe was then mounted onto a syringe pump (ZS100, ChuangRui Pump). For the highest flow conditions (v = 68 mm.s^{-1} for 24h biofilms, and v = 20 mm.s^{-1} for 6-day biofilms), we connected the inlet port to a PYE-Kan-filled beaker via two imbricated tubes (polyethylene tubing as described above, and Tygon-LFL tubes with an inner diameter of 0.76 mm (Ismatec)). We mounted the setup onto a peristaltic pump (MCP, Ismatec) allowing us to work with larger volumes than the syringe pump. For every experiment, we connected the outlet port to a waste container using polyethylene tubing. We finally placed the chip in a 30°C incubator and applied a controlled flow of PYE-Kan to the microchannels for 24h, 48h or 6 days depending on the experiment. The mean flow velocity (v) was calculated from the selected flow rate (Q) and channel cross-sectional area (A) as such: $v = Q/A$.

2.5.4 Visualization

For all visualizations of biofilms grown up to 48h, we used a Nikon TiE epifluorescence microscope equipped with a Hamamatsu ORCA Flash 4 camera and a 40X Plan APO NA 0.9 objective. The full-channel images were stitched using the NIS-Elements software. All single cell level pictures presented in this work were taken 9 mm away downstream of the inlet. For the timelapse experiments (Supplementary Movies 1 and 2), we acquired images every 5 minutes for 24 hours. To visualize 6 day old biofilms, we used a Leica SP8 confocal microscope equipped with a white laser, a 25X HC FLUOTAR NA 0.95, water-immersion objective, as well as a 63X HC PL APO NA 1.40 oil-

immersion objective for high magnification z-stack acquisitions. We used Imaris (Bitplane) for three-dimensional rendering of z-stack pictures (Figure 2.5b).

2.5.5 Data analysis

Data analysis was conducted using Matlab (Mathworks). To discriminate cells from background, the images were segmented with the built-in Matlab function *imbinarize* using an adaptive threshold (*adaptthresh* built-in Matlab function), the sensitivity of which varied depending on the median intensity of the picture. Similarly, the percentage of background removed was also determined by the median intensity. Finally, we filtered out objects smaller than 15 pixels, since this value was observed to be the minimal area of a single cell standing vertically. After segmentation, pictures were visually assessed to ensure the quality of segmentation. In rare cases (4 pictures out of 50), segmentation was aberrant (*i.e.* the segmented features did not correspond to the bacteria in the raw picture, likely due to uneven background) and the images had to be excluded from the analysis.

To calculate the surface coverage and microcolony area, we merged the segmented pictures originating from mKate and Venus using the logical *or* function. To quantify surface coverage, we divided the area of black pixels (i.e. pixels containing a part of cell) by the total area of an image.

We observed that single cell clusters were difficult or even impossible to discriminate by eye when surface coverage was larger than 80%. Therefore, we only included segmented pictures with a surface coverage ≤ 80% for the measurement of microcolony area. We also filtered out any object smaller than 200 pixels, which approximately corresponds to a group of five cells (average cell size: 1.29 $\mu m^2 \approx$ 40.2 pixels, N = 80 cells). We then closed the pictures using a built-in Matlab function (with a disk structuring element having a radius of five pixels) and calculated the area of every colony. The median colony area was finally calculated for each image.

To quantify the degree of mixing of the biofilms, we again only studied segmented pictures with a surface coverage ≤ 80%. Additionally, unlike for surface coverage and colony area quantification, we analyzed mKate and Venus pictures separately. We closed all the pictures as mentioned above. We then calculated the distance between the centroid of an object and its nearest neighbor

expressing the other fluorescent protein, using the built-in Matlab function *knnsearch*. This operation was repeated for every object in every picture. Finally, the mean cross-lineage distance was calculated for each experimental condition, considering distances from both fluorescently-labeled populations.

2.5.6 Estimation of attachment probabilities

To estimate the attachment probability of swarmer *C. crescentus* in different flow conditions, we flowed CB15 Venus cells in a 500 µm-wide, 90 µm-high microchannel using a syringe pump. The flow rates varied between 0.81 and 270 µl.min^{-1} (mean flow velocities from 0.3 to 100 mm.s^{-1} respectively). Each condition was repeated two to three times. Bacteria were visualized by fluorescence microscopy (one frame recorded every second during one minute) and single attachment events were counted. Bacteria had to remain on the surface for at least 3 consecutive frames at the same location to be counted as attached. The number of bacteria attached over time was plotted for each flow condition and, using a linear fit, we extracted the attachment rate from the slope of these curves. The attachment probability was then computed as follows:

$$p_{\text{att}} = \frac{r}{J \cdot A} = \frac{r}{Q \cdot C} \quad (1)$$

Where *r* is the attachment rate, *C* is the bacterial concentration and *J* is the bacterial flux, defined as $J = (Q \cdot C)/A$. Normalization by the bacterial flux is necessary, because the number of bacteria going through the channel during a given time depends on flow rate. Also note that the bacteria loaded in the channel contained a mixture of swarmer and stalked cells, thus our measurement of p_{att} is underestimated compared to biofilm growth conditions where all planktonic cells are swarmers.

To determine the dependence of attachment on the flow regime, we plotted the logarithm of p_{att} as a function of the logarithm of Pe. As defined above, $\text{Pe} = (h^2 v)/(DL)$; we assumed the diffusion coefficient of *C. crescentus* to be equal to that of *E. coli* reported before[64], namely $D = 4 \cdot 10^{-6}$ cm^2.s^{-1}.

We finally determined the proportionality relation between p_{att} and Pe from the slope of the curve, since $\alpha \log(x) = \log(x^{\alpha})$.

For Supplementary Figure 2.1, we generated a population of synchronized swarmer cells. We used a strategy where we connected a biofilm-containing microchannel shedding newly-divided swarmers to a bare microchannel. We loaded a mixture of Venus-expressing CB15 WT and mKate-expressing CB15 *flgE*⁻ cells into a microchannel (channel 1) and let them grow at 30°C during 40h under flow (v = 7 mm.s⁻¹). We then connected the outlet of channel 1 to the inlet of another microchannel (channel 2) using polyethylene tubing. This way, swarmer cells released from the biofilm of channel 1 were transferred to the empty channel 2 at the applied flow rate. For each flow velocity, bacteria were imaged every 2 s for 2 min from which we quantified newly-attached cells at every time frame. Finally, to determine the total concentration of cells, a CFU count was performed. We calculated the relative ratio of WT to mutant cells feeding channel 2 by microscopic observation of the effluent of channel 1. We then adjusted the obtained values for rates of attachment to account for the relative proportions of WT vs *flgE*⁻ cells.

2.6 Supplementary information appendix

2.6.1 Supplementary figures
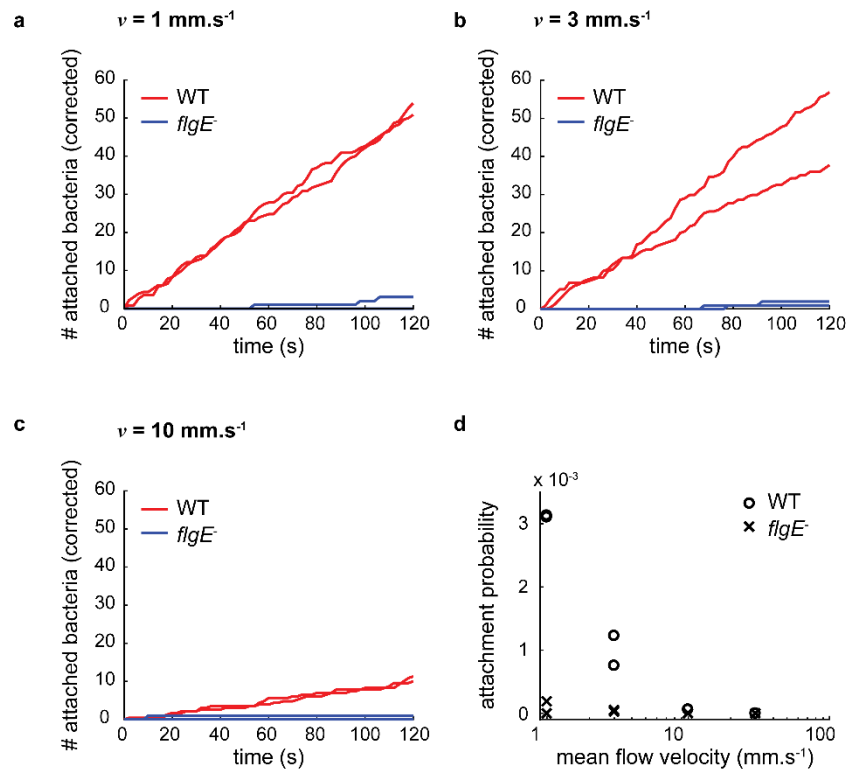
Supplementary Figure 2.1: Rate and probability of attachment as a function of flow speed for WT and *flgE* mutants.

(a-c) We quantified the number of swarmer *C. crescentus* cells (WT in red and *flgE* in blue) that attached to the surface of a microchannel over 2 min at 1 mm. s^{-1} (a), 3 mm.s^{-1} (b) and 10 mm.s^{-1} (c) mean flow velocity. We performed these experiments with a mixture of WT expressing mKate and *flgE* expressing Venus. To normalize the fluxes of incoming bacteria, we divided the number WT cells by the relative abundance of WT to *flgE* cells. (d) Probability of attachment of WT and *flgE* cells as a function of flow velocity. As flow intensity increases, the colonization advantage provided by swimming motility vanishes.

$v = 7$ mm.s^{-1} WT   *flgE*$^-$
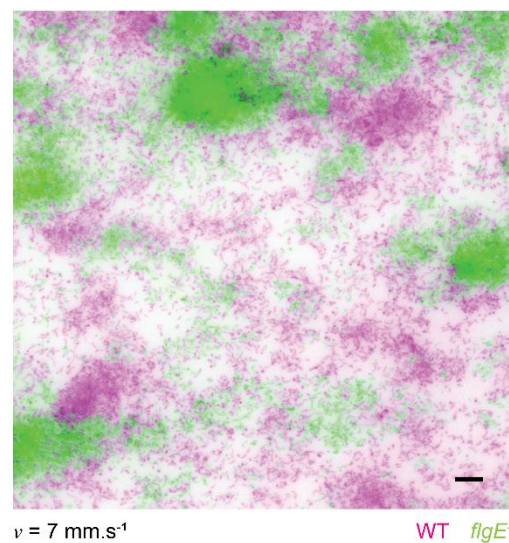
Supplementary Figure 2.2: Competition for surface colonization between WT and *flgE*$^-$ cells.

A mixed population of *C. crescentus* WT (magenta) and *flgE*$^-$ (green) was initially loaded in the microchannel and grown for 24h under intermediate flow (7 mm.s^{-1}). While both WT and mutant colonize the surface in the form of microcolony clusters, the WT strain colonized a larger proportion of the surface with single isolated cells. This allows WT to invade green *flgE*$^-$ microcolonies. *flgE*$^-$ cells colonize a smaller proportion of the surface, mostly as large clonal clusters, but are unlikely to invade WT biofilms.

2.6.2 Supplementary movies

Supplementary movies can be downloaded from: https://www.nature.com/articles/s41467-019-10469-6#Sec16

A description of these movies is available below:

Supplementary Movie 2.1 – *C. crescentus* biofilm in strong flow: timelapse visualization of a *C. crescentus* biofilm growing in strong flow (mean flow velocity: 27 mm.s^{-1}) during 24h. Clonal clusters grow around the cells that were initially attached to the surface, while subsequent attachment of new bacteria is rare.

Supplementary Movie 2.2 – *C. crescentus* biofilm in weak flow: timelaspe visualization of a *C. crescentus* biofilm growing in weak flow (mean flow velocity: 2.5 mm.s^{-1}) during 24h. Single bacteria can frequently attach to the surface, thereby speeding up colonization and leading to the formation of patterns that are less patchy than in strong flow.

Chapter 3. AirGel: a tissue-engineered airway to study respiratory infections

As demonstrated in the previous chapter, mechanical forces can influence bacterial colonization patterns on abiotic surfaces. It is thus reasonable to assume that mechanical properties of human tissues also play a role in modulating bacterial virulence and colonization. In the context of respiratory infections, whether and how mucosal mechanics impact biofilm formation has been a long-standing question. To answer it, airway models enabling dynamic monitoring of host-pathogen interactions are necessary. In this chapter, I will describe how I engineered such a model, with a focus on the requirements and challenges that had to be overcome.

3.1 Additional background

3.1.1 Modeling the respiratory tract

The lower airway consists in a tree-like structure starting with a single branch, the trachea, which splits into several generations of bronchi. The bronchi themselves split into the smaller bronchioles, which finally end with millions of alveoli, where most of the gas exchange occurs[37,78]. Every portion of the respiratory tree is lined by a specialized epithelial layer that constitutes a physical barrier. The exact cell types and ratios composing these epithelia vary in the different sections of the airways. In the proximal parts, like the trachea, large numbers of secretory cells called goblet cells secrete a thick mucus layer that gets propelled out of the airway by the beating action of ciliated cells[37,78]. This mechanism, termed mucociliary clearance (MCC), is the first line of defense against inhaled pathogens. MCC is often altered in diseases like CF, asthma and COPD, which correlates with an increased prevalence of respiratory infections[36]. In many cases, those infections become chronic and biofilms are frequently isolated from the sputum of sick individuals[42,79]. However, how biofilms

form in the human airway is still unclear, mainly because dynamic monitoring of infections *in vivo* is not possible.

Nonetheless, a wide variety of airway model systems have been developed and provide insights into airway physiology in health and disease. Tracheas are frequently explanted from animals as a way to study MCC and mucus architecture[80–85]. Immortalized cell lines like Calu-3, which originate from lung adenocarcinoma, may also be used in bioengineered airway models[86]. However, such cells only poorly recapitulate the histological signature of the respiratory epithelium, and thus, approaches using primary cells directly isolated from human tissues are more promising. Owing to the low number of passages after isolation, these cells retain the potential to differentiate into a tight epithelium containing ciliated cells and goblet cells[87]. Consequently, they have been widely used in various culture systems, like Transwell inserts[88–90] (porous membranes suspended in multi-well plates, allowing for air-liquid interface culture), lung-on-chip devices[91–93] (again comprising a porous membrane, but this time encased in a microfluidic channel) or airway organoids[94–96] (self-assembled spheres of cells embedded in a Matrigel scaffold). Several studies have successfully derived organoids from human induced pluripotent stem cells (iPSCs)[97,98], which has great potential for genetic engineering of airway models and for personalized medicine.

Despite the existence of numerous airway models, when I started my PhD, none of them allowed for dynamic studies of biofilm formation in the respiratory mucosa in a physiologically-relevant manner. For example, mucus in murine models differs from human mucus in composition and properties[80]; piglet models are more accurate, but working with larger animals is obviously more challenging. Tracheal explants, despite allowing dynamic studies to some extent, display a steep decrease in the number of goblet cells after only a few hours in culture, along with signs of apoptosis[99]. Model systems based on porous membranes pose problems for high-resolution microscopy. Finally, organoids often need to be infected by a tedious microinjection process, because their apical side is frequently oriented towards the inside of the sphere; in addition, they do not allow for the establishment of an air-liquid interface (ALI).

As a result, an important part of my PhD consisted in developing a novel system overcoming those limitations. In the next section, I will detail the concept and requirements of this model.

3.1.2 AirGel: concept and requirements

Given that investigating respiratory infections at high spatiotemporal resolution was the main purpose of our new system, we ruled out animal models and opted for an approach combining microfabrication and tissue engineering. In order to faithfully recapitulate the cell populations that make up the human airway mucosa, we decided to use primary human bronchial epithelial (HBE) cells. In addition, we identified a number of requirements in order for our model to fulfill its goal.

The first requirement was to develop a transparent system with relatively low working distance, thereby facilitating microscopic visualization. Second, obviously, the materials used in this airway model should enable long-term cell culture and differentiation. The possibility to establish an ALI was the third requirement, so that infections could be studied in physiologically relevant conditions; this also implies basal access to supply medium to the cells during ALI culture. Finally, apical access to the epithelium was necessary in order to easily inject bacteria.

Consequently, we envisioned a model that we named AirGel, consisting of a tube-shaped cavity inside a transparent hydrogel substrate (Figure 3.1). HBE cells would be grown on the surface of this cavity and ultimately differentiate into ciliated and goblet cells. The lumen would be accessible by open ports in order to both generate the ALI and load bacteria for infection experiments. In the next section, I will discuss the engineering strategies followed to fabricate this model and what challenges had to be overcome.

3.2 Development of the AirGel model system

This part of my PhD project involved extensive optimization of different components of the model in parallel. Therefore, methods, preliminary results and final strategies will be interspersed within the next sections. For the detailed final methods, refer to appendix 3.4.
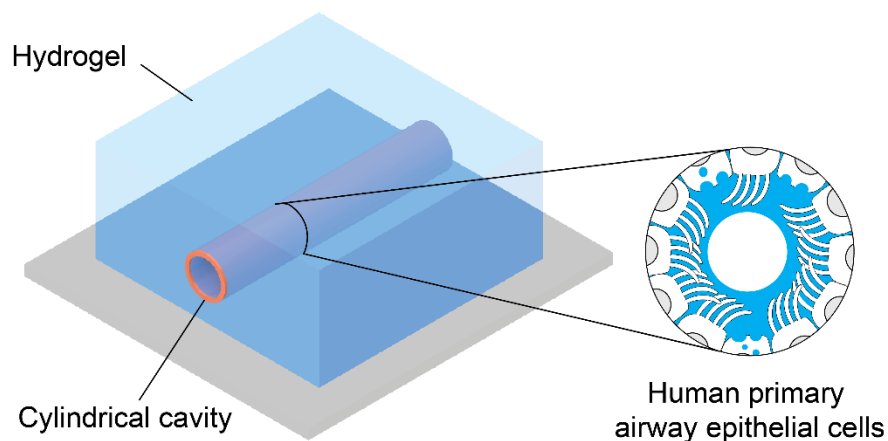
Figure 3.1: Schematic view of the AirGel model.

AirGel consists of an HBE cell-laden cylindrical cavity inside a transparent hydrogel substrate.

3.2.1 PDMS scaffold microfabrication and generation of the hollow lumen

We chose to encase the AirGel model into a PDMS chip, which has several advantages. To name a few: it is widely used in microfabrication processes, it is biocompatible and optically transparent and it can be plasma-bonded to glass. Our original design was strongly inspired by the mini-gut device developed in the Lutolf lab[100]. Briefly, they fabricated a PDMS microfluidic chip with a hydrogel-filled chamber (Figure 3.2a), in which they laser-etched a lumen surrounded by crypt-like structures.

We simply adapted the pattern to be used for laser etching (Figure 3.2b) and grew HBE cells in the resulting lumen (Figure 3.2c). However, this prototype was far from optimal, for several reasons. First, while laser-etching allows for complex designs, such as intestinal crypts, it is also very slow (typically, 1.5h were required to etch a single AirGel prototype). Therefore, it is not the best-suited solution to generate simple features like a straight lumen. In addition, we only have limited control over the shape and dimensions in the Z direction; as a result, it was not possible to achieve a cylindrical structure with the usual protocol from the Lutolf lab. The slowness of the laser etching process also limited the cross-sectional dimensions of the lumen (width: ~450 µm, height: ~ 150 µm), which resulted in large capillary forces and thus very short-lived ALI. Finally, we noted two additional issues related to cell culture and hydrogel composition. I will discuss how we solved them in upcoming sections, but briefly, we observed the following: after 2 to 3 weeks of culture, HBE cells

either invaded the gel (Figure 3.2c) or detached from it (data not shown). Moreover, this prototype did not sustain differentiation into the relevant epithelial cell types, most likely because the small basal reservoirs (Figure 3.2a) did not provide the cells with enough medium.
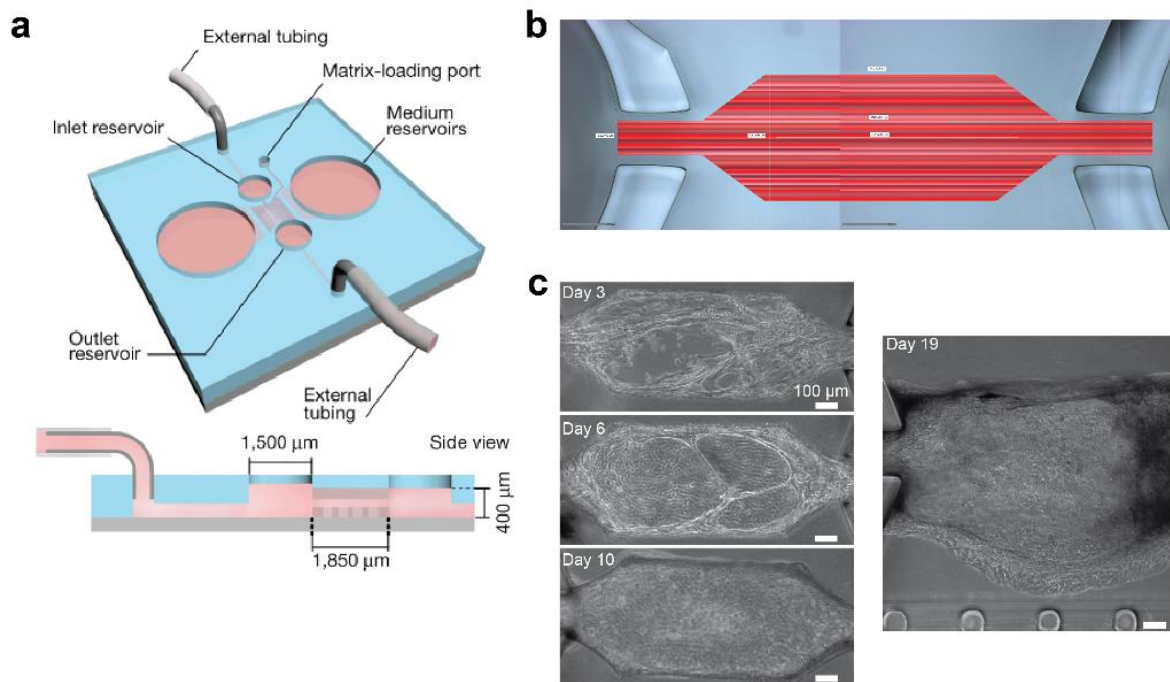
Figure 3.2: AirGel prototype.

(a) Schematic of the Lutolf lab's mini-gut (reproduced from [100]). (b) Pattern used for laser etching of prototype AirGels. We designed a simpler structure than the mini-gut's lumen and crypt design, since the bronchi are straight tubes. Image courtesy of Dr. Mikhail Nikolaev. (c) Initial tests of HBE cell culture in AirGel prototypes.

For all these reasons, I set off to improve the AirGel prototype. The first step was to find a replacement for the laser etching process. A better-suited strategy to quickly generate cylindrical lumens was developed by Jiménez-Torres and colleagues[101]. Their protocol consists in casting the hydrogel matrix around PDMS rods (which are easily fabricated, for instance by curing PDMS inside hypodermic needles). After polymerization of the hydrogel matrix, the rods can simply be removed with tweezers, leaving a tubular cavity behind (Figure 3.3a). In addition to being quick, this process allows for a wide array of sizes. Hypodermic needles are typically found in sizes that range between gauge 10 and 33, which corresponds to inner diameters of approximately 0.1 to 2.7 mm. I opted for gauge 14 (~1.6 mm), because it facilitated ALI maintenance. However, using a rod with such a large diameter also implied building a large hydrogel chamber, at least for microfabrication standards.

Therefore, usual soft lithography protocols were not applicable. To overcome this issue, I leveraged 3D printing technology, which enabled fabrication of large molds (Figure 3.3b) in one simple step. Finally, I also got rid of the basal medium reservoirs. Instead, I filled the glass-bottom dish containing the AirGel chip with 1 ml of culture medium. This ensured sufficient nutrient supply to the cells. A schematic of the resulting AirGel chip is shown in Figure 3.3c.
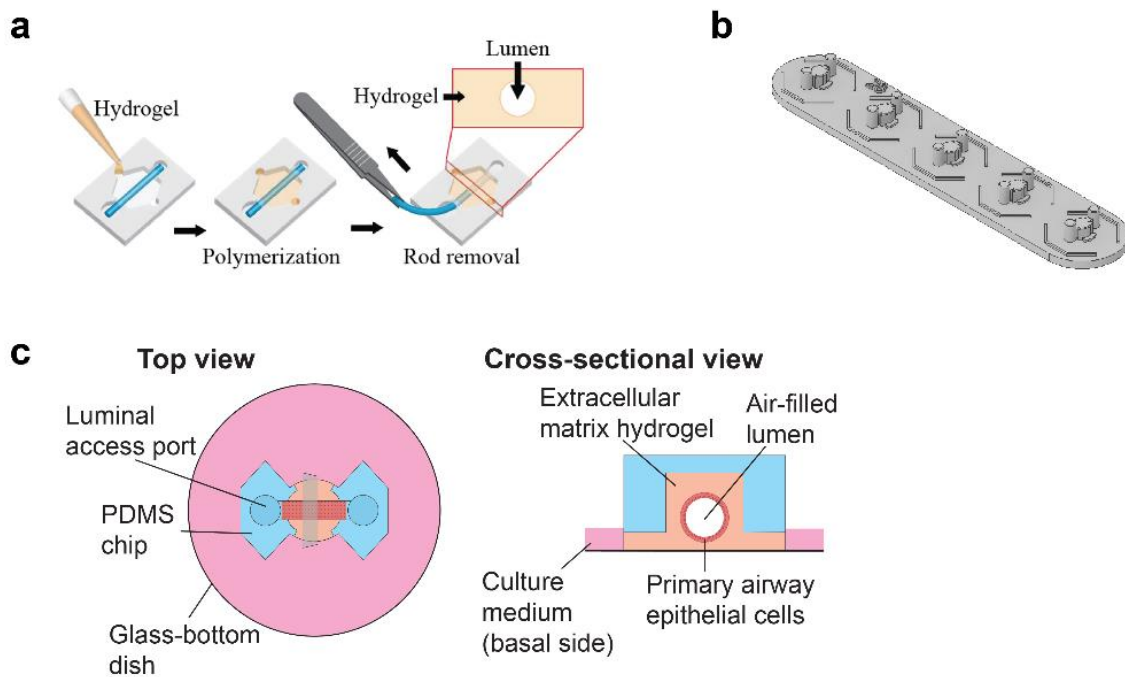
Figure 3.3: AirGel after optimization.

(a) Lumen patterning method developed by Jiménez-Torres and colleagues (reproduced from [101]). (b) 3D printed mold on which PDMS is casted to generate the chip scaffold. (c) Schematic view of the final AirGel model. As shown in pink, the whole surface of the glass-bottom dish is covered in culture medium (1 ml volume), which ensures sufficient nutrient supply to the cells.

3.2.2 Hydrogel substrate

As a starting point, we used the same hydrogel matrix formulation as for the mini-guts[100]. More specifically, it was composed of 25% Matrigel and 75% type I bovine dermis collagen. As shown in Figure 3.2c, however, in the long run, this gel resulted in substantial invasion by the HBE cells (or detachment from the matrix, data not shown). I therefore screened for different gel formulations with the aim of improving long-term cell culture, differentiation and ALI capability. Given the relative complexity of AirGel fabrication, I used a simplified setup composed of a gel layer atop a porous

Transwell insert (Figure 3.4a). I screened for synthetic polyethylene glycol (PEG)-based gels, gels based on extracellular matrix (ECM) components (such as the Matrigel-collagen mix used by the Lutolf lab), and a combination of both. It turned out that, the higher the ECM components ratio, the better the cell coverage and growth (data not shown). Consequently, I focused on optimizing ECM-based gels to match the requirements for AirGels.

One important parameter to tweak was the collagen source and concentration. Type I collagen is most commonly extracted from either the bovine dermis or the rat tail; extraction strategies vary for these two sources, which influences the structure and properties of the resulting gels[102]. I used confocal reflection microscopy to visualize the fiber network of collagen-Matrigel mixtures (in AirGels), for which I varied the collagen source and concentration. More specifically, I used either: bovine dermis collagen 4 mg/ml, rat tail collagen 3 mg/ml, rat tail collagen 8 mg/ml. Rat tail collagen appeared to form a more homogeneous hydrogel than bovine dermis collagen, which displayed thick fibers with large pores (Figure 3.4b). While in the long run, those large fibers led to inhomogeneous coverage by HBE cells (data not shown), they also provided greater mechanical strength to the gel. Consequently, at similar concentrations, the rat tail gel was invaded and remodeled more easily than the bovine dermis gel (Figure 3.4c). Fortunately, high-density rat tail collagen is commercially available (resulting in the 8 mg/ml gel shown in Figure 3.4c); thus, this was selected as the best compromise.

To further improve long-term stability of AirGels, the broad-spectrum protease inhibitor GM6001 was added to the culture medium to prevent the cells from degrading the ECM[103]. Finally, two extra steps were necessary to enable maintenance of the ALI over several days: first, regular Matrigel was replaced with high concentration Matrigel (~10 mg/ml vs ~22 mg/ml, respectively). Additionally, the collagen network was further crosslinked based on a published protocol[104] (for detailed methods, see appendix 3.4).
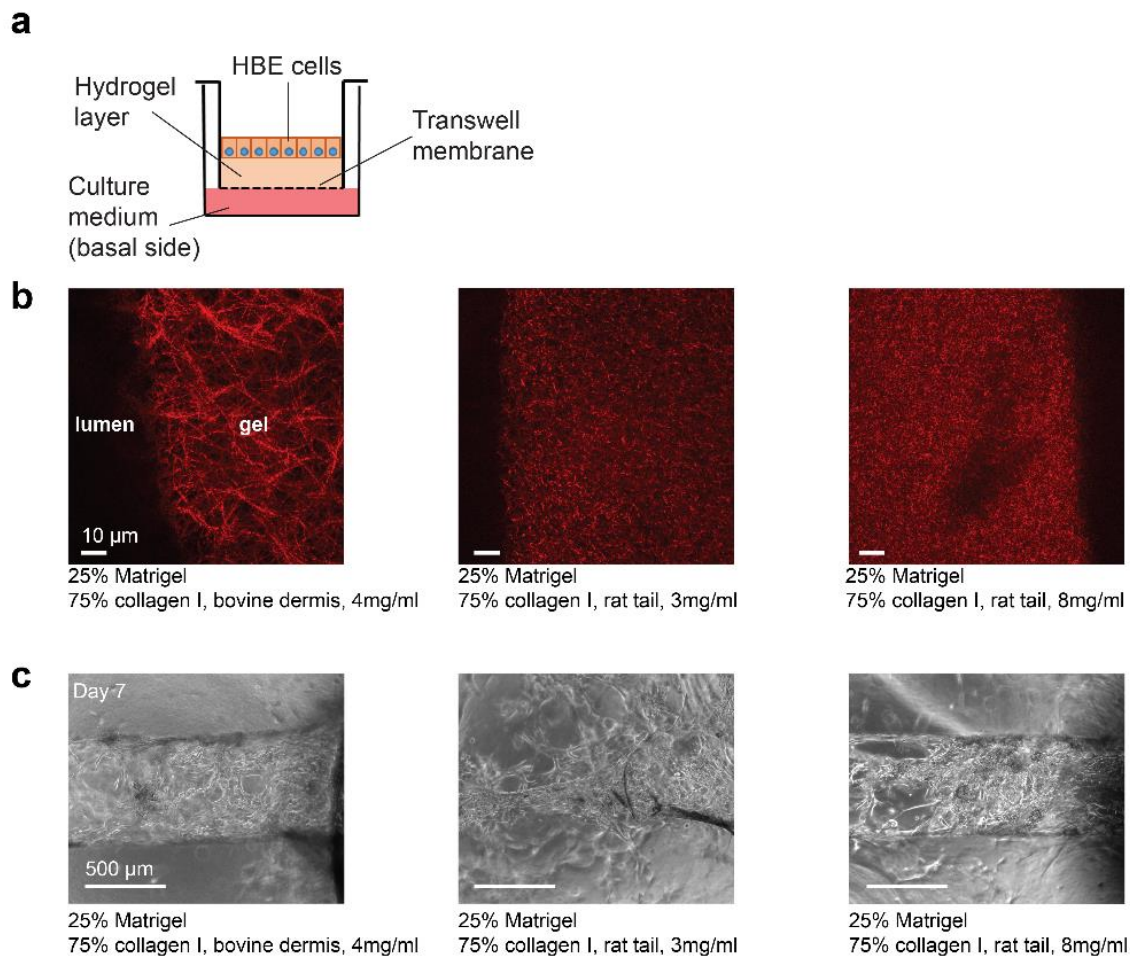
Figure 3.4: Optimization of the hydrogel substrate.

(a) Setup used to rapidly screen hydrogel formulations. (b) Confocal reflection microscopy images of different hydrogel formulations; while they all contained 25% Matrigel and 75% type I collagen, the source and concentration of the collagen varied. From left to right: bovine dermis 4 mg/ml, rat tail 3 mg/ml, rat tail 8 mg/ml. (c) HBE cells grown for 7 days in AirGels made from the gels shown in panel b.

3.2.3 Cell culture conditions

After optimizing the chip fabrication protocol and the formulation of the hydrogel substrate, the last step was to identify culture conditions resulting in stable, differentiated epithelia. As suggested in a publication by Barkal and colleagues[105], the loading density is important for proper coverage of the 3D lumen (~20'000 cells/µl). The culture medium composition did not have to be optimized (aside from the addition of GM6001 as mentioned above), because commercially available media, like PneumaCult™ Airway Organoid Differentiation Medium from Stemcell Technologies, are known to sustain differentiation of HBE cells. One important point that was already discussed in section 3.2.1, though, was to ensure sufficient supply of medium on the basal side of the cells.

3.3 AirGel characterization

After extensive optimization, I reached a reliable fabrication protocol fulfilling the requirements described in section 3.1.2. Thus, the next step was to validate that HBE cells grown in AirGels faithfully recapitulated the characteristic features of human airway epithelia. Note that the detailed methods for this section are also available in appendix 3.4.

To verify that HBE cells uniformly covered the surface of the cylindrical cavity, even after several weeks of culture, I visualized a fully-differentiated AirGel, in which actin had been fluorescently labeled, using selective plane illumination microscope (SPIM). As shown in Figure 3.5a, HBE cells formed a tubular structure in AirGel chips. I then assessed epithelial permeability by loading fluorescent dextran in the lumen of an 11-days old AirGel. After 30 min, the dye was still exclusively contained in the lumen, suggesting the presence of a tight epithelial barrier (Figure 3.5b). Two different methods were followed to verify that epithelia in AirGels comprised the relevant human airway cell types: immunostaining (Figure 3.5c) and single-cell RNA sequencing (scRNA-seq) (Figure 3.5d). Both methods highlighted abundant populations of ciliated cells (41% in scRNA-seq) and secretory cells (34% in scRNA-seq). The proportion of basal cells (8%) was lower than the values usually reported in the literature (ranging from 20% to more than 50% depending on the studies and the region of the airway[106–110]). However, a transitional cell population termed suprabasal cells is sometimes included in the basal cell cluster. KRT4 and KRT13 are among the main markers expressed by suprabasal cells[111]. In AirGels, these markers were highly expressed in the subpopulation of cells that we identified as "immature secretory" (Figure 3.5e and f). Adding this subpopulation to the basal cells gives a proportion of 18%, which is now in accordance with the lower end of values reported in the literature. More specifically, based on a recent publication by Deprez, Zaragosi et al., AirGels appear to recapitulate the histological signature of the distal human airway[108].
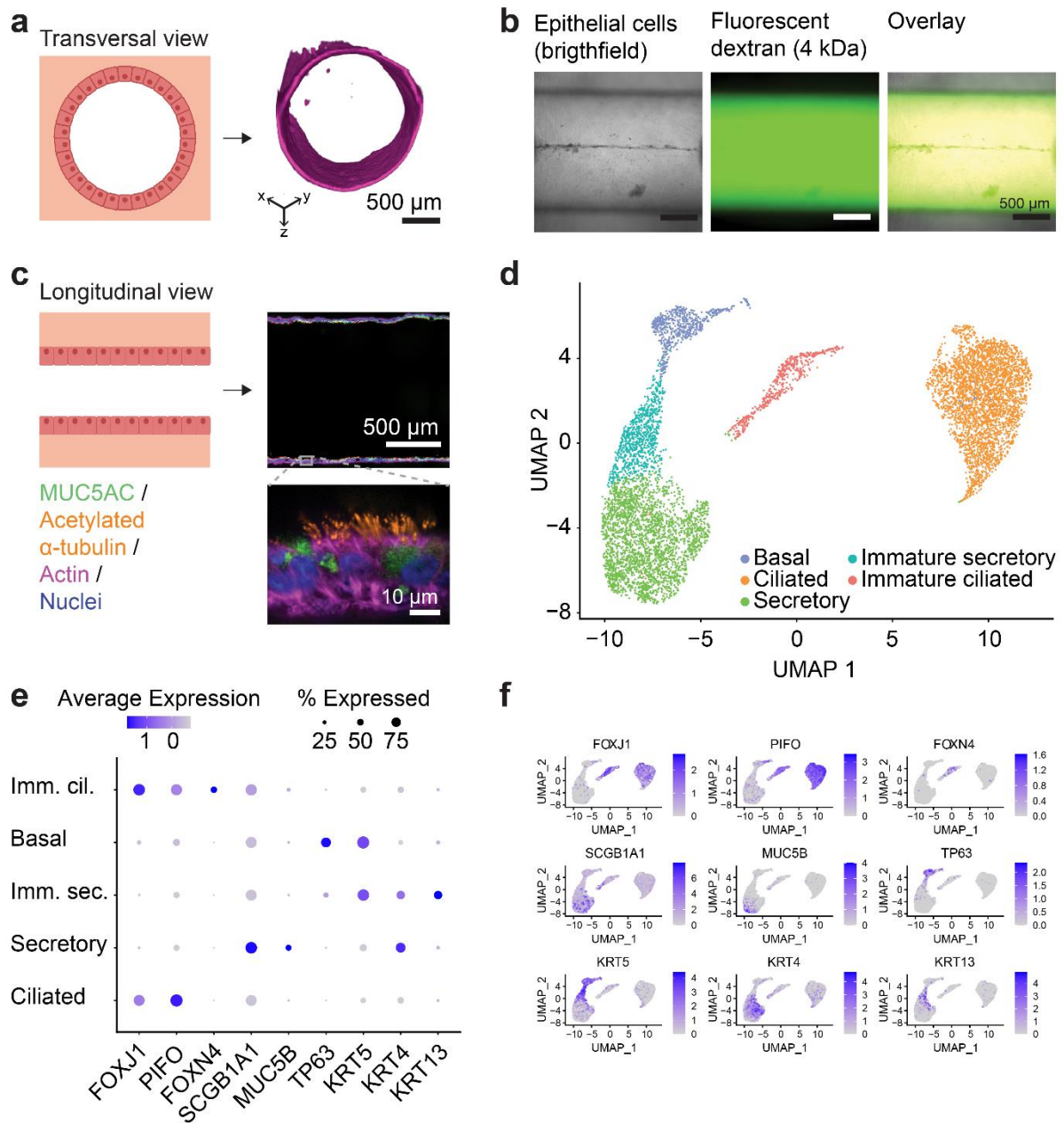
Figure 3.5: Geometry, barrier function and cell types in AirGels.

(a) Transversal view of a fully-differentiated AirGel lumen, in which actin was stained with fluorescently-labeled phalloidin. (b) Epithelial permeability assay, in which fluorescent dextran was loaded into the lumen of an 11-days old AirGel and imaged after 30 min. (c) Immunofluorescence staining of a fully-differentiated AirGel, labeled for the gel-forming mucin MUC5AC (green) and cilia, visualized by staining acetylated α-tubulin (orange) along with the actin dye phalloidin (pink) and nuclear dye DAPI (blue). (d) Uniform Manifold Approximation and Projection (UMAP) embedding of cells pooled from three differentiated AirGels (35-days old), subjected to scRNA-seq profiling. (e) Expression of marker genes of lung epithelial cell types shown for each cluster defined from the scRNA-seq reads of AirGels. Imm. cil. and imm. sec. stand for immature ciliated and immature secretory, respectively. (f) Subset-specific expression of canonical marker genes on UMAP embedding. FOXJ1 and PIFO are typically expressed in ciliated cells. The immature ciliated cell cluster, also known as deuterosomal cells, is marked by high levels of FOXJ1 and expression of FOXN4. Basal cells typically express TP63 and KRT5. The secretory cluster shows expression of SCGB1A1 and a fraction of more mature secretory cells expressing MUC5B[112]. Furthermore, we observe a transitional state between basal and secretory, the immature secretory cluster, which shows partial mutual expression of KRT4 and KRT13 as previously described[109].

Given that AirGels contain secretory cells, the next characterization step consisted in checking for the presence of an extracellular mucus layer. I therefore visualized fully-differentiated AirGels labeled with either antibodies against gel-forming mucins or a FITC-tagged lectin called jacalin, in fixed or live configurations, respectively (Figure 3.6a). In both cases, fiber-like structures lined the lumen, indicating that AirGels secrete mucus. I then measured ciliary beating frequency (CBF) and MCC by loading fluorescent beads in the lumen of AirGels. While MCC measurement was performed in immersed conditions, right upon loading, for CBF beads were left to settle for 1h, before all fluid was aspirated from the lumen. This way, the only beads that remained in the lumen were the ones that bound to the cilia. By recording high-frame rate videos of individual beads and subsequently performing Fourier analysis, I estimated the CBF to be around 15 Hz, which is consistent with previous literature[37,87,113,114] (Figure 3.6b). Tracking the trajectory of single beads in immersed lumens revealed that only differentiated AirGels were able to generate directional flow with physiologically relevant velocities[37,80,85] (Figure 3.6c).

Taken together, these results demonstrate that AirGels mimic key features of the human respiratory tract epithelium. In addition, the fabrication process optimized for microscopy allows for high spatiotemporal resolution imaging. In the next chapter, I will therefore use AirGels as a model to investigate how *P. aeruginosa* forms biofilms at the human airway mucosa.
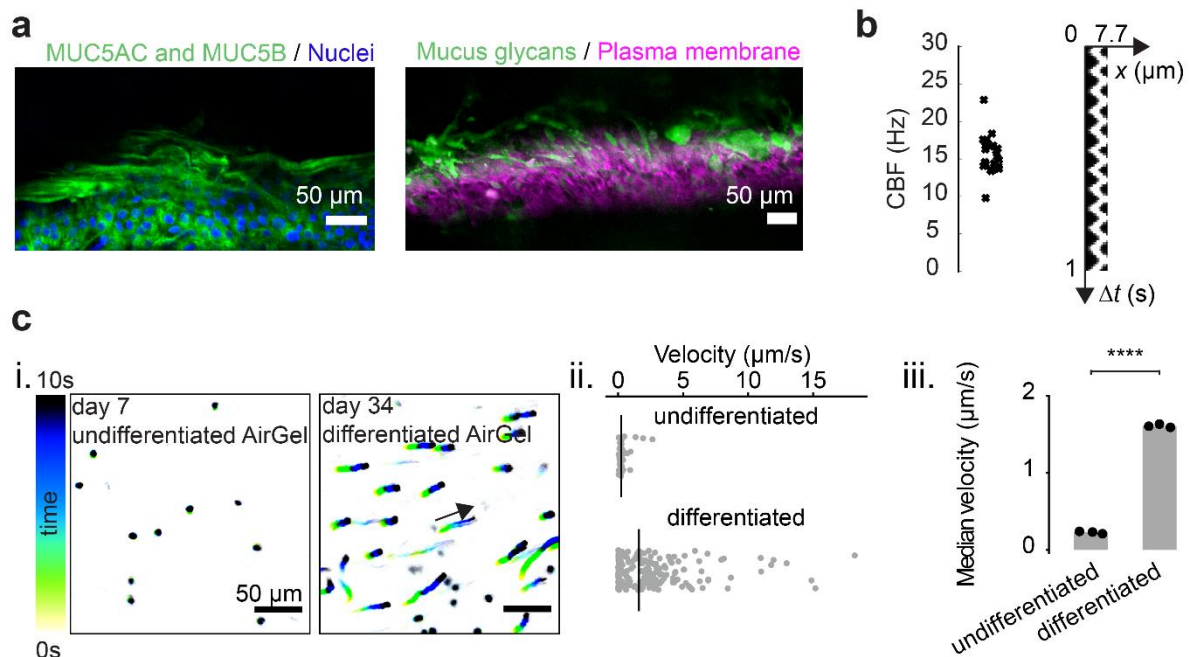
Figure 3.6: Mucociliary function of AirGels.

(a) Staining of the secreted mucus layer (green) in methacarn-fixed and live configurations. Antibodies against airway gel-forming mucins were used for the fixed sample, while fluorescently-labeled jacalin served to label the live sample. (b) CBF measurements from 5 different AirGels (5 locations imaged per AirGel), along with a kymograph showing the oscillations of a single cilia-bound bead over 1s. (c) i. Trajectories of fluorescent beads in undifferentiated and differentiated AirGels. ii. Velocity of each tracked bead in undifferentiated and differentiated AirGels. Black lines indicate the median velocity. iii. Median velocity across all tracked beads for N = 3 AirGels. Each data point corresponds to the median in each experiment; the gray bar shows the median of triplicates. Statistics: independent samples Student t-test with Bonferroni correction ($p < 10^{-7}$).

3.4 Appendix: detailed methods for AirGel fabrication and characterization

These methods have been adapted from the preprint posted on bioRxiv in May 2022 (and updated in December 2022), as:

Tamara Rossy, Tania Distler, Joern Pezoldt, Jaemin Kim, Lorenzo Talà, Nikolaos Bouklas, Bart Deplancke, Alexandre Persat*, *Pseudomonas aeruginosa contracts mucus to rapidly form biofilms in tissue-engineered human airways*.

DOI: https://doi.org/10.1101/2022.05.26.493615

Affiliations:

Tamara Rossy, Tania Distler, Lorenzo Talà & Alexandre Persat: Institute of Bioengineering and Global Health Institute, School of Life Sciences, École Polytechnique Fédérale de Lausanne, Lausanne, 1015, Switzerland.

Joern Pezoldt and Bart Deplancke: Institute of Bioengineering, School of Life Sciences, École Polytechnique Fédérale de Lausanne, Lausanne, 1015, Switzerland.

Jaemin Kim and Nikolaos Bouklas: Sibley School of Mechanical and Aerospace Engineering, Cornell University, Ithaca, NY, USA

3.4.1 AirGel chip fabrication

3.4.1.1 3D printed mold

The mold for the PDMS chips was designed in Autodesk Inventor Professional 2021. This mold was then 3D printed by Multi Jet Modeling on a Connex 500 printer (Objet) using VeroClear resin at the Additive Manufacturing Workshop (AFA) at EPFL. In order to remove uncured resin that could interfere with subsequent PDMS polymerization, we treated our mold by soaking it in deionized water for 2h; then, we incubated it for 18h in an oven set to 85°C; finally, we washed it with deionized water and dishwashing soap before letting it dry.

3.4.1.2 PDMS chip

PDMS (Sylgard 184, Dow Corning) was casted on the mold and cured at 60 °C for about 1h30. We then used a scalpel to cut out each chip individually and carefully remove it from the mold. In parallel, we prepared PDMS rods to pattern the lumens according to a published protocol [101]. In short, we filled gauge 14 needles (Sterican 2.1 x 80 mm, B. Braun) with PDMS and cured it as described above. We then used pliers to break the needles and extract the PDMS rods; their diameter was approximately 1.6 mm (i.e. inner diameter of the needle). We used a scalpel to cut them into 8mm-long pieces. Then, PDMS chips and rods were briefly immersed in isopropanol, left to dry, and cleaned using tape. Afterwards, the rods were inserted into the chips using tweezers; the assembled devices were subsequently autoclaved. They were then plasma bonded to either glass-bottom dishes or glass-bottom 6-well plates (1.5 coverslip, glass diameter 20 mm, MatTek) in a ZEPTO plasma cleaner (Diener electronic). Note that the chips contained thin PDMS membranes at the bottom of their inlet reservoirs (obtained owing to a shallow cavity in the 3D printed mold), so that the rod was not in direct contact with the underlying coverslip. Finally, we exposed the chips to two cycles of UV sterilization in a biosafety cabinet.

3.4.1.3 Extracellular matrix

All the following steps were performed in a biosafety cabinet to maintain sterility. We treated the chips inner surfaces to promote adhesion of the gel following a published method[105]. This consisted in a 10 min exposure to 2% polyethyleneimine (Sigma-Aldrich) followed by a 30 min treatment with 0.4% glutaraldehyde (Electron Microscopy Sciences) for 30 min. The chips were then rinsed once with Milli-Q water (Merck Millipore). Afterwards, the ECM hydrogel was prepared on ice. We first neutralized high-density rat tail type I collagen (~10 mg/ml, Corning) to a final concentration of 8 mg/ml. To do this, we mixed 30 µl 10X PBS, 5.4 µl NaOH 1M, 29.6 µl Milli-Q water and 235 µl collagen with a positive displacement pipette (Gilson). The neutralized collagen was then mixed with high-concentration growth factor reduced Matrigel (~21 mg/ml, Corning) in a 75:25 ratio (100 µl Matrigel for 300 µl of neutralized collagen). The resulting gel was loaded into each chip from the basal access ports and placed in a humidified cell culture incubator (set to 37°C, 5% CO_2) during 20 min in order for polymerization to occur. Then, we pulled the rods out of the chips with tweezers, thereby shaping the lumen[101]. The final step consisted in chemically crosslinking the collagen to strengthen it. We followed a published protocol[104]: we first prepared a 0.6M solution of N-(3-dimethylaminopropyl)-N′-ethylcarbodiimide hydrochloride (EDC, Life Technologies) and a 0.15M solution of N-hydroxysuccinimide (NHS, Sigma-Aldrich). Then, we mixed those solutions in a 1:1 ratio and loaded 25 µl into each lumen. We left them at room temperature for 5 min before aspirating the crosslinking reagents. We then soaked the chips in Milli-Q water (apical and basal sides) overnight, at room temperature. Finally, we replaced Milli-Q water with PneumaCult-Ex Plus medium (Stemcell Technologies) at least one day before loading any cells in the chips, and stored the chips in a cell culture incubator.

3.4.2 Cell culture

3.4.2.1 Expansion in flasks

We obtained primary human bronchial epithelial cells from Lonza (CC-2540S or CC-2540 for healthy donors, 00196979 for the CF donor). They were cultured in T-25 flasks using PneumaCult™-Ex Plus medium (Stemcell Technologies) for no more than 3 passages. When they reached confluence, the

cells were detached from the flask using the Animal Component-Free Cell Dissociation Kit (Stemcell Technologies) and centrifuged before being resuspended in PneumaCult™-Ex Plus to a density of approximately 20'000 cells/µl.

3.4.2.2 Loading into AirGels

AirGels were emptied of all culture medium on the apical and basal sides. 10-12 µl of HBE cell suspension was loaded in the lumen of each AirGel. The chips were then placed in a cell culture incubator for 25 min, flipped upside down and incubated again for 25 min, and then finally for 15 min on each side in order to allow uniform adhesion of cells along the luminal surface. Afterwards, PneumaCult™-Ex Plus was added to the lumen and on the basal side of the chips.

3.4.2.3 Long-term culture in AirGels

HBE cells were expanded in AirGels with PneumaCult™-Ex Plus until confluence was reached (typically 1-3 days). After that, apical and basal expansion medium was replaced with PneumaCult™ Airway Organoid Differentiation Medium (Stemcell Technologies). In order to prevent gel degradation by the HBE cells, we supplemented the medium with 5 µM of protease inhibitor GM6001 (InSolution GM6001, Merck). One day after the first addition of differentiation medium, all fluid was aspirated from the lumen, thereby generating an ALI. This critical step was facilitated by the aforementioned collagen crosslinking and by the large lumen diameter, which lowered capillary forces drawing medium back in the channel. AirGels could be kept in these conditions for at least one month; medium was replaced on the basal side every second day. Before weekends, the lumen was also filled with PneumaCult™ Airway Organoid Differentiation Medium, but ALI was restored every Monday morning and maintained for the whole week.

3.4.2.4 Cell culture on Transwell membranes

For isolated mucus experiment and twitching motility imaging, we grew NHBE cells on 0.4µm-pore polyester Transwell membranes (Corning) instead of AirGels. The expansion phase and cell dissociation process were as described above. NHBE cells were loaded on Transwells at a density of $\sim 5 \cdot 10^4$ cells per well. When they reached confluence, they were transitioned to ALI culture

conditions, i.e. with PneumaCult™-ALI medium (Stemcell Technologies) on the basal side and air on the apical side.

3.4.3 Live staining

To label mucus in live AirGels, we used jacalin conjugated to fluorescein (Vector Laboratories). We prepared a 50 µg/ml solution and loaded it in the lumen. We stored the chips for 30 min in a cell culture incubator before aspirating all fluid from the lumen. In addition, in order to assess epithelial integrity, we loaded a 4 kDa fluorescent dextran solution in the lumen of an 11-day-old healthy chip and incubated it for 30 min. We then verified that all signal was localized in the lumen of the chip.

3.4.4 Immunofluorescence

All steps were performed at room temperature. First, differentiated cells in AirGels were fixed with either 4% paraformaldehyde (PFA, Electron Microscopy Sciences) or methacarn, when we wanted to better preserve extracellular mucus. Methacarn was made fresh before every use as follows: 1 part glacial acetic acid (Sigma-Aldrich), 3 parts chloroform (PanReac AppliChem), 6 parts anhydrous methanol (Sigma-Aldrich). Regardless of the chemical used, the fixation step lasted for 15 min. PFA-fixed cells were then permeabilized with a 0.2% Triton X-100 solution (VWR Life Science) for 20 min. Then, we exposed all cells (i.e. PFA- and methacarn-fixed) to a blocking solution consisting of 1% bovine serum albumin (Sigma-Aldrich) during 45 min. Afterwards, we added solutions of primary antibodies to each AirGel and incubated them for 1h. In case of PFA-fixed cells, we used rabbit anti-MUC5AC (1:100, Abcam) and mouse anti-acetylated alpha tubulin (1:250, Sigma-Aldrich); for methacarn-fixed cells, we used the same anti-MUC5AC, together with rabbit anti-MUC5B (1:100, Sigma-Aldrich). This was followed by the labeling with secondary antibodies, during 1h in the dark. More specifically, we used goat anti-rabbit IgG H&L Alexa Fluor 488 (1:200, Abcam) and goat anti-mouse IgG H&L Alexa Fluor 594 (1:200, ThermoFisher). Finally, nuclei were counterstained for 10 min with DAPI (1:1000, Sigma-Aldrich); in addition, in PFA-fixed cells, actin was stained with Phalloidin Atto 655 (1:40, Sigma-Aldrich) for 10 min.

3.4.5 Sample preparation before lightsheet imaging

To perform lightsheet microscopy on AirGels, we needed to extract the ECM gel and cells from the PDMS chip. After fixation and staining, we filled in the lumen with a 1% low-melt agarose solution in order to ensure structural integrity of the airway. We let it solidify; using tweezers, we could then carefully detach the PDMS from the glass; indeed, since the surface of the 3D printed mold was not perfectly smooth, plasma bonding was not irreversible, which we could leverage for ECM extraction. We then used a scalpel and a spatula to release the piece of ECM from the PDMS chip and later embedded it in 1% low-melt agarose. While the agarose was still liquid, we aspirated the whole gel into a 1 ml syringe (Omnifix-F, B. Braun), whose tip had previously been cut out. After the agarose solidified, we could then use the plunger to freely push the fixed AirGel in and out of the syringe, in order to image it with SPIM.

3.4.6 Microscopy

To image AirGels at low magnification (Figure 3.5b), we used a Nikon TiE epifluorescence microscope equipped with a Hamamatsu ORCA Flash 4 camera and either a 10x objective with N.A. of 0.25 or a 4x objective with N.A. of 0.1. For full channel cross-sectional imaging (Figure 3.5a), we used a Zeiss Lightsheet Z1 dual sided SPIM. It was equipped with PCO Edge 5.5 cameras and a 5x magnification objective with N.A. of 0.16. All the other visualizations were acquired with a Nikon Eclipse Ti2-E inverted microscope coupled with a Yokogawa CSU W2 confocal spinning disk unit and equipped with a Prime 95B sCMOS camera (Photometrics). We either used a 20x water immersion objective with N.A. of 0.95, or a 40x water immersion objective with N.A. of 1.15. We used Imaris (Bitplane) for three-dimensional rendering of lightsheet z-stack pictures and Fiji for the display of all the other images[115].

3.4.7 Single-cell RNA-seq

3.4.7.1 Sample processing and sequencing

Three AirGels differentiated for 35 days were pooled to perform single cell RNA sequencing. The AirGels were washed three times with PBS from the apical and basal sides before carefully detaching

the PDMS chip from the dish. Epithelia were removed together with their ECM from the chip using forceps and placed in dissociation buffer (300 µl Protease from Bacillus Licheniformis (100 mg/ml, Sigma), 3 µl DNase I (10 mg/ml, Roche), 30 µl EDTA (0.5 M, Sigma), 30 µl EGTA (0.5 M, BioWorld), 237 µl sterile PBS and 900 µl Accumax (Brunschwig)). Incubation was performed for 45 min at 37 °C except for centrifugation and pipetting steps which were performed at room temperature. Initially, the piece of gel and attached cells was disrupted by pipetting up and down 50 times every 5 min with a 200 µl filtered pipette tip. After the first 20 min of incubation, the cells were mostly detached from the gel and the cell suspension was centrifuged for 5 min at 400x g, after which the supernatant was removed. The residual volume (approximately 20 µl) was pipetted up and down 50 times every 5 min to disrupt cellular aggregates, this time with a 10 µl filtered pipette tip. Finally, the cell suspension of all three chips was combined and topped up to 1 ml with pre-cooled 10 % BSA (Sigma-Aldrich) in PBS. From this point, all steps were performed on ice or at 4 °C. The cells were centrifuged for 10 min at 400x g. The supernatant was carefully removed and the cells were resuspended in 0.04 % molecular grade BSA in PBS and filtered through a 40 µm Flowmi cell strainer (Bel-Art). The cell suspension was centrifuged once more at 400x g for 10 min. The supernatant was removed and the cells were resuspended in 50 µl 0.04% molecular grade BSA in PBS. The cell count was determined and the cells were immediately taken to the sequencing facility at EPFL (GECF).

HBE cells were then washed once in PBS 10% BSA and then once in PBS 0.04% BSA. After filtration through a 40 µm Flowmi strainer, cells were resuspended in PBS 0.04% BSA, checked for absence of significant doublets or aggregates, and loaded into a Chromium Single Cell Controller (10X Genomics) in a chip together with beads, master mix reagents (containing RT enzyme and poly-dt RT primers) and oil to generate single-cell-containing droplets. Single-cell Gene Expression libraries were then prepared using Chromium Single Cell 3' Library & Gel Bead Kit v3.1 (PN-1000268) following the manufacturer's instruction (protocol CG000315 Rev C). Quality control was performed with a TapeStation 4200 (Agilent) and QuBit dsDNA high sensitivity assay (Thermo) following manufacturer instructions. With this procedure, the cDNAs from distinct droplets harbor a distinct and unique 10X "cell barcode".

Sequencing libraries were processed using an Illumina HiSeq 4000 paired-end Flow Cell and sequenced using read lengths of 28 nt for read1 and 91 nt for read2, at a depth of ca 60k reads/cell.

3.4.7.2 scRNA-seq analysis

The Cell Ranger Single Cell Software Suite v6.1.1 was used to perform sample demultiplexing, barcode processing, and 3' gene counting using 10X Genomics custom annotation of human genome assembly GRCh38[116]. Count matrices were further processed with Seurat (version 4.1.0)[117]. All cells with less than 1,000 detected genes per cell were filtered out. Moreover, cells with more than 25% reads mapping to mitochondrial genes were removed yielding 8,651 cells passing QC. After filtering, data were default normalized and the 2,000 most variable genes identified. The expression levels of these genes were scaled before performing PCA. The following covariates were regressed out: number of UMIs and percent of mitochondrial reads UMAP dimensionality reduction was performed using the first 25 dimensions of the PCA and resolution set to 0.175. Cell subsets were identified based on transcriptional signatures previously identified by Plasschaert, Žilionis *et al* [109]. One subset was comprised of cells with a shared signature between "Ciliated" and "Secretory" cells, with a total of 640 cells, indicative of doublets and were thus removed. The remainder cells, numbering 8,011 were re-embedded as described above (resolution = 0.15). GO analysis was performed for differentially upregulated genes per cluster using *TopGO*[118].

3.4.8 Quantification of cilia beating frequency

We filled the lumens of AirGels with a 1:500 solution of yellow-green carboxylated fluorescent beads with a 2 μm diameter (FluoSpheres, Life Technologies). We incubated them for 1h; in this time interval, despite the flow generated by ciliary beating, some beads were able to settle down and attach to cilia. We then removed all fluid from the lumen and brought the chips to the spinning disk confocal microscope. We then selected small regions of interest (50 x 50 pixels, i.e. 27.5 μm x 27.5 μm) around individual beads and recorded videos at 100 frames per second. Using Matlab R2016b (Mathworks), we computed the mean intensity of each frame over time. We computed the fast Fourier transform of each mean intensity signal, which we then used to obtain single-sided power

spectra. We only kept frequencies between 1 and 30 Hz, thereby getting rid of artifacts. We finally looked for the frequency with maximal amplitude in the power spectrum, which corresponded to the cilia beating frequency.

3.4.9 Quantification of mucociliary clearance

Like for CBF quantification, we loaded a 1:500 solution of 2 µm FluoSpheres in the lumen of AirGels. We immediately visualized them with the spinning disk confocal microscope. We recorded 10 s videos at a rate of 10 frames per second. Then, tracked the trajectory of individual beads with the Fiji plugin TrackMate[119], using the built-in simple LAP tracker. We wrote a script in a Jupyter Notebook to compute the velocity (track displacement over track duration) of each particle[120].

Chapter 4. *Pseudomonas aeruginosa* contracts mucus to form biofilms in the airway

In the previous chapter, I described the development and validation of AirGel, a novel tissue-engineered airway model. I will now focus on the insight this model provided into biofilm formation at the respiratory mucosa.

4.1 Additional background

4.1.1 Respiratory infections and pathogen adaptation to diseased airways

As was made evident by the COVID-19 pandemic, respiratory infections are a global health concern. In fact, in 2019, even before the pandemic started, lower respiratory tract infections were the fourth cause of deaths worldwide, and the leading cause of deaths due to communicable diseases[121]. As discussed in earlier chapters, lower respiratory infections that involve bacterial biofilms are of particular concern, since antibiotic treatments often fail to eradicate them. Of note, while biofilms have traditionally been associated with chronic infections, recent evidence suggests they may also form in acute conditions[79]. However, since most studies of airway biofilms until then had focused on chronic infections, these will be the topic of the next paragraphs.

Chronic respiratory infections are particularly prevalent in individuals with underlying lung disease, like CF. In this illness, because of a dysfunctional ion channel called CFTR, ion transport across the epithelium is defective, which results in a sticky, dehydrated mucus layer[37,78,122]. By compressing the underlying cilia[123], this abnormal mucus impairs MCC, thus facilitating bacterial colonization[36]. Consequently, CF patients suffer from intermittent acute infection episodes for several years. These are followed by the onset of chronic infections, most commonly by the opportunistic pathogen *P. aeruginosa*[124]. This bacterium is frequently found in biofilms in the sputum of CF patients[42,79].

However, little is known about how *P. aeruginosa* transitions from an easily eradicated, acute infectious agent to an airway-adapted, biofilm-forming pathogen. The harshness of the CF airway environment, along with regional differences and isolation, are thought to drive the evolution and diversification of resident *P. aeruginosa*[124,125]. Indeed, despite providing a warm, nutrient-rich niche, the CF airway may also apply selective pressure on pathogens in many ways. For example, the increased mucus viscosity imposes osmotic stress on the numerous microbes colonizing the CF airway[124]. Moreover, in addition to fostering competition, the presence of these various strains triggers the recruitment of inflammatory defense mediators. This leads to increased oxidative and nitrosative stress, and decreased oxygen concentration in the mucus[124]. Finally, recurrent treatments with antibiotics also apply considerable pressure on the colonizing bacteria. All these stressors likely select for strains that are adapted to survive in harsh conditions. *P. aeruginosa* isolated from CF patients often exhibit hypermutability[124]. These mutants, despite their diversity, frequently share some of the following features: antibiotic tolerance or resistance; downregulation of motility, central metabolism, and virulence; upregulation of membrane permeability and efflux; mucoidy; rugose morphology[35,124,126]. While correlations between the environmental pressures and adaptations of *P. aeruginosa* can be hypothesized, a mechanistic understanding of host-pathogen interplays *in vivo* is still missing, in particular from a biomechanical standpoint. To tackle this issue, it is important to investigate how *P. aeruginosa* interacts with airway mucus at high spatiotemporal resolution. In the next section, I will summarize current knowledge about the influences of mucus and mucin gels on *P. aeruginosa*.

4.1.2 Interactions between *P. aeruginosa* and airway mucus

As mentioned earlier, mucus is the first barrier encountered by pathogens infecting the human airway. Whether and how interactions between *P. aeruginosa* and mucus impact biofilm formation *in vivo* is still unclear. Despite the lack of *in vitro* airway models for dynamic investigations, several research groups have found ways to explore these questions in simplified settings.

For instance, *P. aeruginosa* has been shown to grow in CF sputum[127]. Studies growing *P. aeruginosa* either on mucin-coated glass or in mucus extracted from Transwell cultures found a decreased

efficacy of antimicrobial treatments, consistent with clinical data from chronically infected patients[128,129]. Beyond these biochemical processes, physical interactions between mucus and *P. aeruginosa* have also been demonstrated. For example, *P. aeruginosa* selectively binds to mucin via the flagellar cap protein FliD[130]. In the study using mucin-coated glass, this binding capability was also found to decrease surface motility[128]. Similarly, a decrease in motility was observed in concentrated mucus isolated from Transwells[129]. In both cases, the reduced motility led to an increased aggregation of *P. aeruginosa*. A depletion mechanism triggered by polymers in solution, among which commercially-available mucins, also promoted aggregation of this pathogen[131]. However, studies using native mucins or mucin glycans instead showed that they prevent the formation of bacterial aggregates by promoting motility, as well as dispersing existing biofilms[132–134].

All these results highlight the sensitivity of mucus to experimental conditions. For example, commercial mucins are known to differ from native mucins, because their purification process prevents subsequent gel formation[135]. Also, mucus isolated from Transwells is not made of pure mucins, but may contain other polymers like DNA. How all these parameters influence biofilm formation in human airway infections is still unknown. This strong dependence of experimental results on the methodology supports our rationale of studying mucus-pathogen interactions in a system that closely mimics the *in vivo* conditions.

As a result, I leveraged our AirGel human airway model in order to probe the dynamics of *P. aeruginosa* biofilm formation in a physiologically relevant context.

4.2 Modeling *P. aeruginosa* infections in AirGels

These results and discussion have been adapted from the preprint posted on bioRxiv in May 2022 (and updated in December 2022), as:

Tamara Rossy, Tania Distler, Joern Pezoldt, Jaemin Kim, Lorenzo Talà, Nikolaos Bouklas, Bart Deplancke, Alexandre Persat*, *Pseudomonas aeruginosa contracts mucus to rapidly form biofilms in tissue-engineered human airways.*

DOI: https://doi.org/10.1101/2022.05.26.493615

Affiliations:

Tamara Rossy, Tania Distler, Lorenzo Talà & Alexandre Persat: Institute of Bioengineering and Global Health Institute, School of Life Sciences, École Polytechnique Fédérale de Lausanne, Lausanne, 1015, Switzerland.

Joern Pezoldt and Bart Deplancke: Institute of Bioengineering, School of Life Sciences, École Polytechnique Fédérale de Lausanne, Lausanne, 1015, Switzerland.

Jaemin Kim and Nikolaos Bouklas: Sibley School of Mechanical and Aerospace Engineering, Cornell University, Ithaca, NY, USA

4.2.1 *P. aeruginosa* rapidly forms mucus-associated biofilms in AirGels

To visualize biofilm formation in a realistic airway mucosal context, we inoculated P. aeruginosa constitutively expressing the fluorescent protein mScarlet in the lumen of AirGels maintained at the ALI. The mucus and plasma membranes of the host epithelium had also been fluorescently labeled beforehand to allow for simultaneous visualization of the host and the pathogen. After 13h of incubation, epithelial integrity appeared to be preserved, as made evident by the contiguous host cell layer, the localization of bacteria in the luminal compartment (Figure 4.1) and the numerous ciliated cells that were still beating (data not shown).
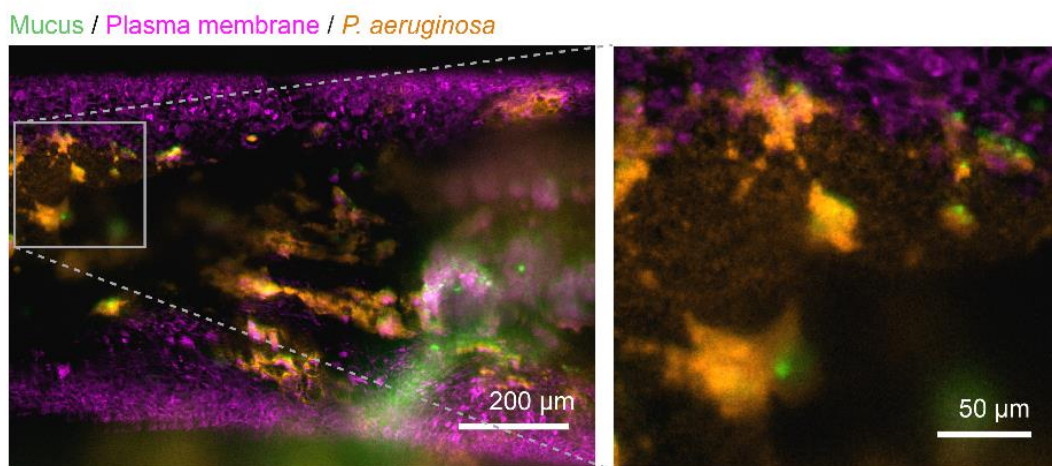
Figure 4.1: Proof-of-concept co-culture of AirGel and *P.aeruginosa*.

Confocal micrograph of a fully-differentiated AirGel 13h post-inoculation with *P. aeruginosa* constitutively expressing mScarlet (orange). The plasma membranes of the host epithelium were stained with CellMask Deep Red (pink) and mucus was labeled with FITC-jacalin (green).

Interestingly, *P. aeruginosa* formed interconnected bacterial clusters colocalized with mucus within the airway surface liquid (ASL) between epithelial cells and the air-liquid interface (Figure 4.1). In dynamic visualizations, bacteria remained attached to mucus despite mucus movements induced by beating cilia (data not shown). Since *P. aeruginosa* takes days to form biofilms in vitro, we were surprised to see these communities form only within a few hours in AirGels[136]. We therefore went on to investigate the mechanisms of rapid biofilm formation on mucus.
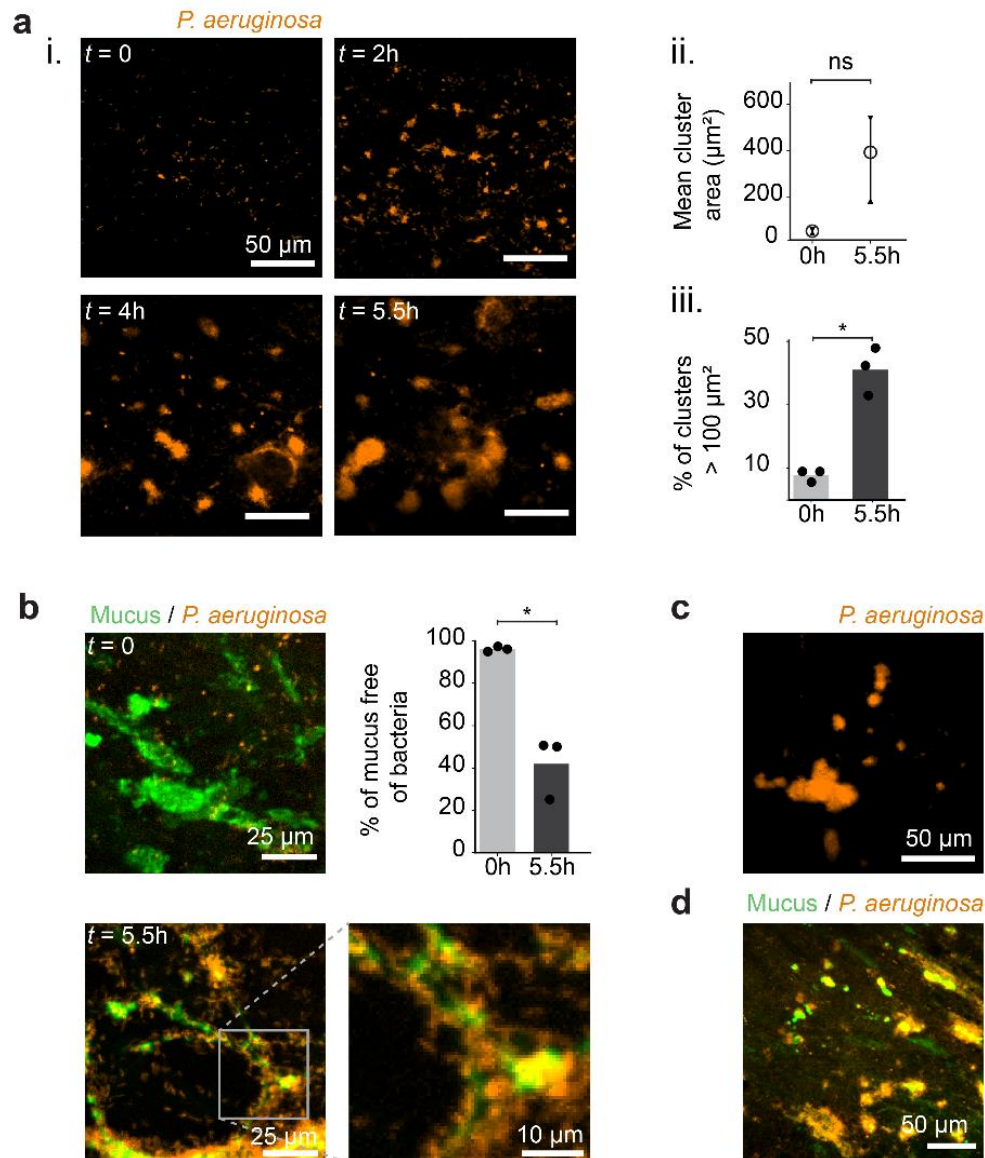
Figure 4.2: *P. aeruginosa* rapidly forms mucus-associated biofilms.

(a) i. Maximal intensity projection images of *P. aeruginosa* in a 35-day-old AirGel (healthy donor) shows biofilm formation within hours. ii. Mean biofilms cluster area for three AirGels. The bar indicates the range between the maximum and minimum of the three means. The circle represents the mean of the means. iii. Percentage of clusters that were larger than 100 µm² in each replicate (black dots). The bars represent the mean across replicates. Statistics: paired samples Student t-test with Bonferroni correction ($p = 0.051$ and $p = 0.01$). (b) *P. aeruginosa* rapidly colonizes mucus surfaces. Images show maximal intensity projection of confocal stacks of a 33-day-old infected AirGel at $t = 0$ and $t = 5.5$h post-inoculation. The graph quantifies the proportion of mucus not occupied by bacteria. Gray bars show the mean of triplicates. Statistics: paired samples Student t-test with Bonferroni correction ($p = 0.02$). (c) Infection of an AirGel in which mucus was not labeled. After 4h15, bacterial aggregates were already visible, indicating their formation is independent of jacalin staining. (d) Infection of 44-day-old CF AirGels with *P. aeruginosa*. After 4h, mucus-associated bacterial aggregates were visible, similar to what we observed in AirGels from healthy donors.

We imaged biofilm biogenesis in AirGels at the single cell level using confocal spinning disk microscopy. *P. aeruginosa* already formed aggregates a few hours after inoculation (Figure 4.2a). While the mucus surface was initially largely devoid of bacteria, half of it was covered by *P. aeruginosa* multicellular structures after 5.5h of infection (Figure 4.2b). Bacterial clusters with the same architecture also formed in the absence of jacalin staining, confirming these biofilms do not form through labeling artefacts (Figure 4.2c). Moreover, *P. aeruginosa* rapidly formed biofilms on mucus of diseased AirGels engineered from primary cells of CF donors (Figure 4.2d).

To confirm the pivotal role of mucus in biofilm formation, we infected a non-differentiated AirGel which does not produce mucus. In the absence of a protective mucus layer, epithelial cells were more vulnerable to *P. aeruginosa* infection (Figure 4.3a and b). Bacteria breached through the epithelial barrier and invaded the underlying ECM. *P. aeruginosa* did not form three-dimensional multicellular structures in the ASL. This further demonstrates the role of mucus hydrogel as a substrate for biofilm formation in differentiated AirGels, and at the same time highlights its protective function.

Our data suggests that *P. aeruginosa* forms biofilms in the airway by attaching to mucus at early stages of infection. To further explore the biophysical mechanisms of biofilm formation, we harvested mucus to perform *ex situ* visualizations. However, we could not observe the formation of *P. aeruginosa* biofilms on mucus extracted from AirGels (Figure 4.3c). We attribute this discrepancy to perturbations in mucus mechanical integrity when extracted from the epithelium, or to the absence of ALI. This difference highlights the importance of investigating microbe-mucus interactions in a native mucosal context such as the one established in AirGels.
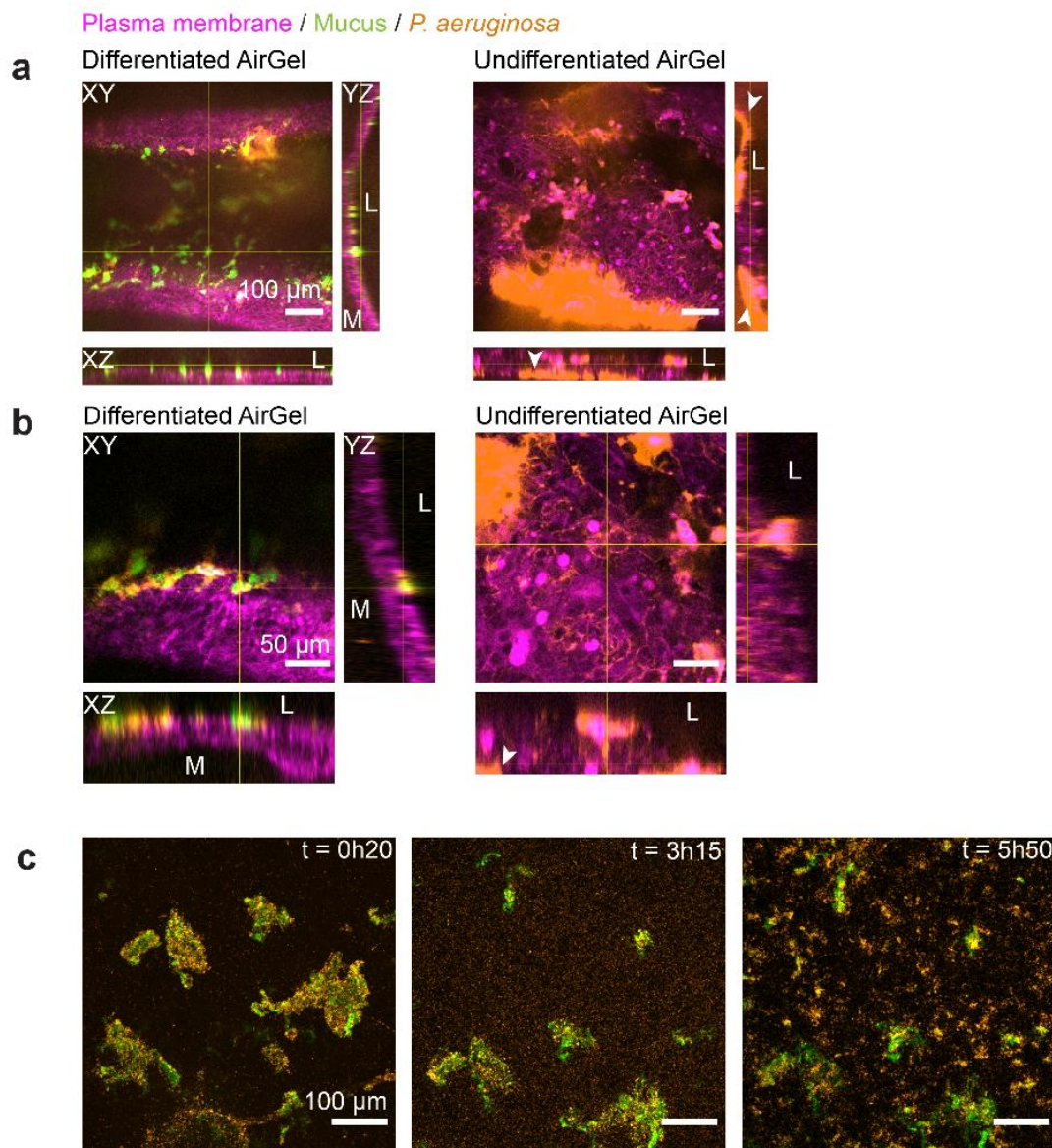
Figure 4.3: Importance of investigating *P. aeruginosa* biofilms on native mucus.

(a-b) *P. aeruginosa* does not form biofilms in AirGels lacking mucus, but damages its tissue more rapidly. Orthogonal views of infections with *P. aeruginosa* in a 37-day-old (differentiated) versus a 1-day old (undifferentiated) AirGel (both from healthy donors) stained with Jacalin at low (a) and high (b) magnification. The infection was imaged at *t* = 5.5h (differentiated) and *t* = 6h (undifferentiated) post-inoculation. L indicates the luminal side and M the extracellular matrix. Since the 1-day-old AirGel was not differentiated, it did not secrete mucus. In these conditions, we could not observe P. aeruginosa aggregates in the ASL on the luminal side. However, bacteria damaged the epithelium extensively in the absence of mucus, which resulted in invasion of the extracellular matrix (white arrowheads). (c) *P. aeruginosa* does not form biofilms on mucus extracted from Transwells, even after almost 6h of incubation.

To understand how biofilms form on native mucus, we therefore inspected the different steps of their formation in AirGels. To nucleate *in vitro* biofilms, *P. aeruginosa* cells navigate the surface of abiotic materials using twitching motility, which promotes the formation of aggregates[57]. Fast imaging of single cells shows that *P. aeruginosa* moves with twitching-like trajectories at the surface of mucus fibers (data not shown). As expected from axenic experiments, these single cells aggregate into small clusters within 2h of colonization. These small multicellular clusters subsequently moved along mucus fibers to eventually fuse (Figure 4.4a). This caused a cascade of cluster fusion events that sped up biofilm formation. We tracked aggregate fusion in kymographs highlighting the correlation between mucus and bacterial displacements (Figure 4.4b). The size of individual clusters remains approximately constant during motion and fusion, showing aggregate fusion predominates over bacterial growth. After 6h of aggregation and fusion, dense biofilms are formed.
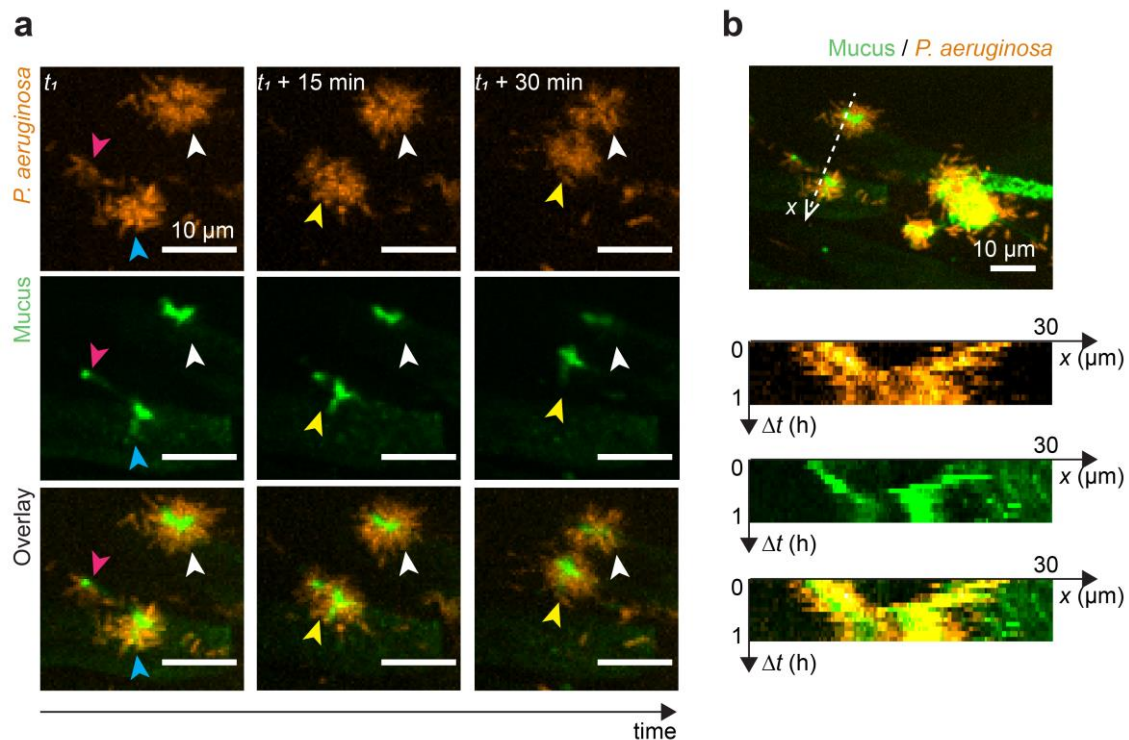
Figure 4.4: Dynamics of *P. aeruginosa* biofilm formation on mucus.

(a) Dynamic visualization of *P. aeruginosa* cluster fusion on mucus in a 33-day-old AirGel ($t_1 = 6.2$h). The blue and pink arrowheads show two aggregates that fuse within the first 15 min. The resulting cluster is indicated by a yellow arrowhead. This new cluster then moves closer to the one indicated by the white arrowhead. All images are maximal intensity projections from z-stacks. (b) Kymographs showing the displacement of two clusters along their axis of motion. The bacterial aggregate and underlying mucus traveled together at an approximate speed of 0.5 µm/min.

4.2.2 Formation of mucus-associated *P. aeruginosa* biofilms depends on T4P-mediated mucus rearrangements

We found that during biofilm formation, the mucus surface area tends to decrease compared to an uninfected control (Figure 4.5a and b). The distances between landmarks in a mucus patch decreased over time (Figure 4.5c), demonstrating that mucus contracts during biofilm formation. We therefore hypothesized that mucus contraction speeds up biofilm formation by bringing *P. aeruginosa* cells closer to each other. Ultimately, these cells would become contiguous to form small aggregates. By carrying on mucus contraction, these aggregates would then fuse to each other. To substantiate this physical contraction mechanism, we investigated how *P. aeruginosa* could restructure mucus during attachment and colonization. We envisioned two mechanisms for bacteria-induced mucus deformations: degradation or direct mechanical contraction. *P. aeruginosa* secretes mucinases capable of degrading gel-forming mucins[137]. Enzymatic mucus degradation could release polymers that generate entropic depletion forces promoting bacterial aggregation or that generate osmotic forces compressing mucus[131,138]. To test whether mucus degradation could drive contraction, we colonized AirGels with a mutant in the type II secretion system locus *xcp* that is necessary for mucin utilization[137,139]. The *Δxcp* mutant however formed biofilms similar to WT, ruling out the hypothesis of polymer-induced forces driving the formation of multicellular structures (Figure 4.6a).

Could *P. aeruginosa* remodel mucus by directly and actively applying force on the surface? *P. aeruginosa* can generate extracellular forces using flagella and T4P, motorized filaments that also play a role during *in vitro* biofilm biogenesis. In addition, T4P and flagella mediate single cell interactions with mucins[128,130,132,140,141]. To investigate their functions in the context of rapid biofilm formation on mucus, we infected AirGels with *P. aeruginosa* mutants lacking flagella (*ΔfliC*) and T4P (*ΔpilA*). The *ΔfliC* mutant formed biofilms that were indistinguishable from wild type (WT) (Figure 4.6a). By contrast, *ΔpilA* cells did not form multicellular structures, indicating T4P play a role in rapid biofilm formation. Since T4P may bind to glycans present on mucins[140,141], weaker cell attachment to mucus could cause a decrease in aggregation of *ΔpilA*. Yet, colocalization analysis shows that the *ΔpilA* mutant is still able to attach efficiently to mucus (Figure 4.6b). We therefore envisioned a

mechanism where T4P generate retractile forces that contract mucus from the surface, ultimately speeding up *P. aeruginosa* aggregation and cluster fusion.
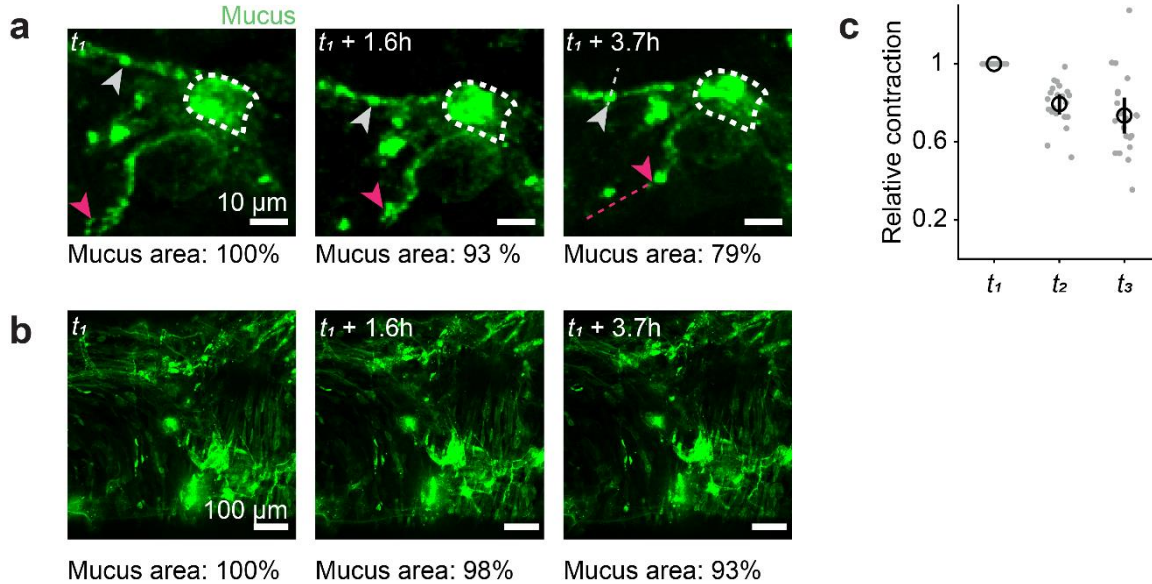
Figure 4.5: Mucus contraction over time.

(a) Time course visualization of a jacalin-stained mucus patch in a 35-day-old AirGel infected with WT *P. aeruginosa* (t_1 = 1.2h). Reference features and their trajectories are indicated by colored arrowheads and dashed lines. (b) Mucus does not contract in the absence of *P. aeruginosa*. Jacalin-stained mucus in a 35-days old healthy, uninfected AirGel (t_1 = 0.9h). The total area of mucus was estimated over time and found to only differ slightly over time, most likely due to photobleaching and drift in and out of focus. (c) Mucus contraction was quantified by tracking the distances over time between $N = 7$ reference features in the infected mucus patch. The distances were normalized to the initial time point. They decrease over time, indicating contraction of the mucus patch. t_1, t_2, t_3 refer to the timepoints shown in panel c. Black circle: mean. Black line: standard deviation.

To physically explore this scenario, we ran non-linear finite element simulations wherein mucus is treated as a hyperelastic material[142]. The mechanical action of *P. aeruginosa* T4P at the mucus surface is considered through the introduction of an active surface stress. The simulations recapitulated the experimental observations of mucus hydrogel contraction during *P. aeruginosa* colonization (Figure 4.6c). Simulations also predict that the steady-state mucus area decreases with the magnitude of the surface contractile modulus. This suggests that the more T4P retract, the more *P. aeruginosa* compresses mucus. To experimentally validate this model, we visualized AirGels colonization by a *ΔpilT* mutant which produces T4P that cannot retract, mimicking conditions of zero contractile modulus. *P. aeruginosa ΔpilT* could still associate with mucus and form a few small clusters, but clearly failed to form mucus-associated biofilms to the same extent as WT (Figure 4.6d and e), which was coherent with simulations. These results show that T4P retraction is necessary

for rapid biofilm formation, and is consistent with a scenario where retraction compresses the mucus substrate.

To further support the surface contraction model, we tested the prediction that deformations increase further with surface contractility. We imaged AirGel colonization by the hyperpiliated *P. aeruginosa* mutant *ΔpilH,* whose T4P retraction frequency is approximately twice the one of WT (Figure 4.7a). *ΔpilH* formed biofilms more rapidly than WT: we observed dense aggregates as early as 2h, while we only did after 4h for WT (Figure 4.7b and c). In addition, *ΔpilH* induced more rapid mucus contraction than WT (Figure 4.7d), consistent with simulations. After 5.5h, WT and *ΔpilH* biofilms had similar morphologies and size, suggesting biofilm fusion reaches a physical limit most likely due to packing at the mucus surface (Figure 4.7b and c). Overall, our results support a model where *P. aeruginosa* contracts the surface of mucus by active T4P retraction. Single cells initially twitch on mucus to form small aggregates. The static aggregates collectively generate forces from T4P that are sufficient to deform their substrate, driving large-scale mucus contraction. By contracting, mucus brings aggregates closer. They eventually fuse and form biofilms (Figure 4.8).
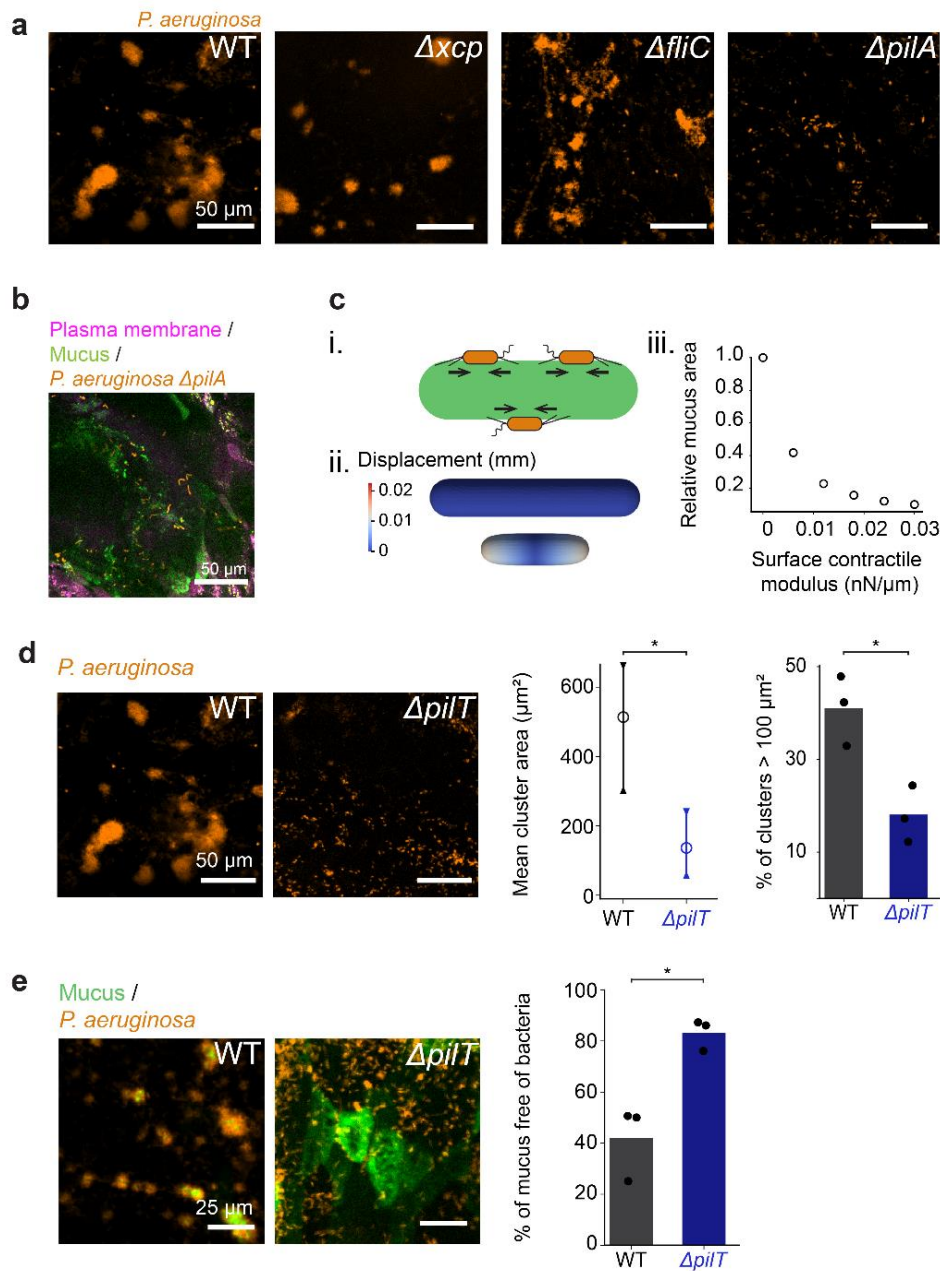
Figure 4.6: T4P retraction mediates aggregate formation by rearranging mucus.

(a) Biofilm formation of PAO1 mutants unable to degrade mucus or to generate force (t = 5.5h). Both the *Δxcp* mutant (lacking type II secretion system necessary for secretion of mucinases) and the *ΔfliC* mutant (lacking flagella) form biofilms similar to WT. In contrast, the *ΔpilA* mutant lacking T4P was unable to form biofilms in AirGels. (b) T4P are necessary for mucus contraction but not for attachment. *ΔpilA* mutant *P. aeruginosa* infecting a 35-days old, healthy AirGel. 3h25 after inoculating the bacteria, aggregates were still absent. However, the bacteria colocalized with the mucus, indicating that T4P are not necessary for adhesion to mucus. (c) Finite element simulations of mucus deformation during surface contraction. i. schematic representation of *P. aeruginosa* applying contractile force on mucus by retracting T4P. ii. finite element simulation of deformation of a mucus cylinder at rest (top) and under active surface stress (bottom). Colormap indicate displacement of surface elements. iii. relative mucus area as a function of surface contractile modulus. As the surface contractile modulus increases, the relative area of mucus decreases. (d) T4P retraction is necessary for biofilm formation. Images compare biofilms from WT *P. aeruginosa* and from the *ΔpilT* mutant unable to retract T4P (t = 5.5h). *ΔpilT* cluster area and percentage of large clusters is significantly smaller than WT (N = 3). Statistics: independent samples Student t-test with Bonferroni correction (p = 0.035 and p = 0.015). (e) Mucus does not rearrange during *ΔpilT* colonization (t = 5.5h). Most of the mucus surface remains free of bacteria during *ΔpilT* colonization (N = 3). Statistics: independent samples Student t-test with Bonferroni correction (p = 0.01).
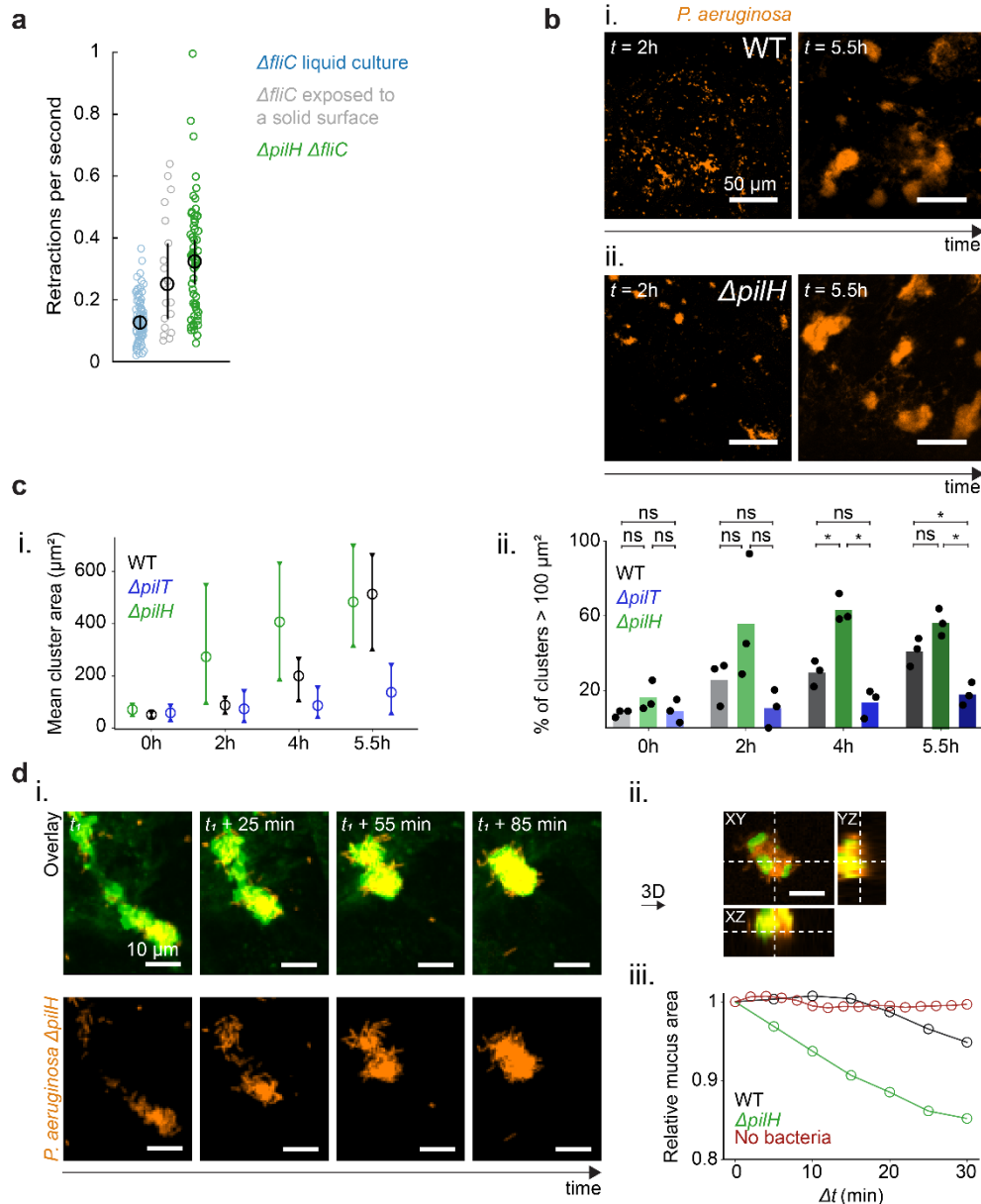
Figure 4.7: Aggregate formation via mucus contraction depends on T4P retraction rate.

(a) T4P retraction frequency increases during surface contact and is constitutively high in a *pilH* deletion mutant. T4P retraction rates were measured by interferometric scattering (iSCAT) microscopy, which allows for label-free T4P visualization[4]. To prevent cells from swimming away during the iSCAT measurements, a flagellum-less *ΔfliC* mutant was used as background strain. This strain was either grown in liquid or pre-adapted to culture on a solid surface for 3h. Black circles and bars indicate the bootstrap median and 95% confidence interval of the medians, respectively. (b) Increased T4P activity speeds up biofilm formation on mucus. Comparison of biofilm formation by i. the *ΔpilH* mutant with hyperactive T4P versus ii. WT, at t = 2h and t = 5.5h after inoculation. *ΔpilH* already forms small biofilms after 2h. (c) i. kinetics of biofilm size for WT, *ΔpilT* and *ΔpilH*. For each strain, we infected three AirGels from a healthy donor. Bars represent the range between the maximum and minimum of the means from triplicates, circles represent the overall mean. ii. comparison of percentage of large clusters for WT, *ΔpilT* and *ΔpilH*, over time. Statistics: one-way ANOVA for each time point, followed by a post-hoc Tukey test if the null hypothesis was rejected. At t = 4h, the differences between WT and *ΔpilH* (p = 0.003) and between *ΔpilH* and *ΔpilT* (p = 0.001) were significant. At t = 5.5h, the differences between WT and *ΔpilT* (p = 0.02) and between *ΔpilH* and *ΔpilT* (p = 0.001) were significant. (d) *ΔpilH* dramatically contracts mucus. i. timelapse images showing an event of mucus contraction by *ΔpilH*. ii. orthogonal views of the bacteria-covered mucus cluster at t_1 + 85 min, showing that PAO1 *ΔpilH* cells surround mucus. iii. relative mucus area changes measured during 30 min for WT and *ΔpilH*; since *ΔpilH* starts aggregating and remodeling mucus earlier than WT, the starting points of the recording differed (*ΔpilH*: 2.5h, WT: 6.2h, negative control: 8.1h). Images are maximal intensity projections of z-stacks throughout the figure except for the orthogonal projection in H.
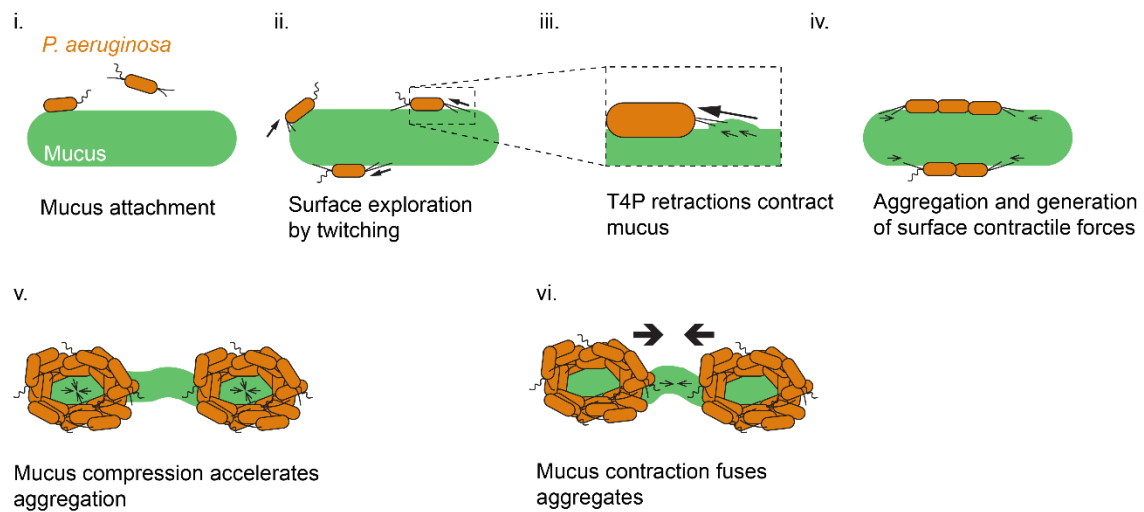
Figure 4.8: Proposed model for rapid *P. aeruginosa* biofilm formation on airway mucus.

i) Single bacterial cells attach to mucus. ii) *P. aeruginosa* navigates the mucus surface using T4P-dependent twitching motility. iii) T4P retraction locally contracts mucus. iv) Surface exploration promotes encounters between single cells. This initiates aggregation and the formation of small clusters. These clusters remain static on mucus. As single cells in aggregates use T4P to pull on and contract mucus, they generate surface contractile forces. v) Collective retraction of T4P from many cells compacts bacterial aggregates. vi) Still under the action of retractile T4P forces, aggregates further contract mucus to initiate fusion into biofilms.

4.2.3 Discussion

We used AirGels, tissue-engineered human lung organoids, to investigate how *P. aeruginosa* forms biofilms at the airway mucosal surface. We found that *P. aeruginosa* forms biofilms via an active mechanism of mucus remodeling. *P. aeruginosa* attaches to mucus and subsequently uses T4P to generate surface contractile forces. As a result, the mucus gel contracts, effectively reducing its area and bringing mucus-bound bacteria closer to each other. After this initial biofilm seeding, *P. aeruginosa* may initiate the secretion of matrix components to strengthen the cohesion of the biofilm.

T4P play multiple functions during biofilm formation in many species. In *P. aeruginosa*, successive T4P extension and retraction power twitching motility on surfaces[4,143]. This allows freshly attached cells to explore the environment, stimulating cell-cell encounters that nucleate aggregation[143]. These microcolonies ultimately mature into full biofilms. This model however falls short on soft surfaces. Hydrogels with low stiffness limit the transmission of T4P traction force to the surface thereby impairing twitching motility, but at the same time still enable biofilm formation[15]. Mucus contractions induced by *P. aeruginosa* show that T4P-generated forces can remodel soft materials as well. In

addition to highlighting a new mode of biofilm formation, this mechanism provides additional evidence that bacteria can mechanically remodel the host microenvironment[21].

Although the classical view of airway infections associates biofilms with chronic infections and planktonic cells with acute infections, recent work has demonstrated the coexistence of these bacterial lifestyles in sputum samples from both acutely and chronically infected patients[79]. Our observations of early biofilm formation in AirGels is therefore consistent with these clinical observations. However, *in vitro*, the effect of mucus on biofilm formation depends on the experimental protocol: while native mucins in solution inhibit biofilm formation[132–134], studies with full mucus or commercial mucins instead report increased aggregation[128,129,131]. This demonstrates that mucus-pathogen interactions vary dramatically depending on the model system used, thereby highlighting the importance of carefully reproducing and controlling relevant parameters *in vitro*.

Forming biofilms early on could provide a fitness advantage to *P. aeruginosa* in the non-hospitable airway environment. For example, bacterial aggregation could reduce *P. aeruginosa*'s susceptibility to neutrophils which are rapidly recruited to the mucosal surface during infection[144,145]. At the same time, forming biofilms increases *P. aeruginosa* tolerance to antibiotic treatment and promotes the emergence of resistant mutants[31]. There is however an upside for the host: mucus adsorbs a large proportion of the planktonic *P. aeruginosa*, keeping them away from the epithelium. Our results therefore highlight the duality of mucus: protecting the airway epithelium from acute infections, while providing a fertile ground for biofilm formation that favors chronic infections.

Most investigations of host-pathogen interactions have so far mainly relied on animal models and immortalized cell lines. Their limitations have been an obstacle to establish a holistic understanding of infections. By developing AirGels, we provide the community with a 3D airway infection model that expresses relevant cell types, secretes mucus, and is compatible with high-resolution imaging in presence of an air-liquid interface. As a result, AirGels have a strong potential in bridging the gap between *in vivo* and *in vitro* investigations of airway infections. Since AirGels are modular, we envision that engineering refinements could improve their suitability as an infection model for a wide

range of organisms. In addition, characterizing the rheological and chemical properties of the mucus lining would allow a better connection between investigations in AirGels and clinical observations. In summary, alternative approaches that leverage engineered microenvironments will help us better comprehend bacterial physiology in realistic infection contexts, which could ultimately allow the discovery of novel therapeutic strategies against antibiotic-resistant infections.

4.3 Appendix: detailed methods for the investigation of *P. aeruginosa* biofilms in AirGels

These methods have been adapted from the preprint posted on bioRxiv in May 2022 (and updated in December 2022), as:

Tamara Rossy, Tania Distler, Joern Pezoldt, Jaemin Kim, Lorenzo Talà, Nikolaos Bouklas, Bart Deplancke, Alexandre Persat*, *Pseudomonas aeruginosa contracts mucus to rapidly form biofilms in tissue-engineered human airways*.

DOI: https://doi.org/10.1101/2022.05.26.493615

Affiliations:

Tamara Rossy, Tania Distler, Lorenzo Talà & Alexandre Persat: Institute of Bioengineering and Global Health Institute, School of Life Sciences, École Polytechnique Fédérale de Lausanne, Lausanne, 1015, Switzerland.

Joern Pezoldt and Bart Deplancke: Institute of Bioengineering, School of Life Sciences, École Polytechnique Fédérale de Lausanne, Lausanne, 1015, Switzerland.

Jaemin Kim and Nikolaos Bouklas: Sibley School of Mechanical and Aerospace Engineering, Cornell University, Ithaca, NY, USA

4.3.1 Bacterial strains, plasmids and culture conditions

We used *Pseudomonas aeruginosa* PAO1 (WT or mutants, listed in Table 4.1) for all the infection experiments. Most strains were made to constitutively express the fluorescent protein mScarlet following a published protocol[146] using the plasmids listed in

Table 4.2. The backbone plasmid pUC18t-Mini Tn7 with gentamycin resistance was purchased from Addgene and isolated from *E. coli* XL10 Gold by GeneJET Plasmid Miniprep Kit (Thermo Fisher). The isolated plasmid was digested with the restriction enzymes HindIII and BamHI. The Ptet promoter was amplified by PCR using *P. aeruginosa* PAO1 genomic DNA and the mScarlet gene was amplified from a pre-existing plasmid. The Ptet promoter and mScarlet was then fused via Fusion PCR by overlapping extension. The resulting extended product was digested with HindIII and BamHI, then ligated to the digested pUC18t-MiniTn7 Gm backbone. Since this plasmid included a gentamycin resistance cassette, we grew the fluorescent PAO1 strains overnight in LB medium with 30 µg/ml gentamycin. The next morning, we diluted the stationary cultures 1:1000 in plain LB and let them grow 3-4h before infecting AirGels.

Table 4.1: Strains used in this study

Strain	Relevant characteristics	Source / Reference
Pseudomonas aeruginosa PAO1 (ATCC 15692)	WT PAO1	[147]
PAO1 mScarlet	WT PAO1 with constitutive chromosomal mScarlet expression	This study
PAO1 *Δxcp*	*xcpP* to *xcpZ* chromosomal deletion (called DZQ40 in the original study)	[148]
PAO1 *Δxcp* mScarlet	PAO1 *Δxcp* with constitutive chromosomal mScarlet expression	This study
PAO1 *ΔfliC*	In-frame deletion of PA1092	[149]
PAO1 *ΔfliC* mScarlet	PAO1 *ΔfliC* with constitutive chromosomal mScarlet expression	This study
PAO1 *ΔpilA*	In-frame deletion of PA4525	[149]
PAO1 *ΔpilA* mScarlet	PAO1 *ΔpilA* with constitutive chromosomal mScarlet expression	This study
PAO1 *ΔpilT*	In-frame deletion of PA0395	[149]
PAO1 *ΔpilT* mScarlet	PAO1 *ΔpilT* with constitutive chromosomal mScarlet expression	This study
PAO1 *ΔpilH*	In-frame deletion of PA0409	[150]
PAO1 *ΔpilH* mScarlet	PAO1 *ΔpilH* with constitutive chromosomal mScarlet expression	This study
PAO1 *ΔfliC ΔpilH*	In-frame deletion of PA1092 and PA0409	[151]

Table 4.2: Plasmids used in this study

Plasmid	Source	Reference
pTNS2	Addgene 64968	[152]
pUC18T-mini-Tn7T-Gm-Ptet_mScarlet	Addgene 63121 with Ptet promoter fused to mScarlet	This study

4.3.2 Infection of AirGels

The night before infection, AirGels were stained with the plasma membrane dye CellMask Deep Red (Life Technologies). The dye was diluted to 5 µg/ml and loaded in both the apical and basal compartments. The next morning, the lumen was again exposed to air for 3-4h. Mucus was stained with jacalin as described above, and all luminal fluid was then aspirated. Finally, we infected AirGels with mScarlet *P. aeruginosa*. We measured the optical density of our exponential bacterial cultures and centrifuged them for 2-3 min at 5000 rpm. We discarded the supernatant and resuspended the pellet in D-PBS to reach an optical density value of approximately 3. We then loaded 0.5 µl of bacterial culture in the lumen of AirGels (this small volume allowed for ALI maintenance). The resulting multiplicity of infection was approximately 10. For the infection shown in Figure 4.1, we started with a stationary *P. aeruginosa* culture that we diluted in D-PBS to an optical density of ~0.035. We then dipped a sterile toothpick in the culture and lightly touched the inlet of an AirGel with it in order to deposit bacteria while maintaining the ALI. This second method may mechanically compromise the epithelium with the toothpick, we therefore opted for the first one in most experiments.

The chips were then placed in an UNO-T-H-CO2 stage-top incubator (Okolab) for temperature, humidity and CO_2 control. The environment was maintained at 37°C and 5% CO_2, and connected to a bottle of Milli-Q water for humidification. Since condensation frequently appears on the PDMS chip during imaging, we placed pieces of Kimtech Science™ Kimwipes™ (Kimberly-Clark Professional) in the inlet ports of AirGels; this prevented dripping water from disrupting the ALI conditions. We visualized the infection progress over time with the aforementioned spinning disk confocal microscope. For WT, *ΔpilT* and *ΔpilH*, we repeated the infections to reach *N* = 3 replicates per

condition. The AirGels for all 3 replicates were all made from the same healthy donor and were between 33- and 38-day-old at the time of infection.

4.3.3 Colonization of extracted mucus

We isolated mucus from 8.5-month-old NHBE cells grown on 0.4 µm pore size polyester Transwell membranes (Corning). To do so, we immersed the apical side of the membranes in a jacalin-fluorescein solution (50 µg/ml in D-PBS) and we placed them in a cell culture incubator for 30 min. We then collected all fluid from the apical side with a pipette and dispensed 12.5 µl into 4 mm PDMS gaskets bonded to a glass-bottom dish (1.5 coverslip, glass diameter 20 mm, MatTek). We filled the space around the PDMS gasket with D-PBS to prevent dehydration of the mucus. We then centrifuged an exponential *P. aeruginosa* mScarlet culture at 5000 rpm for 3 min and resuspended them in D-PBS before loading 15 µl on the labeled mucus. We then placed the dish in the stage-top incubator and imaged the bacteria and mucus with the confocal spinning disk microscope described above.

4.3.4 Twitching motility on mucus

We infected a 4-month-old healthy HBE Transwell with *P. aeruginosa* mScarlet as follows. We loaded 3.3 µl of early exponential culture (~10^5 colony-forming units) on the apical side of the HBE culture, which had been labeled with fluorescent jacalin. We carefully took the Transwell insert out of the cell culture plate using sterile tweezers and we placed it on a glass-bottom dish (1.5 coverslip, MatTek). We then placed the dish in a stage-top incubator and recorded time-lapse videos of twitching bacteria with our spinning-disk confocal microscope. Because of the lack of culture medium in the visualization setup, recordings could not last long and would dehydrate within minutes.

4.3.5 Biofilm image acquisition and analysis

We acquired z-stack of infected AirGels over a 35 µm-deep range at different time points (t = 0h, 2h, 4h and 5.5h ± 0.5h). Since the AirGel surface is curved, we projected images in 2D using the maximal intensity projection tool in Fiji in order to facilitate downstream analysis. All the subsequent analysis steps were done in Jupyter Notebooks[120].

We started by quantifying the sizes of bacterial clusters. First, we visually inspected the pictures: if there were large intensity variations (e.g. in case of a mix of dim single cells and bright clusters), we saturated bright pixels to 1.5 times the mean intensity of the picture. We then segmented the pictures using Otsu thresholding (from the 'opencv' Python package[153], version 4.5.4.60) and visually assessed the result. In the rare cases where the segmentation was not deemed satisfactory (i.e. if some features were not detected properly or if there was too much noise), a simple threshold was manually selected. The pictures were then closed and filtered; more specifically, we removed any object smaller than ~6 µm^2 (20 pixels), which approximately corresponds to the area of a single cell. We then obtained the area of each cluster using the function 'regionprops' ('scikit-mage' Python package[154], version 0.19.2), which calculates properties of segmented objects in binary pictures. We calculated the mean cluster area for each replicate; then, for each condition, we plotted the maximum, minimum and mean of the means (e.g. Figure 4.2a). We also computed and plotted the proportion of aggregates larger than 100 µm^2.

We then quantified colocalization between mucus and bacteria. The segmentation and filtration of mucus pictures was identical as for bacterial clusters. Then, using the logical '&' function, we identified the pixels that were common between the binary pictures from the bacterial and mucus channels. With 'regionprops', we obtained the areas of these common zones and we normalized them to the total area of mucus. Thus, we could find the proportion of mucus that was covered in bacteria. We finally calculated the proportion of mucus devoid of bacteria as follows: 1 – (proportion of mucus covered in bacteria).

To quantify the contraction of a patch of mucus, we first canceled the effects of drift by registering the images in Fiji using the 'Correct 3D drift' plugin. We then manually tracked the displacement of $N = 7$ reference features with the Fiji plugin 'Manual Tracking'. We loaded the trajectories in a Jupyter Notebook and calculated the distances between each pair of positions over time. We finally normalized the resulting data to the initial distances and plotted them, along with the mean and standard deviation at each time point (Figure 4.5c).

Finally, we also measured mucus shrinkage over time for WT, *ΔpilH* and an uninfected control AirGel. To do so, we used images from 30 min timelapses (the starting point of the timelapses differed: 6 h 10 min for WT, 2 h 30 min for *ΔpilH*, and 8 h 5 min for the negative control). We segmented and quantified mucus areas as described above for each time point, and normalized it to the initial area (Figure 4.7d).

4.3.6 iSCAT-based quantification of T4P retraction frequency

P. aeruginosa were grown as previously described[151]. Briefly, an overnight culture was obtained from a single colony and grown in LB at 37°C with 290 rpm shaking. The overnight culture was diluted 1:500 or 1:1000 and grown for 2 to 3 hours to obtain a mid-exponential phase culture. For surface-grown cells, 100 µl of the mid-exponential phase cell suspension were plated on LB 1 % agarose, grown for 3 h at 37 °C and harvested in 500 µl LB by gentle scraping. Cells were diluted to OD600 0.02 to 0.05 prior to visualization. Both liquid- and solid-grown cells were either loaded on 500 µm x 140 µm PDMS microchannels or in 6 mm PDMS gaskets. Cells sticking to the surface were visualized without flow with iSCAT and movies were recorded at 10 fps for either 2 min, 1 min or 30 s. Raw iSCAT images were processed as described previously[4,151]. Individual movies were manually analyzed using Fiji[115] by counting the total number of TFP in each cell as well as the number of TFP retractions represented by tensed TFP. The residence time of each cell on the coverslip was also recorded. For each cell we computed the retraction frequency by dividing the total number of retractions by the residence time of the cell on the coverslip. Finally, we computed a bootstrap median retraction frequency and 95% confidence interval by pooling the data obtained by all three biological replicates. Data analysis was performed using Matlab R2020a (Mathworks).

4.3.7 Statistical analysis

All statistical tests were run in Python using Jupyter Notebooks[120]. Independent or paired-samples Student t-tests were performed with Bonferroni correction using the function 'add_stat_annotation' from the statannot package[155] (version 0.2.3). One-way ANOVAs were run using the function 'f_oneway' in the 'stats' module from SciPy[156] (version 1.7.3). When the ANOVA result rejected the

null hypothesis, we followed up with a post-hoc Tukey test using 'stats.multicomp.pairwise_tukeyhsd' from the 'statsmodels' module[157].

4.3.8 Computational model of mucus remodeling by T4P

We refer the reader to our previous work[142,158] for the general theory on the kinematics of the surface and the volume of a 3D soft body, focusing on cell-laden microtissues. Specific considerations on the implementation of this work are introduced in the following formulations.

Kinematics

Let V be a fixed reference configuration of a continuum body $\mathcal{B}$. We use the notation $\chi: V \to \mathbb{R}^3$ for the deformation of body $\mathcal{B}$. A motion χ is the vector field of the mapping $\boldsymbol{x} = \chi(\mathbf{X})$, of a material point in the reference configuration $\mathbf{X} \in V$ to a position in the deformed configuration $\boldsymbol{x} \in v$. The kinematics of a material point are described by

$$\mathbf{u}(\mathbf{X}, t) = \boldsymbol{x}(\mathbf{X}, t) - \mathbf{X} \tag{S1}$$

where $\mathbf{u}(\mathbf{X}, t)$ is the displacement vector field in the spatial description. The kinematics of an infinitesimal bulk element are described by

$$\mathbf{F}(\mathbf{X}, t) = \frac{\partial \chi(\mathbf{X}, t)}{\partial \mathbf{X}} = \nabla_{\mathbf{X}} \boldsymbol{x}(\mathbf{X}, t) \tag{S2}$$

$$\mathbf{F}^{-1}(\boldsymbol{x}, t) = \frac{\partial \chi^{-1}(\boldsymbol{x}, t)}{\partial \boldsymbol{x}} = \nabla_{\boldsymbol{x}} \mathbf{X}(\boldsymbol{x}, t) \tag{S3}$$

where $\mathbf{F}(\mathbf{X}, t)$ and $\mathbf{F}^{-1}(\boldsymbol{x}, t)$ are the deformation gradient and inverse deformation gradient, respectively. Note that $J(\mathbf{X}, t) = \mathrm{d}v/\mathrm{d}V = \det \mathbf{F}(\mathbf{X}, t)$ is the Jacobian determinant defining the ratio of a volume element between material and spatial configuration.

A motion of an arbitrary differential vector element can be mapped by the deformation gradient $\mathbf{F}$. However, a unit normal vector $\mathbf{N}$ in the reference configuration cannot be transformed into a unit normal vector $\mathbf{n}$ in the current configuration via the deformation gradient[159], motivating us to develop

the kinematics of an infinitesimal surface element[160]. Note that we utilize $\{\widehat{\bullet}\}$ to denote the surface quantity bounded by outer surface denoted as $\partial\Omega_0$.

$$\widehat{\mathbf{F}}(\mathbf{X}, t) = \frac{\partial\chi(\mathbf{X}, t)}{\partial\mathbf{X}} \cdot \widehat{\mathbf{I}} = \widehat{\nabla}_{\mathbf{X}} x(\mathbf{X}, t) \tag{S5}$$

$$\widehat{\mathbf{F}}^{-1}(\boldsymbol{x}, t) = \frac{\partial\chi^{-1}(\boldsymbol{x}, t)}{\partial\boldsymbol{x}} \cdot \widehat{\boldsymbol{\imath}} = \widehat{\nabla}_{\boldsymbol{x}} \mathbf{X}(\boldsymbol{x}, t) \tag{S6}$$

where $\widehat{\mathbf{F}}(\mathbf{X}, t)$ and $\widehat{\mathbf{F}}^{-1}(\boldsymbol{x}, t)$ are the deformation gradient and inverse deformation gradient, respectively. Note that $\widehat{\mathbf{I}} = \mathbf{I} - \mathbf{N}\otimes\mathbf{N}$ and $\widehat{\boldsymbol{\imath}} = \boldsymbol{\imath} - \mathbf{n}\otimes\mathbf{n}$ are the mixed surface unit tensors, where $\mathbf{I}$ and $\boldsymbol{\imath}$ are the unit tensors, and $\mathbf{N}$ and $\mathbf{n}$ are the outward unit normal vectors, in reference and current configuration, respectively. Note that $\hat{J}(\mathbf{X}, t) = \mathrm{d}a/\mathrm{d}A = |\mathrm{cof}\,\mathbf{F} \cdot \mathbf{N}|$ is the Jacobian determinant defining the ratio of an area element between material and spatial configuration.

Equilibrium

The total potential energy functional $W(\chi)$ is defined as:

$$\begin{aligned} W(\chi) = &\int_{\Omega_0} \Psi(\mathbf{F}, \chi; \mathbf{X})\mathrm{d}V + \int_{\partial\Omega_0} \widehat{\Psi}(\widehat{\mathbf{F}}, \chi; \mathbf{X})\mathrm{d}S - \int_{\Omega_0} \mathbf{B} \cdot \mathbf{u}(\chi; \mathbf{X})\mathrm{d}V \\ &- \int_{\partial\Omega_0} \mathbf{T} \cdot \mathbf{u}(\chi; \mathbf{X})\mathrm{d}S \end{aligned} \tag{S9}$$

where Ψ and $\widehat{\Psi}$ are strain energies in bulk and on surface, and $\mathbf{B}$ is the reference body force and $\mathbf{T}$ is the surface traction. An equilibrated configuration is obtained by minimizing this functional considering all admissible deformations $\delta\chi$. It is important to note that the strain energies $(\Psi, \widehat{\Psi})$ can be varied depending on the bacterium and mucus models so that the following sections can be written in a single formulation for brevity, and the specific strain energies are to be defined below.

Following the derivation presented in [161], we can finally arrive at a set of localized force balance equations. Neglecting the inertial effect, the local form of linear and angular momentum balances for bulk and surface are defined by

$$\nabla_{\mathbf{X}} \cdot \mathbf{P} + \mathbf{B} = \mathbf{0} \quad \text{in } V \tag{S10}$$

$$\widehat{\nabla}_{\mathbf{X}} \cdot \widehat{\mathbf{P}} + \mathbf{T} - \mathbf{PN} = \mathbf{0} \quad \text{on } S \tag{S11}$$

$$\mathbf{u} = \breve{\mathbf{u}} \quad \text{on } S_u \tag{S12}$$

$$[\![\widehat{\mathbf{P}}\widehat{\mathbf{N}}]\!] = 0 \quad \text{on } L$$

where $\breve{\mathbf{u}}$ is the prescribed displacement on the boundary S_u, $\widehat{\mathbf{N}}$ is the bi-normal vector to the boundary curve, and $[\![\bullet]\!]$ indicates summation over surfaces intersecting on boundary curves[160].

Weak Form

For the finite element implementation, we need to obtain the weak form for our problem. By adding the constraint that the first variation of the total potential energy must be equal to zero $\delta W(\chi) = 0$, we obtain a weak form statement as

$$G = \int_{\Omega_0} \mathbf{P} : \nabla_{\mathbf{X}} \delta\mathbf{u} \, dV + \int_{\partial\Omega_0} \widehat{\mathbf{P}} : \widehat{\nabla}_{\mathbf{X}} \delta\mathbf{u} \, dS - \int_{\Omega_0} \mathbf{B} \cdot \delta\mathbf{u} \, dV - \int_{\partial\Omega_0} \mathbf{T} \cdot \delta\mathbf{u} \, dS$$
$$= 0 \quad \forall \, \delta\mathbf{u} \tag{S13}$$

where $\delta\mathbf{u}$ is the admissible deformation field.

We employed the open-source platform FEniCS[162], to implement the finite element simulation. We used the Scalable Nonlinear Equations Solvers (SNES) from the open-source toolkit PETSc[163], which provides numerical computations of a Newton-type iterative procedure to solve the nonlinear variational problem. Note that the value of γ should be ramped from zero to its prescribed value for numerical stability as the problem is highly nonlinear.

Constitutive Relations

To relate the active stress with deformation, we must specialize our choice for the strain energies in the bulk and on the surface. For the deformation of compressible tissue, we consider a passive bulk

energy Ψ^p that captures the permanent elasticity of the collagen network, and for the contribution of bacterium contractility, we can consider the active surface energy $\widehat{\Psi}^a$ that accounts for the action of the bacterium on the surface of mucus tissue.

a. Passive mucus model

The passive strain energy density Ψ^p describes the elasticity of mucus tissue. We consider the mucus as a soft, highly deformable and highly compressible hyperelastic material, but we neglect it's biphasic and viscoelastic nature in terms of energy dissipation. We choose the compressible Neo-Hookean model [158,159] for the mucus.

$$\Psi^p = \frac{K}{2}(J-1)^2 + \frac{G}{2}(I_1 - 3 - 2\ln J)$$

(S14)

where K and G are the bulk and shear moduli.

b. Active model for the contractile action of bacteria

We assume that the bacteria-mucus interaction can be described through a surface strain energy generating constant surface stresses similar to fluid-like surface tension[142,158]. Bacteria exert a contractile force on the periphery of the mucus, and we recapitulate this action through an active surface energy $\widehat{\Psi}^a$. We postulate that the surface energy $\widehat{\Psi}^a$ is a function of the change of the surface area $\hat{J}$.

$$\widehat{\Psi}^a = \gamma \hat{J}$$

(S15)

where γ is a surface contractile modulus (energy per unit area) representing the contractility of bacterium on the surface at the equilibrium state. It is important note that we consider no bulk contractility due to the bacteria as results verify their presence only on the periphery of the mucus.

c. Energy penalization

As at high level of contraction the bacteria are bound to jam, barring the additional contraction of the mucus (even if the material itself can accommodate it), we have to enforce this jamming transition. Assuming that we know the initial surface concentration of bacteria we enforce the kinematic constraint via energy penalization. From the experimental observation, we enforce the surface area of deformed mucus tissue cannot be smaller than a ratio ($\hat{J}_{pen}$) of the initial surface area. An appropriate energy penalization $\hat{\Psi}_{pen}$ for enforcing the prescribed surface condition is given by

$$\hat{\Psi}_{pen} = \frac{P}{2} \langle \hat{J}_{pen} - \hat{J} \rangle^2 \tag{S16}$$

where P is the penalty parameter (energy per unit area), and $\langle \bullet \rangle$ is the Macaulay brackets that used to describe the ramp function,

$$\langle x \rangle = \begin{cases} x & (x > 0) \\ 0 & (x \leq 0) \end{cases} \tag{S17}$$

Finite Element Simulation

The reference (undeformed) state corresponds to a state where the active contractile moduli are set to zero. Experimentally, this reference state corresponds to the initial state of the mucus right after the mixing of mucus and bacterium and before the application of forces by encapsulated bacterium. The reference configuration for the finite element simulations represents the geometry shown in Figure 4.6c. The entire surface is allowed to actively contract through increasing the surface contractile modulus up to an equilibrium value. The final (deformed) state is defined when the surface contractile moduli γ reaches its prescribed value, and no external loads are applied. Experimentally, this corresponds to the equilibrium state of the mucus. The final configurations represent the equilibrium states.

Parameter Calibration

The parameters of the model are the bulk and shear moduli, K and G, and surface contractile modulus, γ, penalty parameter, P and penalty surface ratio, $\hat{J}_{pen}$. There is a unique relationship between K, G, and Poisson's ratio ν, allowing to interchangeably use ν in place of K for the calibration procedure. We selected a set of parameters: $G = 1.0$ Pa, $\nu = 0.1$, $\gamma = 0.03$ nN/μm and $P = 1.0$ nN/μm. The corresponding bulk and elastic moduli were $K = 0.9$ Pa and $E = 2.2$ Pa within the range of reported values for mucus[36,164].

Chapter 5.　　Conclusion

Throughout my PhD, I studied biofilm formation in model systems that integrate realistic mechanical cues. In this chapter, I will summarize and discuss the key results before proposing additional perspectives to explore.

5.1 Achieved results and discussion

5.1.1 Cellular advective-diffusions underlies surface colonization by *C. crescentus*

As described in Chapter 2, I started by exposing the freshwater bacterium *C. crescentus* to controlled flow velocities in microfluidic channels, and by visualizing the resulting surface colonization patterns with fluorescence microscopy. I then developed an image analysis pipeline to quantify spatial patterns formed by the biofilms under different flow conditions. These patterns turned out to be governed by a cellular advective-diffusion mechanism. *C. crescentus* divides asymmetrically, yielding a stalked mother cell and a piliated daughter cell at each generation; thus, if the daughter cell does not immediately attach next to its mother upon division, its fate is determined by the balance between hydrodynamics and diffusion-like, flagellum-driven motility. In weak flow, bacterial swimming dominates, increasing the probability for the planktonic daughter cell to encounter and attach to the surface. On the other hand, it is likely to be flushed out of the channel in strong flow, where advective transport is the main contributor to the displacement of planktonic cells. As a consequence, I observed that surface colonization rate and lineage mixing decreased with increasing flow velocity. Colonization in strong flows was characterized by the formation of large and sparse clonal clusters. Importantly, lineage distribution was independent of surface saturation, ruling out the possibility of a transient artifact stemming from the different rates of colonization. These results suggest that, by modulating the spatial organization of single cells, mechanical cues from the environment impact the evolution of social phenotypes within biofilms.

While the asymmetry of *C. crescentus* division is a key component of the cellular advective-diffusion process described in my thesis, similar mechanisms may still arise for different species, in environments with different geometries. For example, as discussed in Chapter 2, asymmetric distribution of signaling molecules related to EPS secretion is also found in *P. aeruginosa* and *E. coli*[55,70–72]. Even in the absence of any asymmetry, advective-diffusion can influence bacterial colonization of environments with more complex geometries. This was observed when *Shewanella oneidensis* was grown in microchannels with 2D baffle patterns: biofilms were only able to penetrate those microstructures under weak flows, when swimming motility occurred on timescales comparable to advective transport[46]. While this may not directly influence lineage mixing, it demonstrates once again that mechanical cues underpin bacterial colonization patterns. Beyond ecological consequences, understanding the impact of environmental conditions on biofilm organization could open new therapeutic avenues. As discussed by Nadell et al., numerous public goods secreted by biofilm-dwelling cells are also important virulence factors[9]. Thus, one would choose different therapeutic strategies depending on how social interactions influence virulence within the community (e.g. aiming either at minimizing or maximizing strain diversity)[9].

5.1.2 AirGel: advantages and limitations

In the second part of my PhD, I set off to model the respiratory tract, in which biofilms have been observed both in acute and chronic infections[79]. To do so, I used a tissue-engineering approach to generate a cylindrical lumen lined with human airway epithelial cells. The substrate in which the lumen was patterned is a cross-linked, optically transparent ECM gel, allowing for long-term cell culture, establishment of an ALI, and high-resolution microscopy. HBE cells successfully formed a tight epithelial barrier in AirGels. Furthermore, they differentiated into relevant airway cell types, comprising goblet cells, ciliated cells and basal cells. Directional, cilia-driven transport of fluorescent particles occurred in differentiated AirGels, suggesting that they recapitulate the MCC function of the airway.

Like every model system, however, AirGels also come with a few limitations. First, the rates of MCC measured in AirGels are in the lower limit of the physiological range reported for murine tracheal explants[80,85]. One of the reasons for the low median values shown in Chapter 3 comes from the fact that epithelium-bound, non-motile beads were not excluded from the calculation. Thus, the medians are an underestimate of the actual MCC velocity. Nevertheless, even the moving beads were mostly on the lower end of the physiological range. The explanation may lie in the humidity levels to which HBE cells are exposed during culture in AirGels. Kudo, Song, Yockey et al. have indeed demonstrated that mice housed in low ambient humidity conditions had reduced MCC[85]. Since the humidity levels are not precisely controlled in the incubators where AirGels are cultured, and since the ECM substrate is dense and thick, the conditions to which HBEs are exposed might be too dry. Consequently, careful examination of the physicochemical properties of mucus in AirGels would also be necessary to ensure that they match healthy *in vivo* values. Two additional limitations of AirGels are inherent to their fabrication protocol. First, because the lumen is generated through manual removal of PDMS rods, the surface of the ECM gel often comprises imperfections that alter the smoothness of the subsequent airway tissue. The second limitation is the working distance for microscopic visualization of AirGels. Because of the design of the PDMS scaffold, which includes thin membranes elevating the rod above the coverslip, the highest magnification objective that could be used was a 40X objective with a working distance of 610 μm. Reducing the thickness of these membranes is not possible with the 3D printer used to build the master mold for AirGels. Consequently, imaging intracellular physiological responses of the bacteria infecting AirGels, such as localization of specific proteins, would most likely not be feasible, as they would require higher magnification. However, the absence of a porous membrane in the field of view already constitutes a substantial improvement for imaging quality compared to Transwells or lung-on-chip devices. I therefore argue that AirGels are appropriate models for high resolution time-lapse monitoring of respiratory infections.

5.1.3 A new mechanism of biofilm formation on mucus

For that reason, as described in Chapter 4, I used AirGels to study biofilm formation by *P. aeruginosa* in the airway mucosa. Not only did this pathogen form biofilms on shorter timescales than previously reported from flow cell experiments[136], but it did so through an active mechanism of host mucus remodeling. By pulling with T4P, *P. aeruginosa* contracted the mucus layer, effectively reducing its area and bringing mucus-bound bacteria closer to each other. This resulted in accelerated aggregation. T4P retraction rate also appeared to influence the speed of biofilm formation; a hyperpiliated mutant with increased T4P activity indeed aggregated even faster than WT. The finding that *P. aeruginosa* remodels host material to its advantage is reminiscent of other infection processes. For instance, when *Listeria monocytogenes* is phagocytosed by host cells, it subverts the actin cytoskeletal machinery as a mean to propel itself through the cytoplasm and eventually spread to neighboring cells[165]. Similarly, both enteropathogenic and enterohemorrhagic *E. coli* trigger actin polymerization at their point of contact with the intestinal epithelium, leading to an intimate attachment of the bacteria to the tissue[166]. Enhanced biofilm formation through mucus contraction may therefore constitute yet another example of the ingenuity with which pathogens exploit host resources for their benefit.

However, as discussed in Chapter 4, the effect of mucus on biofilm formation depends on the experimental conditions: some groups reported an inhibitory effect of mucins[132–134], while others instead found it to promote aggregation[128,129,131]. The results obtained in AirGels are in line with the latter. There are important differences between AirGels and the experimental systems in which mucins prevented biofilm formation. First, these studies involved purified mucins instead of full mucus as secreted by goblet cells in AirGels. Other constituents of mucus, such as DNA, might thus counteract the inhibitory effect triggered by purified mucins. Furthermore, infections occurred at the ALI in AirGels, while most other studies performed experiments in immersed conditions. The lack of ALI may thus prevent biofilm formation, for instance by altering the mechanical properties of mucus, or by maintaining bacteria in a planktonic state. Consistent with these hypotheses, *P. aeruginosa* failed to form biofilms when mucus was extracted from Transwells and placed in phosphate buffer

saline, as shown in Figure 4.3c. Finally, as discussed above, whether the rheology of mucus in AirGels matches healthy *in vivo* conditions, and how this influences biofilm formation, is still to be determined. Overall, host-pathogen interactions vary dramatically depending on the model system used. This justifies approaches reproducing realistic environmental cues *in vitro*, like the one taken throughout my PhD thesis.

5.2 Future developments

While the work described in this thesis provided some insight into the influence of environmental cues on biofilm formation, it also opened the way for additional research directions to explore. Here, I provide a non-exhaustive list of questions that remain open.

5.2.1 Studying aquatic biofilms in settings that better mimic natural conditions

Biofilms in nature most often comprise multiple species. Therefore, growing *C. crescentus* with other aquatic bacteria in microfluidic channels would be relevant, especially since the response to fluid flow depends on the division, motility and adhesive properties of different strains. As discussed in Chapter 1, biofilm organization and social phenotypes dynamically influence each other[24]. Thus, flow-induced spatial patterns within biofilms might impact the resulting social interactions between different strains. A fairly straightforward way to study this would involve a mixed population of antibiotic-susceptible and antibiotic-degrading strains. One could expose them to a range of flow intensities in order to generate an array of initial spatial structures. Antibiotic treatment would then be applied. The resulting lineage distribution would most likely depend on the original pattern, since susceptible individuals within well-mixed populations are expected to benefit from the action of the degrading strain (Figure 5.1). Finally, natural environments are more complex than the straight microchannels used in my study. A future improvement could therefore consist in implementing more intricate geometries, like the pores, curves or baffles used in previous works[23,44–46]. Transient modifications of flow conditions – for example mimicking a seasonal change of water flow rate in a stream – would also constitute a relevant addition.
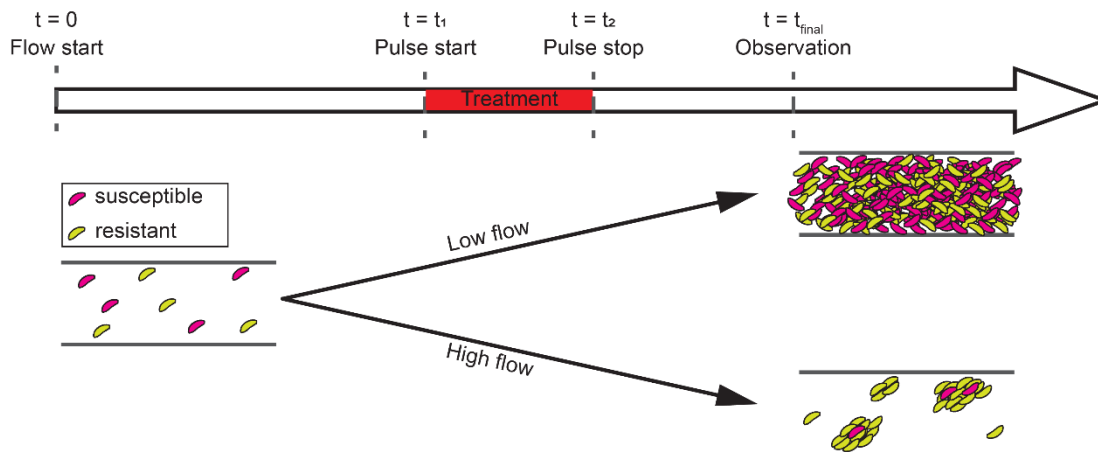
Figure 5.1: Proposed experiment to investigate the effects of spatial patterning on social interactions.

A mixture of antibiotic-susceptible and antibiotic-degrading *C. crescentus* would be loaded in a microfluidic channel at $t = 0$. They would be exposed to different intensities of fluid flow in order to generate distinct colonization patterns. Then, one would apply a pulse of antibiotic treatment at $t = t_1$. Depending on the initial lineage distribution, the spatial patterns at the end of the experiment are expected to differ as a response to the treatment.

5.2.2 Increasing the complexity of AirGels

In a similar manner, AirGels could also benefit from an increased complexity in order to better reproduce the airway environment. An important player currently missing is the immune system. For example, immune cells like macrophages or neutrophils could mitigate the acute infection phase and apply selective pressures driving the pathogen adaptation to the airway. Immune cells could either be seeded directly in the airway lumen, or on the basal side to mimic recruitment from the bloodstream. The latter would come with new questions and challenges, such as how well immune cells would migrate through the dense, cross-linked ECM. For an even more complete model system, AirGels could be upgraded with the addition of endothelial channels and fibroblasts in the matrix, as was attempted by Barkal and colleagues[105] (Figure 5.2).
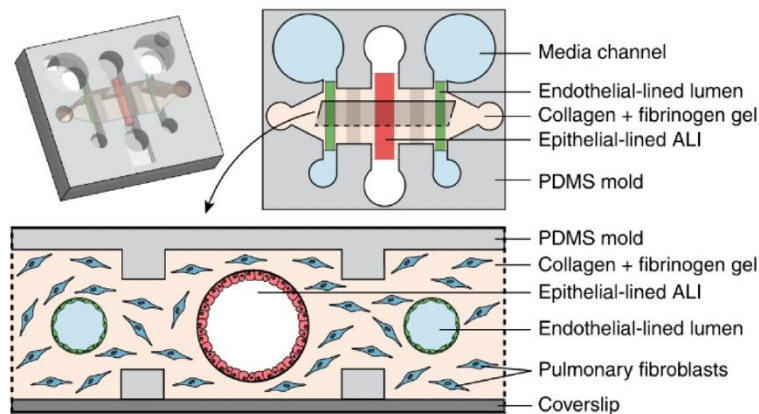
Figure 5.2: Organotypic lung model developed by Barkal et al.

Such design could be applied to AirGels to further recapitulate important features of the human lung. Image taken from [105].

To investigate the role of the tree-like geometry of the airway – e.g. to visualize if pathogens preferentially accumulate at the junction of several bronchi – the current fabrication protocol of AirGels can be easily adapted to generate a lumen with a branching point, based on a published method[101]. As a proof-of-concept, I built an AirGel with a branched lumen (Figure 5.3) and stably grew and differentiated HBE cells in it. Although the fabrication process of the branched lumen could still be improved, this preliminary result constitutes an encouraging first step.
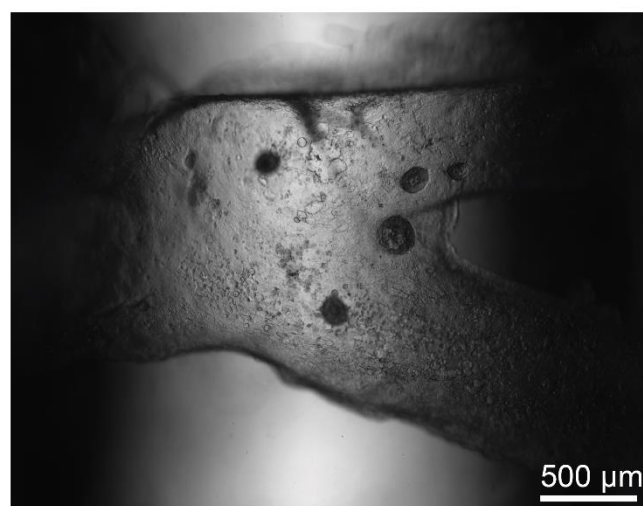
Figure 5.3: Proof-of-concept 6-days old AirGel with a branched lumen.

HBE cells from a CF donor successfully attached, grew and differentiated in a lumen comprising a branching point, to better reproduce *in vivo* architecture.

5.2.3 Towards using AirGels for disease modeling and personalized medicine

As described in Chapter 4, AirGels were successfully fabricated with cells from a CF donor (and subsequently infected with *P. aeruginosa*). Characterizing and infecting AirGels made from additional CF donors, as well as donors suffering from other diseases like COPD or asthma would thus be the next logical step. Beyond primary cells, the use of patient-derived iPSCs would open a whole new avenue of possibilities towards personalized medicine and genetic engineering. Unlike primary cells, iPSCs are not impaired by extensive passaging, thereby allowing for the selection and expansion of successfully transfected clones. Genetic engineering would be valuable both for real-time visualization of secreted, fluorescently-labeled mucins (as was done in mice[80]) and for mechanistic studies involving the knock-out of specific genes (e.g. to decipher the relative contributions of MUC5AC and MUC5B to biofilm formation). Moreover, patient-derived iPSCs would allow the study and correction of genetic mutations associated with respiratory diseases.

5.2.4 Infecting AirGels with clinically relevant strains

During my PhD, I only infected AirGels with laboratory strains of *P. aeruginosa.* In the future, the use of clinical isolates might provide insight into the role of different virulence factors in long-term infections. Similarly, integrating other microbes frequently found in infected lungs would emulate clinical conditions; for example, *S. aureus* and *P. aeruginosa* coinfections can persist for years in CF patients[167]. In addition, AirGels would be useful to quantify more precisely the rates at which pathogens grow and kill host cells during infections, for instance through time-lapse microscopy.

As mentioned several times throughout this thesis, biofilms are especially tolerant to antibiotics, and recurrent treatments drive the emergence of resistant mutants[31]. Therefore, a future direction to explore is the antibiotic susceptibility of the mucus-associated biofilms that form in AirGels. Also, *P. aeruginosa* strains isolated from the airway of chronically-infected CF patients often exhibit mutations promoting EPS secretion[124,126]. One might thus wonder what role is played by the matrix in the fast aggregation occurring in AirGels. I performed a preliminary experiment with mutant strains lacking the *pelA* or *pslBCD* genes responsible for EPS production in *P. aeruginosa* (Figure 5.4). These

mutants were able to form aggregates on mucus within hours, suggesting that EPS is not necessary for the rapid formation of mucus-associated biofilms. However, these results do not rule out the possibility that matrix is secreted by WT cells in the same time frame, nor that it may play an important role later in the infection process. Additional experiments would be required for a more comprehensive view of the role played by the biofilm matrix (such as staining the EPS with lectins, or integrating fluorescent reporters for genes like *pelA* or *pslBCD* in WT cells).
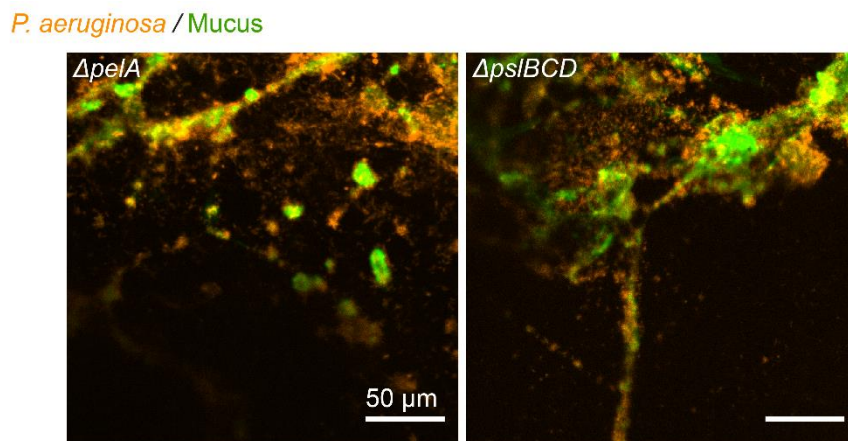
Figure 5.4: Formation of mucus-associated biofilms by matrix-deficient *P. aeruginosa*.

AirGels were stained with jacalin and infected with fluorescent *P. aeruginosa* mutants lacking genes for *pelA* and *pslBCD*, which are involved in EPS production. At *t* = 5.5h, bacteria and mucus were imaged by spinning disk confocal microscopy. Both mutants were able to aggregate on the host mucus, suggesting that the onset of biofilm formation in the airway is independent of matrix secretion.

5.2.5 Investigating the prevalence of mucus contraction by respiratory pathogens

Several questions related to the contraction of host mucus via T4P remain open. For instance, can other piliated strains or species trigger the same phenomenon? A preliminary result obtained by a postdoctoral researcher in our lab, Dr Lucas Meirelles, provides a partial answer to that question. Indeed, while I only infected AirGels with the *P. aeruginosa* strain PAO1, he found that *P. aeruginosa* PA14 also rapidly formed aggregates in the mucus layer of CF Transwells (Figure 5.5). Whether this is specific to *P. aeruginosa* or can be found in other species, like *Burkholderia cenocepacia*[168,169] or *Acinetobacter baumanii*[170], is still to be established. In the case of polymicrobial infections, investigating the interactions between strains that contract mucus and others that do not could also be of interest.
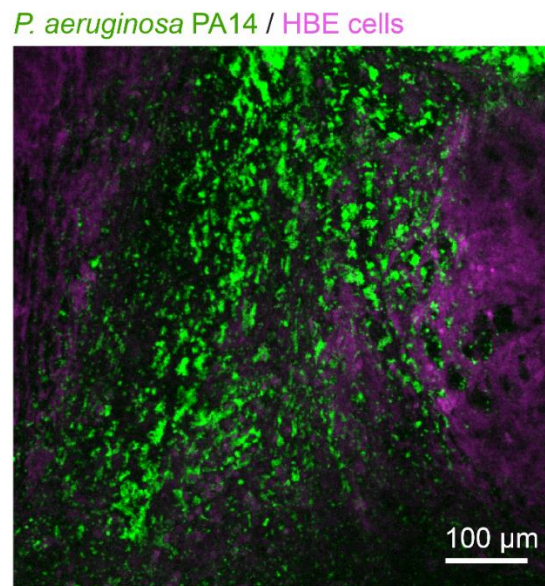
Figure 5.5: Aggregation of *P. aeruginosa* strain PA14 on CF mucus.

A fully-differentiated CF Transwell was infected with PA14 expressing GFP. After 15h, z-stacks were acquired by confocal spinning disk microscopy. Dense bacterial aggregates had formed on slices above the HBE cells and seemed to shake with the motion of the cilia (not shown), indicating they were located in the mucus layer. Image courtesy of Dr. Lucas Meirelles.

5.2.6 Elucidating the link between mucus rheology and biofilm formation

Finally, while Chapter 4 highlights a new mechanism of physical interaction between a pathogen and its host, the quantitative links between mucus mechanics, bacterial physiology and infection progress are still unknown. To overcome this issue, future experiments leveraging microparticle tracking rheology could be critical. With this technique, the viscoelastic properties of mucus could be characterized in AirGels throughout the infection and correlated to bacterial colonization or virulence, for example. The impact of rheological differences between healthy and diseased mucus would be particularly interesting to investigate. In addition, since the stickier mucus from sick individuals is more difficult for the cilia to clear, it may have to be coughed up[81]. One could thus apply strong bursts of airflow to mimic cough. The remaining biomass would then be quantified, and compared between AirGels secreting mucus with different viscoelastic properties.

Considering the myriad of questions that remain to be answered, research about bacterial colonization in realistic environments holds many promises for the future. Hopefully, the work

presented in this thesis can inspire new studies and encourage the microbiology community to take

mechanics into account in their choice of model system.

References

1. Persat, A. *et al.* The Mechanical World of Bacteria. *Cell* **161**, 988–997 (2015).

2. Dufrêne, Y. F. & Persat, A. Mechanomicrobiology: how bacteria sense and respond to forces. *Nat Rev Microbiol* **18**, 227–240 (2020).

3. Berne, C., Ellison, C. K., Ducret, A. & Brun, Y. V. Bacterial adhesion at the single-cell level. *Nat. Rev. Microbiol.* **16**, 616–627 (2018).

4. Talà, L., Fineberg, A., Kukura, P. & Persat, A. Pseudomonas aeruginosa orchestrates twitching motility by sequential control of type IV pili movements. *Nat Microbiol* **4**, 774–780 (2019).

5. Persat, A., Inclan, Y. F., Engel, J. N., Stone, H. A. & Gitai, Z. Type IV pili mechanochemically regulate virulence factors in Pseudomonas aeruginosa. *PNAS* **112**, 7563–7568 (2015).

6. Fuchs, E. L. *et al.* The Pseudomonas aeruginosa Vfr Regulator Controls Global Virulence Factor Expression through Cyclic AMP-Dependent and -Independent Mechanisms. *J Bacteriol* **192**, 3553–3564 (2010).

7. Baraquet, C., Murakami, K., Parsek, M. R. & Harwood, C. S. The FleQ protein from Pseudomonas aeruginosa functions as both a repressor and an activator to control gene expression from the pel operon promoter in response to c-di-GMP. *Nucleic Acids Research* **40**, 7207–7218 (2012).

8. Borlee, B. R. *et al.* Pseudomonas aeruginosa uses a cyclic-di-GMP-regulated adhesin to reinforce the biofilm extracellular matrix. *Molecular Microbiology* **75**, 827–842 (2010).

9. Nadell, C. D., Xavier, J. B. & Foster, K. R. The sociobiology of biofilms. *FEMS Microbiology Reviews* **33**, 206–224 (2009).

10. Flemming, H.-C. *et al.* Biofilms: an emergent form of bacterial life. *Nat. Rev. Microbiol.* **14**, 563–575 (2016).

11. Sauer, K. *et al.* The biofilm life cycle: expanding the conceptual model of biofilm formation. *Nat Rev Microbiol* 1–13 (2022) doi:10.1038/s41579-022-00767-0.

12.   Sauer, K., Camper, A. K., Ehrlich, G. D., Costerton, J. W. & Davies, D. G. Pseudomonas aeruginosa Displays Multiple Phenotypes during Development as a Biofilm. *Journal of Bacteriology* **184**, 1140–1154 (2002).

13.   Conrad, J. C. & Poling-Skutvik, R. Confined Flow: Consequences and Implications for Bacteria and Biofilms. *Annual Review of Chemical and Biomolecular Engineering* **9**, 175–200 (2018).

14.   Epstein, A. K., Wong, T.-S., Belisle, R. A., Boggs, E. M. & Aizenberg, J. Liquid-infused structured surfaces with exceptional anti-biofouling performance. *Proceedings of the National Academy of Sciences* **109**, 13182–13187 (2012).

15.   Cont, A., Vermeil, J. & Persat, A. *Mechanoregulation of biofilm architecture promotes* P. aeruginosa *antibiotic tolerance.* http://biorxiv.org/lookup/doi/10.1101/2022.02.16.480709   (2022) doi:10.1101/2022.02.16.480709.

16.   Gloag, E. S., Fabbri, S., Wozniak, D. J. & Stoodley, P. Biofilm mechanics: Implications in infection and survival. *Biofilm* **2**, 100017 (2020).

17.   Persat, A., Stone, H. A. & Gitai, Z. The curved shape of Caulobacter crescentus enhances surface colonization in flow. *Nature Communications* **5**, (2014).

18.   Thomas, W. E., Nilsson, L. M., Forero, M., Sokurenko, E. V. & Vogel, V. Shear-dependent 'stick-and-roll' adhesion of type 1 fimbriated Escherichia coli. *Molecular Microbiology* **53**, 1545–1557 (2004).

19.   Picioreanu, C., Blauert, F., Horn, H. & Wagner, M. Determination of mechanical properties of biofilms by modelling the deformation measured using optical coherence tomography. *Water Research* **145**, 588–598 (2018).

20.   Douarche, C., Allain, J.-M. & Raspaud, E. Bacillus subtilis Bacteria Generate an Internal Mechanical Force within a Biofilm. *Biophysical Journal* **109**, 2195–2202 (2015).

21.   Cont, A., Rossy, T., Al-Mayyah, Z. & Persat, A. Biofilms deform soft surfaces and disrupt epithelia. *eLife* **9**, e56533 (2020).

22.   Hall-Stoodley, L., Costerton, J. W. & Stoodley, P. Bacterial biofilms: from the natural environment to infectious diseases. *Nat. Rev. Microbiol.* **2**, 95–108 (2004).

23.   Nadell, C. D., Ricaurte, D., Yan, J., Drescher, K. & Bassler, B. L. Flow environment and matrix structure interact to determine spatial competition in Pseudomonas aeruginosa biofilms. *eLife* **6**, e21855 (2017).

24.   Nadell, C. D., Drescher, K. & Foster, K. R. Spatial structure, cooperation and competition in biofilms. *Nat. Rev. Microbiol.* **14**, 589–600 (2016).

25.   Battin, T. J., Besemer, K., Bengtsson, M. M., Romani, A. M. & Packmann, A. I. The ecology and biogeochemistry of stream biofilms. *Nature Reviews Microbiology* **14**, 251–263 (2016).

26.   Stokes, J. M., Lopatkin, A. J., Lobritz, M. A. & Collins, J. J. Bacterial Metabolism and Antibiotic Efficacy. *Cell Metab* **30**, 251–259 (2019).

27.   Stoodley, P., Cargo, R., Rupp, C. J., Wilson, S. & Klapper, I. Biofilm material properties as related to shear-induced deformation and detachment phenomena. *J Ind Microbiol Biotech* **29**, 361–367 (2002).

28.   Cámara, M. *et al.* Economic significance of biofilms: a multidisciplinary and cross-sectoral challenge. *npj Biofilms Microbiomes* **8**, 1–8 (2022).

29.   Lebeaux, D., Chauhan, A., Rendueles, O. & Beloin, C. From in vitro to in vivo Models of Bacterial Biofilm-Related Infections. *Pathogens* **2**, 288–356 (2013).

30.   Joly, V. *et al.* Value of antibiotic levels in serum and cardiac vegetations for predicting antibacterial effect of ceftriaxone in experimental Escherichia coli endocarditis. *Antimicrob Agents Chemother* **31**, 1632–1639 (1987).

31.   Ciofu, O., Moser, C., Jensen, P. Ø. & Høiby, N. Tolerance and resistance of microbial biofilms. *Nat Rev Microbiol* 1–15 (2022) doi:10.1038/s41579-022-00682-4.

32.   Antibiotic resistance. https://www.who.int/news-room/fact-sheets/detail/antibiotic-resistance.

33.   Wagner, C. E., Wheeler, K. M. & Ribbeck, K. Mucins and Their Role in Shaping the Functions of Mucus Barriers. *Annual Review of Cell and Developmental Biology* **34**, 189–215 (2018).

34.   Dhanisha, S. S., Guruvayoorappan, C., Drishya, S. & Abeesh, P. Mucins: Structural diversity, biosynthesis, its role in pathogenesis and as possible therapeutic targets. *Critical Reviews in Oncology / Hematology* **122**, 98–122 (2018).

35.   Zanin, M., Baviskar, P., Webster, R. & Webby, R. The Interaction between Respiratory Pathogens and Mucus. *Cell Host & Microbe* **19**, 159–168 (2016).

36.   Lai, S. K., Wang, Y.-Y., Wirtz, D. & Hanes, J. Micro- and macrorheology of mucus. *Adv Drug Deliv Rev* **61**, 86–100 (2009).

37.   Fahy, J. V. & Dickey, B. F. Airway mucus function and dysfunction. *New England Journal of Medicine* **363**, 2233–2247 (2010).

38.   Jacob, K. M. & Reguera, G. Competitive advantage of oral streptococci for colonization of the middle ear mucosa. *Biofilm* **4**, 100067 (2022).

39.   Béchon, N. & Ghigo, J.-M. Gut biofilms: Bacteroides as model symbionts to study biofilm formation by intestinal anaerobes. *FEMS Microbiology Reviews* **46**, fuab054 (2022).

40.   Srivastava, A., Gupta, J., Kumar, S. & Kumar, A. Gut biofilm forming bacteria in inflammatory bowel disease. *Microbial Pathogenesis* **112**, 5–14 (2017).

41.   Hardy, L., Cerca, N., Jespers, V., Vaneechoutte, M. & Crucitti, T. Bacterial biofilms in the vagina. *Research in Microbiology* **168**, 865–874 (2017).

42.   DePas, W. H. *et al.* Exposing the Three-Dimensional Biogeography and Metabolic States of Pathogens in Cystic Fibrosis Sputum via Hydrogel Embedding, Clearing, and rRNA Labeling. *mBio* **7**, e00796-16 (2016).

43.   Bjarnsholt, T. *et al.* The in vivo biofilm. *Trends in Microbiology* **21**, 466–474 (2013).

44.   Wucher, B. R. *et al.* Vibrio cholerae filamentation promotes chitin surface attachment at the expense of competition in biofilms. *Proceedings of the National Academy of Sciences* **116**, 14216–14221 (2019).

45.   Drescher, K., Shen, Y., Bassler, B. L. & Stone, H. A. Biofilm streamers cause catastrophic disruption of flow with consequences for environmental and medical systems. *Proc. Natl. Acad. Sci. U.S.A.* **110**, 4345–4350 (2013).

46.   Kumar, A. *et al.* Microscale confinement features can affect biofilm formation. *Microfluid Nanofluid* **14**, 895–902 (2013).

47.   Roberts, A. E. L., Kragh, K. N., Bjarnsholt, T. & Diggle, S. P. The Limitations of In Vitro Experimentation in Understanding Biofilms and Chronic Infection. *Journal of Molecular Biology* **427**, 3646–3661 (2015).

48.   Colvin, K. M. *et al.* The pel polysaccharide can serve a structural and protective role in the biofilm matrix of Pseudomonas aeruginosa. *PLoS Pathog.* **7**, e1001264 (2011).

49.   Nadell, C. D., Drescher, K., Wingreen, N. S. & Bassler, B. L. Extracellular matrix structure governs invasion resistance in bacterial biofilms. *ISME J.* **9**, 1700–1709 (2015).

50.   Vidakovic, L., Singh, P. K., Hartmann, R., Nadell, C. D. & Drescher, K. Dynamic biofilm architecture confers individual and collective mechanisms of viral protection. *Nat. Microbiol.* **3**, 26–31 (2018).

51.   Welch, J. L. M., Rossetti, B. J., Rieken, C. W., Dewhirst, F. E. & Borisy, G. G. Biogeography of a human oral microbiome at the micron scale. *Proc. Natl. Acad. Sci. U.S.A.* **113**, E791–E800 (2016).

52.   Mitri, S., Xavier, J. B. & Foster, K. R. Social evolution in multispecies biofilms. *Proc. Natl. Acad. Sci. U.S.A.* **108**, 10839–10846 (2011).

53.   Hartmann, R. *et al.* Emergence of three-dimensional order and structure in growing biofilms. *Nat. Phys.* **15**, 251–256 (2019).

54.   Entcheva-Dimitrov, P. & Spormann, A. M. Dynamics and Control of Biofilms of the Oligotrophic Bacterium Caulobacter crescentus. *J. Bacteriol.* **186**, 8254–8266 (2004).

55.   Lee, C. K. *et al.* Multigenerational memory and adaptive adhesion in early bacterial biofilm communities. *Proc. Natl. Acad. Sci. U.S.A.* **115**, 4471–4476 (2018).

56.   O'Toole, G. A. & Kolter, R. Flagellar and twitching motility are necessary for Pseudomonas aeruginosa biofilm development. *Mol. Microbiol.* **30**, 295–304 (1998).

57.   Zhao, K. *et al.* Psl trails guide exploration and microcolony formation in *Pseudomonas aeruginosa* biofilms. *Nature* **497**, 388–391 (2013).

58.   Martínez-García, R., Nadell, C. D., Hartmann, R., Drescher, K. & Bonachela, J. A. Cell adhesion and fluid flow jointly initiate genotype spatial distribution in biofilms. *PLoS Comput. Biol.* **14**, e1006094 (2018).

59.   Tsang, P. H., Li, G., Brun, Y. V., Freund, L. B. & Tang, J. X. Adhesion of single bacterial cells in the micronewton range. *Proc. Natl. Acad. Sci. U.S.A.* **103**, 5764–5768 (2006).

60.   Laub, M. T., Shapiro, L. & McAdams, H. H. Systems biology of Caulobacter. *Annu. Rev. Genet.* **41**, 429–441 (2007).

61.   Siegal-Gaskins, D. & Crosson, S. Tightly regulated and heritable division control in single bacterial cells. *Biophys. J.* **95**, 2063–2072 (2008).

62.   Hug, I., Deshpande, S., Sprecher, K. S., Pfohl, T. & Jenal, U. Second messenger–mediated tactile response by a bacterial rotary motor. *Science* **358**, 531–534 (2017).

63.   Berne, C. *et al.* Feedback regulation of Caulobacter crescentus holdfast synthesis by flagellum assembly via the holdfast inhibitor HfiA. *Mol. Microbiol.* **110**, 219–238 (2018).

64.   Berg, H. C. *Random walks in biology.* (Princeton University Press, 1993).

65.   Squires, T. M. & Quake, S. R. Microfluidics: Fluid physics at the nanoliter scale. *Rev. Mod. Phys.* **77**, 977–1026 (2005).

66.   Stone, H. A., Stroock, A. D. & Ajdari, A. Engineering Flows in Small Devices: Microfluidics Toward a Lab-on-a-Chip. *Annu. Rev. Fluid Mech.* **36**, 381–411 (2004).

67.   Kostenko, V., Salek, M. M., Sattari, P. & Martinuzzi, R. J. Staphylococcus aureus biofilm formation and tolerance to antibiotics in response to oscillatory shear stresses of physiological levels. *FEMS Immunol. Med. Microbiol.* **59**, 421–431 (2010).

68.   Purevdorj, B., Costerton, J. W. & Stoodley, P. Influence of Hydrodynamics and Cell Signaling on the Structure and Behavior of Pseudomonas aeruginosa Biofilms. *Appl. Environ. Microbiol.* **68**, 4457–4464 (2002).

69.   Kim, M. K., Ingremeau, F., Zhao, A., Bassler, B. L. & Stone, H. A. Local and global consequences of flow on bacterial quorum sensing. *Nat. Microbiol.* **1**, 15005 (2016).

70.   Duvernoy, M.-C. *et al.* Asymmetric adhesion of rod-shaped bacteria controls microcolony morphogenesis. *Nat. Commun.* **9**, 1120 (2018).

71. Christen, M. *et al.* Asymmetrical Distribution of the Second Messenger c-di-GMP upon Bacterial Cell Division. *Science* **328**, 1295–1297 (2010).

72. Gordon, V. D., Davis-Fields, M., Kovach, K. & Rodesney, C. A. Biofilms and mechanics: a review of experimental techniques and findings. *J. Phys. D: Appl. Phys.* **50**, 223002 (2017).

73. Chilukuri, S., Collins, C. H. & Underhill, P. T. Dispersion of flagellated swimming microorganisms in planar Poiseuille flow. *Phys. Fluids* **27**, 031902 (2015).

74. Okubo, A. & Levin, S. A. A Theoretical Framework for Data Analysis of Wind Dispersal of Seeds and Pollen. *Ecology* **70**, 329–338 (1989).

75. Liu, G. *et al.* A motility-induced phase transition drives Myxococcus xanthus aggregation. *arXiv:1709.06012*.

76. Cremer, J., Arnoldini, M. & Hwa, T. Effect of water flow and chemical environment on microbiota growth and composition in the human colon. *Proc. Natl. Acad. Sci. U.S.A.* **114**, 6438–6443 (2017).

77. Donaldson, G. P., Lee, S. M. & Mazmanian, S. K. Gut biogeography of the bacterial microbiota. *Nat. Rev. Microbiol.* **14**, 20–32 (2016).

78. Livraghi, A. & Randell, S. H. Cystic Fibrosis and Other Respiratory Diseases of Impaired Mucus Clearance. *Toxicologic Pathology* **35**, 116–129 (2007).

79. Kolpen, M. *et al.* Bacterial biofilms predominate in both acute and chronic human lung infections. *Thorax* (2022) doi:10.1136/thoraxjnl-2021-217576.

80. Fakih, D. *et al.* Normal murine respiratory tract has its mucus concentrated in clouds based on the Muc5b mucin. *American Journal of Physiology-Lung Cellular and Molecular Physiology* **318**, L1270–L1279 (2020).

81. Fernández-Blanco, J. A. *et al.* Attached stratified mucus separates bacteria from the epithelial cells in COPD lungs. *JCI Insight* **3**, e120994 (2018).

82. Hoegger, M. J. *et al.* Impaired mucus detachment disrupts mucociliary transport in a piglet model of cystic fibrosis. *Science* **345**, 818–822 (2014).

83.	Ostedgaard, L. S. *et al.* Gel-forming mucins form distinct morphologic structures in airways. *PNAS* **114**, 6842–6847 (2017).

84.	Ramirez-San Juan, G. R. *et al.* Multi-scale spatial heterogeneity enhances particle clearance in airway ciliary arrays. *Nature Physics* 1–7 (2020) doi:10.1038/s41567-020-0923-8.

85.	Kudo, E. *et al.* Low ambient humidity impairs barrier function and innate resistance against influenza infection. *PNAS* **116**, 10905–10910 (2019).

86.	Humayun, M., Chow, C.-W. & Young, E. Microfluidic Lung Airway-on-a-Chip with Arrayable Suspended Gels for Studying Epithelial and Smooth Muscle Cell Interactions. *Lab on a Chip* (2018) doi:10.1039/C7LC01357D.

87.	Rayner, R. E., Makena, P., Prasad, G. L. & Cormet-Boyaka, E. Optimization of Normal Human Bronchial Epithelial (NHBE) Cell 3D Cultures for in vitro Lung Model Studies. *Scientific Reports* **9**, 500 (2019).

88.	Secor, P. R. *et al.* Filamentous Bacteriophage Produced by Pseudomonas aeruginosa Alters the Inflammatory Response and Promotes Noninvasive Infection In Vivo. *Infection and Immunity* **85**, (2017).

89.	Davis, A. S. *et al.* Validation of Normal Human Bronchial Epithelial Cells as a Model for Influenza A Infections in Human Distal Trachea. *J Histochem Cytochem* **63**, 312–328 (2015).

90.	Kiedrowski, M. R. *et al.* Staphylococcus aureus Biofilm Growth on Cystic Fibrosis Airway Epithelial Cells Is Enhanced during Respiratory Syncytial Virus Coinfection. *mSphere* **3**, (2018).

91.	Kilic, O. *et al.* A microphysiological model of the bronchial airways reveals the interplay of mechanical and biochemical signals in bronchospasm. *Nature Biomedical Engineering* 1 (2019) doi:10.1038/s41551-019-0366-7.

92.	Si, L. *et al.* A human-airway-on-a-chip for the rapid identification of candidate antiviral therapeutics and prophylactics. *Nature Biomedical Engineering* 1–15 (2021) doi:10.1038/s41551-021-00718-9.

93.	Benam, K. H. *et al.* Small airway-on-a-chip enables analysis of human lung inflammation and drug responses in vitro. *Nature Methods* **13**, 151–157 (2016).

94.   Sachs, N. *et al.* Long-term expanding human airway organoids for disease modeling. *The EMBO Journal* **38**, e100300 (2019).

95.   Zhou, J. *et al.* Differentiated human airway organoids to assess infectivity of emerging influenza virus. *PNAS* **115**, 6822–6827 (2018).

96.   Tan, Q., Choi, K. M., Sicard, D. & Tschumperlin, D. J. Human airway organoid engineering as a step toward lung regeneration and disease modeling. *Biomaterials* **113**, 118–132 (2017).

97.   McCauley, K. B. *et al.* Efficient Derivation of Functional Human Airway Epithelium from Pluripotent Stem Cells via Temporal Regulation of Wnt Signaling. *Cell Stem Cell* **20**, 844-857.e6 (2017).

98.   Miller, A. J. *et al.* Generation of lung organoids from human pluripotent stem cells in vitro. *Nature Protocols* **14**, 518 (2019).

99.   Abeynaike, L., Meeusen, E. N. & Bischof, R. J. An ovine tracheal explant culture model for allergic airway inflammation. *J Inflamm (Lond)* **7**, 46 (2010).

100.   Nikolaev, M. *et al.* Homeostatic mini-intestines through scaffold-guided organoid morphogenesis. *Nature* **585**, 574–578 (2020).

101.   Jiménez-Torres, J. A., Peery, S. L., Sung, K. E. & Beebe, D. J. LumeNEXT: A Practical Method to Pattern Luminal Structures in ECM Gels. *Advanced Healthcare Materials* **5**, 198–204 (2016).

102.   Antoine, E. E., Vlachos, P. P. & Rylander, M. N. Review of Collagen I Hydrogels for Bioengineered Tissue Microenvironments: Characterization of Mechanics, Structure, and Transport. *Tissue Eng Part B Rev* **20**, 683–696 (2014).

103.   Ishikawa, S. & Ito, S. Repeated whole cigarette smoke exposure alters cell differentiation and augments secretion of inflammatory mediators in air-liquid interface three-dimensional co-culture model of human bronchial tissue. *Toxicology in Vitro* **38**, 170–178 (2017).

104.   Hinman, S. S., Wang, Y., Kim, R. & Allbritton, N. L. In vitro generation of self-renewing human intestinal epithelia over planar and shaped collagen hydrogels. *Nat Protoc* **16**, 352–382 (2021).

105.   Barkal, L. J. *et al.* Microbial volatile communication in human organotypic lung models. *Nature Communications* **8**, 1770 (2017).

106.   Dvorak, A., Tilley, A. E., Shaykhiev, R., Wang, R. & Crystal, R. G. Do Airway Epithelium Air–Liquid Cultures Represent the In Vivo Airway Epithelium Transcriptome? *Am J Respir Cell Mol Biol* **44**, 465–473 (2011).

107.   Travaglini, K. J. *et al.* A molecular cell atlas of the human lung from single-cell RNA sequencing. *Nature* **587**, 619–625 (2020).

108.   Deprez, M. *et al.* A Single-Cell Atlas of the Human Healthy Airways. *Am J Respir Crit Care Med* **202**, 1636–1645 (2020).

109.   Plasschaert, L. W. *et al.* A single-cell atlas of the airway epithelium reveals the CFTR-rich pulmonary ionocyte. *Nature* **560**, 377–381 (2018).

110.   Montoro, D. T. *et al.* A revised airway epithelial hierarchy includes CFTR-expressing ionocytes. *Nature* **560**, 319–324 (2018).

111.   Bukowy-Bieryłło, Z. Long-term differentiating primary human airway epithelial cell cultures: how far are we? *Cell Communication and Signaling* **19**, 63 (2021).

112.   Hewitt, R. J. & Lloyd, C. M. Regulation of immune responses by the airway epithelial cell landscape. *Nat Rev Immunol* **21**, 347–362 (2021).

113.   Hoegger, M. J. *et al.* Assessing mucociliary transport of single particles in vivo shows variable speed and preference for the ventral trachea in newborn pigs. *PNAS* **111**, 2355–2360 (2014).

114.   Bermbach, S. *et al.* Mechanisms of Cilia-Driven Transport in the Airways in the Absence of Mucus. *Am J Respir Cell Mol Biol* **51**, 56–67 (2014).

115.   Schindelin, J. *et al.* Fiji: an open-source platform for biological-image analysis. *Nat Methods* **9**, 676–682 (2012).

116.   What is Cell Ranger? -Software -Single Cell Gene Expression -Official 10x Genomics Support. https://support.10xgenomics.com/single-cell-gene-expression/software/pipelines/latest/what-is-cell-ranger.

117. Hao, Y. *et al.* Integrated analysis of multimodal single-cell data. *Cell* **184**, 3573-3587.e29 (2021).

118. Alexa, A. & Rahnenfuhrer, J. topGO: Enrichment Analysis for Gene Ontology. R package version 2.44.0. (2021).

119. Tinevez, J.-Y. *et al.* TrackMate: An open and extensible platform for single-particle tracking. *Methods* **115**, 80–90 (2017).

120. Kluyver, T. *et al.* Jupyter Notebooks – a publishing format for reproducible computational workflows. in (eds. Loizides, F. & Scmidt, B.) 87–90 (IOS Press, 2016). doi:10.3233/978-1-61499-649-1-87.

121. The top 10 causes of death. https://www.who.int/news-room/fact-sheets/detail/the-top-10-causes-of-death.

122. Button, B. M. & Button, B. Structure and Function of the Mucus Clearance System of the Lung. *Cold Spring Harbor Perspectives in Medicine* **3**, a009720–a009720 (2013).

123. Button, B. *et al.* A periciliary brush promotes the lung health by separating the mucus layer from airway epithelia. *Science* **337**, 937–941 (2012).

124. Folkesson, A. *et al.* Adaptation of Pseudomonas aeruginosa to the cystic fibrosis airway: an evolutionary perspective. *Nature Reviews Microbiology* **10**, 841–851 (2012).

125. Jorth, P. *et al.* Regional Isolation Drives Bacterial Diversification within Cystic Fibrosis Lungs. *Cell Host Microbe* **18**, 307–319 (2015).

126. Starkey, M. *et al.* Pseudomonas aeruginosa Rugose Small-Colony Variants Have Adaptations That Likely Promote Persistence in the Cystic Fibrosis Lung. *Journal of Bacteriology* **191**, 3492–3503 (2009).

127. Palmer, K. L., Mashburn, L. M., Singh, P. K. & Whiteley, M. Cystic Fibrosis Sputum Supports Growth and Cues Key Aspects of Pseudomonas aeruginosa Physiology. *Journal of Bacteriology* **187**, 5267–5277 (2005).

128. Landry, R. M., An, D., Hupp, J. T., Singh, P. K. & Parsek, M. R. Mucin–Pseudomonas aeruginosa interactions promote biofilm formation and antibiotic resistance. *Molecular Microbiology* **59**, 142–151 (2006).

129. Matsui, H. *et al.* A physical linkage between cystic fibrosis airway surface dehydration and Pseudomonas aeruginosa biofilms. *Proceedings of the National Academy of Sciences* **103**, 18131–18136 (2006).

130. Arora, S. K., Ritchings, B. W., Almira, E. C., Lory, S. & Ramphal, R. The Pseudomonas aeruginosa Flagellar Cap Protein, FliD, Is Responsible for Mucin Adhesion. *Infect Immun* **66**, 1000–1007 (1998).

131. Secor, P. R., Michaels, L. A., Ratjen, A., Jennings, L. K. & Singh, P. K. Entropically driven aggregation of bacteria by host polymers promotes antibiotic tolerance in Pseudomonas aeruginosa. *Proceedings of the National Academy of Sciences* **115**, 10780–10785 (2018).

132. Co, J. Y. *et al.* Mucins trigger dispersal of Pseudomonas aeruginosa biofilms. *NPJ Biofilms Microbiomes* **4**, (2018).

133. Wheeler, K. M. *et al.* Mucin glycans attenuate the virulence of Pseudomonas aeruginosa in infection. *Nature Microbiology* **4**, 2146–2154 (2019).

134. Caldara, M. *et al.* Mucin Biopolymers Prevent Bacterial Aggregation by Retaining Cells in the Free-Swimming State. *Current Biology* **22**, 2325–2330 (2012).

135. Kočevar-Nared, J., Kristl, J. & Šmid-Korbar, J. Comparative rheological investigation of crude gastric mucin and natural gastric mucus. *Biomaterials* **18**, 677–681 (1997).

136. Ma, L. *et al.* Assembly and Development of the Pseudomonas aeruginosa Biofilm Matrix. *PLOS Pathogens* **5**, e1000354 (2009).

137. Alrahman, M. A. & Yoon, S. S. Identification of essential genes of Pseudomonas aeruginosa for its growth in airway mucus. *J Microbiol.* **55**, 68–74 (2017).

138. Datta, S. S., Preska Steinberg, A. & Ismagilov, R. F. Polymers in the gut compress the colonic mucus hydrogel. *Proceedings of the National Academy of Sciences* **113**, 7041–7046 (2016).

139. Chapon-Hervé, V. *et al.* Regulation of the *xcp* secretion pathway by multiple quorum-sensing modulons in *Pseudomonas aeruginosa. Molecular Microbiology* **24**, 1169–1178 (1997).

140. Comolli, J. C., Waite, L. L., Mostov, K. E. & Engel, J. N. Pili Binding to Asialo-GM1 on Epithelial Cells Can Mediate Cytotoxicity or Bacterial Internalization by Pseudomonas aeruginosa. *Infect Immun* **67**, 3207–3214 (1999).

141. Bucior, I., Pielage, J. F. & Engel, J. N. Pseudomonas aeruginosa Pili and Flagella Mediate Distinct Binding and Signaling Events at the Apical and Basolateral Surface of Airway Epithelium. *PLOS Pathogens* **8**, e1002616 (2012).

142. Kim, J., Mailand, E., Ang, I., Sakar, M. S. & Bouklas, N. A model for 3D deformation and reconstruction of contractile microtissues. *Soft Matter* **17**, 10198–10209 (2021).

143. Burrows, L. L. Pseudomonas aeruginosa twitching motility: type IV pili in action. *Annu Rev Microbiol* **66**, 493–520 (2012).

144. Montefusco-Pereira, C. V. *et al.* P. aeruginosa Infected 3D Co-Culture of Bronchial Epithelial Cells and Macrophages at Air-Liquid Interface for Preclinical Evaluation of Anti-Infectives. *JoVE (Journal of Visualized Experiments)* e61069 (2020) doi:10.3791/61069.

145. Yonker, L. M. *et al.* Development of a Primary Human Co-Culture Model of Inflamed Airway Mucosa. *Sci Rep* **7**, 8182 (2017).

146. Choi, K.-H. & Schweizer, H. P. mini-Tn 7 insertion in bacteria with single att Tn 7 sites: example Pseudomonas aeruginosa. *Nature Protocols* **1**, 153–161 (2006).

147. Holloway, B. W. & Morgan, A. F. Genome Organization in Pseudomonas. *Annual Review of Microbiology* **40**, 79–105 (1986).

148. Ball, G., Chapon-Hervé, V., Bleves, S., Michel, G. & Bally, M. Assembly of XcpR in the Cytoplasmic Membrane Is Required for Extracellular Protein Secretion in Pseudomonas aeruginosa. *Journal of Bacteriology* **181**, 382–388 (1999).

149. Bertrand, J. J., West, J. T. & Engel, J. N. Genetic Analysis of the Regulation of Type IV Pilus Function by the Chp Chemosensory System of Pseudomonas aeruginosa. *Journal of Bacteriology* **192**, 994–1010 (2010).

150. Barken, K. B. *et al.* Roles of type IV pili, flagellum-mediated motility and extracellular DNA in the formation of mature multicellular structures in Pseudomonas aeruginosa biofilms. *Environmental Microbiology* **10**, 2331–2343 (2008).

151. Kühn, M. J. *et al.* Mechanotaxis directs Pseudomonas aeruginosa twitching motility. *Proceedings of the National Academy of Sciences* **118**, e2101759118 (2021).

152. Choi, K.-H. *et al.* A Tn7-based broad-range bacterial cloning and expression system. *Nat Methods* **2**, 443–448 (2005).

153. Bradski, G. The OpenCV Library. *Dr. Dobb's Journal: Software Tools for the Professional Programmer* **25**, (2000).

154. van der Walt, S. *et al.* scikit-image: image processing in Python. *PeerJ* **2**, e453 (2014).

155. Weber, M. statannot: add statistical annotations on an existing boxplot/barplot generated by seaborn.

156. Virtanen, P. *et al.* SciPy 1.0: fundamental algorithms for scientific computing in Python. *Nat Methods* **17**, 261–272 (2020).

157. Seabold, S. & Perktold, J. Statsmodels: Econometric and Statistical Modeling with Python. in 92–96 (2010). doi:10.25080/Majora-92bf1922-011.

158. Mailand, E., Li, B., Eyckmans, J., Bouklas, N. & Sakar, M. S. Surface and Bulk Stresses Drive Morphological Changes in Fibrous Microtissues. *Biophys J* **117**, 975–986 (2019).

159. Holzapfel, A. G. *Nonlinear solid mechanics II*. (2000).

160. Steinmann, P. On boundary potential energies in deformational and configurational mechanics. *Journal of the Mechanics and Physics of Solids* **3**, 772–800 (2008).

161. Javili, A. & Steinmann, P. A finite element framework for continua with boundary energies. Part II: The three-dimensional case. *Computer Methods in Applied Mechanics and Engineering* **199**, 755–765 (2010).

162. *Automated Solution of Differential Equations by the Finite Element Method*. vol. 84 (Springer Berlin Heidelberg, 2012).

163. Balay, S. *et al.* PETSc Users Manual. (2019).

164.   Fung, Y. C. *Biomechanics: mechanical properties of living tissues*. (Springer, 2011).

165.   Tilney, L. G. & Portnoy, D. A. Actin filaments and the growth, movement, and spread of the intracellular bacterial parasite, Listeria monocytogenes. *J Cell Biol* **109**, 1597–1608 (1989).

166.   Knutton, S., Baldwin, T., Williams, P. H. & McNeish, A. S. Actin accumulation at sites of bacterial adhesion to tissue culture cells: basis of a new diagnostic test for enteropathogenic and enterohemorrhagic Escherichia coli. *Infect Immun* **57**, 1290–1298 (1989).

167.   Fischer, A. J. *et al.* Sustained Coinfections with Staphylococcus aureus and Pseudomonas aeruginosa in Cystic Fibrosis. *Am J Respir Crit Care Med* **203**, 328–338 (2021).

168.   Cheung, K.-J. *et al.* Pilus-mediated epithelial cell death in response to infection with Burkholderia cenocepacia. *Microbes and Infection* **9**, 829–837 (2007).

169.   Malešević, M. *et al.* Virulence traits associated with Burkholderia cenocepacia ST856 epidemic strain isolated from cystic fibrosis patients. *Antimicrob Resist Infect Control* **6**, 57 (2017).

170.   Vesel, N. & Blokesch, M. Pilus Production in Acinetobacter baumannii Is Growth Phase Dependent and Essential for Natural Transformation. *J Bacteriol* **203**, e00034-21 (2021).

Curriculum Vitae

Tamara Rossy

0000-0002-0945-619X   www.linkedin.com/in/tamara-rossy

Google scholar page   @tamara_rossy

Education

PhD in Biotechnology and Bioengineering	**2017 – present**.
EPFL, Switzerland	(defended:
Laboratory of Prof. Alexandre Persat (Global Health Institute and Institute of Bioengineering)	Nov. 14th 2022)
MSc in Bioengineering (120 ECTS)	
EPFL, Switzerland	**2014 – 2016**
Specialization: Biomechanical Engineering, with Neuroprosthetics minor (30 ECTS)	
BSc in Life Sciences and Technologies (180 ECTS)	**2011 – 2014**
EPFL, Switzerland	

Research experience

PhD candidate	**2017 – present**
Persat laboratory, EPFL, Switzerland	(Jun. 2017 –
Bacterial colonization in realistic environments: how mechanics impact biofilm formation in the wild and during infection	present)
MSc thesis project	**2016**
Maharbiz Laboratory, University of California, Berkeley, USA	(Feb. – Aug.)
Development of a microfabrication process for ultrasonic implantable neural interfaces	
Student project	**2015**
Laboratory for Soft Bioelectronic Interfaces (Prof Lacour), EPFL, Switzerland	(Sep. – Dec.)
Fabrication of microtubes with spiral bending conformation for peripheral neural interfaces	
Internship in Bioengineering	**2015**
MindMaze SA, Ecublens, Switzerland	(Jul. – Aug.)
Virtual reality intervention in stroke patients	
Student project	**2014**
Jensen Laboratory, EPFL, Switzerland	(Sep. – Dec.)
Time-sampled approach for investigating resistance mutations to favipiravir in influenza A	
BSc thesis project	**2014**
Laboratory of Psychophysics (Prof Herzog), EPFL, Switzerland	(Feb. – Jun.)
Unpredictability in the Ternus-Pikler display and non-retinotopic representations	

Publications

First author publications

Rossy, T., Distler, T., Pezoldt, J., Kim, J., Tala, L., Bouklas, N., Deplancke, B., & Persat, A. (2022).
Pseudomonas aeruginosa contracts mucus to form biofilms in tissue-engineered human airways. *bioRxiv,* under review.

Rossy, T., Nadell, C. D., & Persat, A. (2019).
Cellular advective-diffusion drives the emergence of bacterial surface colonization patterns and heterogeneity. *Nature communications*, *10*(1), 1-9.

Other publications

Iouranova, A., Grun, D., Rossy, T., Duc, J., Coudray, A., Imbeault, M., de Tribolet-Hardy, J., Turelli, P., Persat A., & Trono, D. (2022).
KRAB zinc finger protein ZNF676 controls the transcriptional influence of LTR12-related endogenous retrovirus sequences. *Mobile DNA*, *13*(1), 1-17.

Garipelli, G., Rossy, T., Perez-Marcos, D., Jöhr, J., & Diserens, K. (2021).
Movement-related cortical potentials in embodied virtual mirror visual feedback. *Frontiers in Neurology*, 928.

Cont, A., Rossy, T., Al-Mayyah, Z., & Persat, A. (2020).
Biofilms deform soft surfaces and disrupt epithelia. *Elife*, *9*.

Conference presentations

EPFL Bioengineering Day 2022, Lausanne, Switzerland
Oral presentation selected from applications to the Hubbell-Swartz award: *Pseudomonas aeruginosa contracts mucus to rapidly form biofilms in tissue-engineered human airways*

Swiss Society for Microbiology, Annual congress, 2022, Lausanne, Switzerland
Invited oral presentation: *Pseudomonas aeruginosa contracts mucus to rapidly form biofilms in tissue-engineered human airways*

16th Mucins in Health and Disease conference, 2022, Utrecht, the Netherlands
Oral presentation selected from abstracts: *Pseudomonas aeruginosa contracts mucus to rapidly form biofilms in tissue-engineered human airways*

ASCB | EMBO Cell Bio meeting, 2021, virtual
Oral presentation selected from abstracts: *AirGel: a tissue-engineered airway for the investigation of respiratory infections*

EMBO | EMBL Symposium: Organoids: Modelling Organ Development and Disease in 3D Culture, 2020, virtual
Poster presentation: *AirGel: A tissue-engineered airway to study respiratory infections*

EMBO | EMBL Symposium: New Approaches and Concepts in Microbiology, 2019, Heidelberg, Germany
Poster presentation: *Cellular advective-diffusion drives the emergence of bacterial surface colonization patterns and heterogeneity*

8th ASM Conference on Biofilms, 2018, Washington DC, USA
Oral presentation selected from abstracts: *Fluid Flow, Motility and Cell Shape Set the Foundation for Biofilm Architecture of Caulobacter crescentus*
Meeting review: Fuqua, C., Filloux, A., Ghigo, J. M., & Visick, K. L. (2019). Biofilms 2018: A diversity of microbes and mechanisms. *Journal of Bacteriology*, *201*(18), e00118-19.

Awards and distinctions

Finalist for the 2022 Jeffrey Hubbell and Melody Swartz Young Bioengineer Award
500 CHF finalist prize

8th ASM Conference on Biofilms
500$ travel award

EPFL Global Health Institute retreat 2022
2nd prize for best talk by a PhD student

"Ma thèse en 180s" sci-com competition 2022
Audience choice award in the EPFL selection round, 2nd place in the EPFL final, participation to the Swiss final

High school diploma with highest honors

Sci-com & Outreach

Competition "Ma thèse en 180s" 2022, EPFL final and Swiss final

EPFL Open Days 50th anniversary, participated in the "Objet mystère" animation

Voir-est-savoir scientific imaging competition, 3rd place in 2019 and participated in 2020

Talks in front of EPFL SV Bachelor and Master students
SV Opportunities Exploration Day 2018, SV in Extenso 2021